

**Plasma dynamics at the surface
interface in radio frequency
discharges**

Martin Paul Blake

Doctor of Philosophy

University of York

Physics

July 2019

Abstract

Inductively coupled plasmas play an important role in the manufacture of computer chips through etching and deposition processes. This relies on established system pressures and power values in order to generate and sustain the required reactive species density. Oxygen and hydrogen plasmas are routinely used in this industry and will therefore be at the centre of this study. This research focuses on the development of a diagnostic procedure that resolves the plasma-surface interface by analysing stimulated plasma emission induced by a tailored voltage waveform (Pulse induced Optical Emission Spectroscopy (PiOES)). These measurements are generated in an area of the plasma that doesn't benefit from plasma emission produced via the inductive coil but does have great significance for industrial processes. The aim is to find a pulse regime that has minimal impact on electron and ion properties in the plasma-surface region, while producing enough emission to analyse the reactive chemistry and calculate atomic species densities. PiOES-ERA, HPEM and TALIF techniques have been compared and show good agreement in the measurement and simulation of atomic oxygen density in a low pressure E-mode plasma. This was achieved through the development of a tailored voltage waveform design and novel implementation within the GEC. The final result is a configurable pulse application that allows the operator to analyse different regions of the plasma, that were previously unobtainable. In both hydrogen and oxygen plasmas the E-H mode transition is found to be key in influencing the atomic species densities. In oxygen this is confirmed through the use of PROES measurements and HPEM simulations. The H-mode plasma measurements highlight additional excitation and/or de-excitation processes that are currently not considered in the ERA model, therefore more research into these processes is required to fully resolve them.

Contents

Abstract	2
Contents	3
List of Tables	5
List of Figures	6
Acknowledgements	12
Declaration	13
1 Introduction	14
1.1 Motivation	14
1.2 Outline	17
2 Theory of processing plasmas	18
2.1 Definition of a plasma	18
2.2 Low temperature plasmas	20
2.3 Inductively coupled plasmas	20
2.3.1 Plasma sheath	22
2.3.2 Ion Energy Distribution Function (IEDF)	25
3 Diagnostic and experimental configuration	29
3.1 Experimental configuration	29
3.1.1 Chamber geometry	30
3.1.2 Electrical components	31
3.2 Diagnostic techniques	32
3.2.1 Retarding Field Energy Analyser (RFEA)	33
3.2.2 Optical emission spectroscopy	34
3.2.3 Population of excited states	35
3.2.4 Phase resolved optical emission spectroscopy (PROES)	36
3.2.5 Classic actinometry	40
3.2.6 Advanced actinometry	41
3.2.7 Energy resolved actinometry	41
3.3 Two-Photon Absorption Laser Induced Fluorescence	45
3.3.1 Laser Induced Fluorescence	45
3.3.2 Two-Photon Laser Induced Fluorescence	46
3.3.3 Calibration	49
3.3.4 TALIF experimental technique	50

4	Low temperature plasma modelling	55
4.1	Hybrid plasma equipment model: modules and equations solved	56
4.2	Geometry	59
4.3	Chemistry	61
5	Pulse-induced OES: influence on plasma emission and substrate ion energies	65
5.1	Tailored voltage waveform development	65
5.1.1	Initial TVW design	66
5.1.2	Developed TVW design	68
5.1.3	Initial TVW design results	70
5.1.4	Modified TVW design results	76
5.2	Pulse influence on ion energy	79
6	Measurements and simulations of atomic oxygen densities and gas temperatures	87
6.1	TALIF measurements of O atom densities and gas temperature	88
6.1.1	Atomic O densities	91
6.1.2	Gas temperature	98
6.2	Modelling atomic oxygen density and gas temperature	102
6.3	PiOES-ERA + TALIF comparison	104
6.3.1	Pulse induced optical emission spectroscopy	106
6.3.2	Axial profiles of dissociation degree and mean electron energy	108
6.4	Comparison of PiOES and TALIF	110
6.4.1	ERA in H-mode analysis	112
6.5	Effectiveness of PiOES-ERA in Oxygen	113
7	Scaling of H density with pressure and power	115
7.1	Hydrogen atom TALIF	116
8	Conclusion	120
	Appendices	124
A	List of publications and conference attendances	125
B	Industrial relevance	127
B.1	Experimental setup	127
B.2	PiOES analysis	128
B.3	Surface analysis	129
B.3.1	SEM	129
B.3.2	EDX	131

List of Tables

2.1	Ion energies and fluxes in an ICP plasma driven at 13.56 MHz, with a floating lower electrode at 100 and 1000 W with pressures of 5 and 10 Pa, gas mixture is 98% O ₂ , 2% Ar.	28
3.1	This table highlights the emission wavelength, radiative lifetimes and quenching coefficients of the atomic states used in this work.	39
4.1	Complete chemistry set used in these HPEM simulations	61
4.1	Complete chemistry set used in these HPEM simulations	62
4.1	Complete chemistry set used in these HPEM simulations	63
B.1	Untreated quartz surface composition	131
B.2	Quartz surface composition, post plasma treatment with either an He/H ₂ or He/H ₂ /Ar plasma	132

List of Figures

2.1	Electric (E) and magnetic (B) fields in the planar ICP configuration, with field lines and direction indicated by the arrows	22
2.2	Charged particle density and electric potential representation, starting at the plasma bulk before transitioning into the sheath region and finishing at the reactor wall	24
2.3	Isotropic etching (a) for when sidewall slope doesn't matter and to undercut the mask for easy removal and (b) completely anisotropic etching; preferred pattern transfer method for nano and atomic scale processes	26
2.4	Floating lower electrode comparison of a 100 W E-mode (black dotted lines) to 1000 W H-mode (red dotted lines) IEDFs at 5 Pa (a) and 10 Pa (b) . . .	27
3.1	Schematic of the GEC, with RF and pulse generation mechanisms. A voltage probe measures the amplified pulse at the lower electrode and nanosecond resolution camera to capture pulse induced OES	31
3.2	Schematic of the RFEA probe with grids (G_1 to G_3) and collector plate (C) as illustrated	33
3.3	Sketch of a typical current voltage curve produced during a defined voltage range sweep (-20 to 140 eV) with associated current values	34
3.4	Sketch illustrating the population dynamics of the excited states (i and k) in a plasma. The basic corona model is shown in black, while the red lines and text illustrate the extension to the basic collisional radiative model with the addition of non-radiative de-excitation (quenching).	36
3.5	Illustration of the PROES principles and how they are obtained experimentally by varying the camera gate position.	37
3.6	PROES measurement over a single RF cycle (74 ns) using a 750 nm narrowband filter to capture emission from an oxygen/argon plasma operated at 100 W and 5 Pa.	38
3.7	The excitation plot is calculated using equation 3.2 from the PROES measurements in figure 3.6	40
3.8	Electron impact cross section profiles of the excitation states used in this work (750, 777 and 844 nm). D and De refer to the direct and dissociative excitation respectively [1-3].	43
3.9	Calculated excitation ratios of the 750 and 844 nm line (a) and 777 and 844 nm line (b) as a function of dissociation degree and mean electron energy. .	44
3.10	This plot represents an overlay of the contour lines for both the excitation ratios shown in figures 3.9a and 3.9b, these excitation ratios are obtained with a 98% O_2 and 2% Ar gas mixture.	45

3.11	Processes in TALIF start with two photon absorption from the ground state (E_1) into (E_2) followed by the various de-excitation processes (radiative decay and quenching).	46
3.12	Oxygen and xenon TALIF schemes	51
3.13	Hydrogen and krypton TALIF schemes	52
3.14	Experimental schematic based on the GEC cell including laser set-up and ICCD configuration	52
3.15	TALIF calibration and measurement in the GEC reference cell. Xenon calibration measurement at 20 Pa with a laser energy of 100 μ J (a) and 20 Pa oxygen/argon plasma operated at 200 W and 800 μ J laser energy (b) . .	53
3.16	Sample oxygen TALIF signal, by increasing the laser energy it highlights the point at which the TALIF signal saturates and no longer exhibits a linear response. Here, a linear response is observed up to 800 μ J. The plasma was operated at 50 W at a pressure of 10 Pa and gas mixture of O ₂ /Ar (98%/2%).	54
4.1	List of HPEM modules with the complete life-cycle achieved in one iteration	57
4.2	Schematic of the plasma geometry used in this work, modelled on the GEC reference cell	60
5.1	Initial pulse shape, with the shortest achievable pulse width (50 ns) at FWHM and voltage varied between 30—70 V, the large black dots represent the points at which the waveform can be manually modified from.	67
5.2	Tailored voltage waveforms with a positive (a) and negative (b) polarity. Generated using equation 5.1 with an increasing number of harmonics (1, 4 and 8). The timescales (x-axis) are over one full RF cycle of 74 ns. The peak to peak voltage (V_{pp}) is set according to the pulse shape and experimental configuration.	69
5.3	This figure illustrates a 70 V positive pulse applied at the lower electrode over multiple RF cycles, the line plot is a spatial integration and shows the additional emission from the pulse during the plasma sustainment mechanisms. These measurements are taken at system pressures of 10 Pa with a 1:2 Ar/O ₂ gas ratio operated at 50 W	70
5.4	Initial PiOES emission measurements, a peak to peak voltage increase of 30, 50 and 70 V_{pp} in figures a,c and e respectively. Spatial integration (0-4 mm) as a function of time (ns) for each of the PiOES images b, d and f. The plasma is operated with a gas ratio of 1:2 Ar/O ₂ and a system pressure of 10 Pa at 50 W.	71
5.5	The four phase positions assigned to the plasma background voltage waveform detected by the voltage probe and displayed on the oscilloscope, these are spaced 90° apart and are selected prior to the pulse being applied at the lower electrode.	72
5.6	Initial TVW design applied to the plasma background voltage at the four phase positions, the plasma needs to be operational before the phase positions are apparent, at which point the phase can be selected and a pulse applied	73

5.7	IEDF measurements of a positive pulse at the four phase positions P1 (a), P2 (b), P3 (c) and P4 (d) as highlighted in figure 5.5, with a baseline taken using the Impedans RFEA probe and no pulse. An ideal pulse will have minimal deviation from the baseline value across all pulse voltages, the plasma is operated at 50 W in a 1:2 Ar/O ₂ gas mixture, with a system pressure of 10 Pa	74
5.8	DC bias for the pulse voltage variations at the different phase positions as shown in figure 5.7, P2 has the largest ion energy variation ($\sim 20 - 35$ eV) is represented by a more negative DC bias in order to counteract the increase in electrons at the surface.	75
5.9	Plot (a) is a negative 70 V pulse waveform over multiple RF cycles, while (b) depicts both positive and negative pulses over a shorter timescale, highlighting the reduced pulse width and rise times. The plasma is operated at 50 W with a pressure of 10 Pa and gas mixture of O ₂ /Ar (98%/2%).	77
5.10	Plots (a) is a positive 70 V pulse waveform, while (b) is a negative 70 V pulse with opposite polarity, these plots show the varying impact of the polarity on the bulk of the plasma due to the electron and ion behaviour. The plasma is operated at 50 W with a pressure of 10 Pa and gas mixture of O ₂ /Ar (98%/2%).	78
5.11	PROES measurement of the lower electrode region <25 mm with a 70 V _{pp} positive (a) and negative (b) pulse applied, these are a close up of the same region with the negative pulse emission shifting towards the plasma bulk as the negative pulse repels the electrons at the lower electrode surface. The plasma is operated at 50 W with a pressure of 10 Pa and gas mixture of O ₂ /Ar (98%/2%).	78
5.12	PROES measurement of the lower electrode region <25 mm of a 30 V _{pp} positive (a) and negative (b) pulse, they show no clear pulse induced emission. The plasma is operated at 50 W with a pressure of 10 Pa and gas mixture of O ₂ /Ar (98%/2%).	79
5.13	These plots illustrate the ion energy and flux for a positive (a) and negative (b) pulse voltage variation, these results show that a positive pulse has a greater influence on ion properties and DC self bias. The plasma is operated at 50 W with a pressure of 10 Pa and gas mixture of O ₂ /Ar (98%/2%). Pulse voltage is 100 V _{pp}	80
5.14	Ion flux (a) and DC bias (b) for the IEDF pulse voltage variation. The positive pulse has a larger ion flux variation and more negative DC self bias at the electrode surface. The plasma is operated at 50 W with a pressure of 10 Pa and gas mixture of O ₂ /Ar (98%/2%), Pulse voltages measured are 30, 50, 70 and 100 V _{pp}	80
5.15	Positive (a) and negative (b) pulse voltage variation with the background ion flux subtracted from each pulse voltage plot. Highlighting the baseline change from the background measurement taken for both sets of measurements. The plasma is operated at 50 W with a pressure of 10 Pa and gas mixture of O ₂ /Ar (98%/2%). Pulse voltage is 100 V _{pp}	82
5.16	Ion energy data taken for different repetition rates 452, 226 and 113 kHz, with identical plasma powers of 50 W and system pressure maintained at 10 Pa, the gas mixture is O ₂ /Ar (98%/2%). At the highest repetition frequency (452 kHz) the ion flux and energy impact is observed, with a positive pulse voltage of 100 V _{pp}	83

5.17	Ion flux (a) and DC bias (b) for the IEDF pulse frequency variation, both plots exhibit an increasing trend with increased repetition rates. Highlighting the importance of creating enough induced emission while keeping the repetition frequency low. The plasma is operated at 50 W with a pressure of 10 Pa and gas mixture of O ₂ /Ar (98%/2%).	83
5.18	Ion energy data taken for a positive (a) and negative (b) polarity pulse at the four phase positions as outlined in figure 5.5, the negative pulse shows an overall lower ion energy value and greater consistency, which is preferential for the measurements taken in chapter 6. The plasma is operated at 50 W with a pressure of 10 Pa and gas mixture of O ₂ /Ar (98%/2%), with a pulse voltage of 100 V _{pp}	84
6.1	844 nm emission of an O ₂ /Ar plasma (98%/2%) operated at 800 W with a system pressure of 150 Pa and TALIF laser energy of 800 μJ. The dotted white lines represent the electrode surfaces. This figure represents a 2 ns image taken from the full wavelength sweep, illustrating the position of the plasma and TALIF laser beam.	90
6.2	Atomic oxygen density contour plot (a) measured in a plasma operating a gas mixtures of O ₂ /Ar (98%/2%) and increasing pressure (0 - 250 Pa) and plasma power (200 - 1000 W) values, the atomic oxygen densities increase with both pressure and power, while the effective lifetime (b) of atomic oxygen in the same pressure and power parameter range also increases with plasma power.	92
6.3	Contour plot of the dissociation degree as a function of system pressure and power. Increasing dissociation is observed at higher plasma powers as the electron density increases and influences the electron impact dissociation rates. Gas mixture is O ₂ /Ar (98%/2%).	95
6.4	PROES images and plots indicating an E-H mode transition in an oxygen plasma with small argon admixture. The mode transition can be observed in both the PROES images and clearly in the plot of atomic oxygen densities. It is marked by the addition of a second sheath structure (plot (c)) and the jump in oxygen density as shown in the final plot (f). The plasma pressure is 150 Pa and incremental plasma power measurements of 200 - 1000 W. Gas mixture is O ₂ /Ar (98%/2%).	97
6.5	TALIF measurements of absolute O density as a function of plasma power (a) and pressure variation (b) are plotted, laser energy was 800 μJ as previously calibrated. Trends vary significantly depending on pressure and power with possible thermal effects which would impact recombination rate, the consideration of surface loss processes at different conditions is also a factor. Gas mixture is O ₂ /Ar (98%/2%).	99
6.6	Gas temperature contour plot for a power (200 - 1000 W) and pressure (20 - 250 Pa) variation. Gas temperature peaks at an increased plasma power while higher system pressures suppress the temperature due to an overall lower average gain per molecule. Gas mixture is O ₂ /Ar (98%/2%).	100
6.7	Line plot of pressure (20 - 250 Pa) (a) as a function of plasma power and gas temperature, and plot (b) showing the highest (1000 W) and lowest (200 W) plasma power measurements as a function of gas pressure and temperature. Gas mixture is O ₂ /Ar (98%/2%).	101

6.8	Atomic oxygen density simulation using the oxygen/argon chemistry set in chapter 4, modelled in a 200 W plasma with a pressure of 150 Pa, the high atomic density value at the electrode is a consequence of the edge effects between the electrode edge and ground ring and is only observed in the capacitive mode due to the strong electric fields generated in that axis. Gas mixture is O ₂ /Ar (98%/2%).	102
6.9	HPEM simulation of electron density as a function of pressure (150 Pa) and plasma power (200 - 1000 W) highlighting the step like increase in electron density due to increased plasma power and mode transition from capacitive to inductive plasma. Gas mixture is O ₂ /Ar (98%/2%).	104
6.10	HPEM simulation and TALIF measurements compared over the same operational conditions of 150 Pa, with a plasma power variation from 200 - 1000 W. Both methods show similar trends in the E-H transition region with the HPEM model predicting a slightly earlier transition start period. Gas mixture is O ₂ /Ar (98%/2%).	105
6.11	Comparison of the TALIF calculated gas temperatures and HPEM simulated results, as a function of plasma power (200 - 1000 W) and constant pressure (150 Pa). Gas mixture is O ₂ /Ar (98%/2%). These results have fairly good agreement with similar trends.	105
6.12	Comparison of PiOES images at 50 Pa (a) and 250 Pa (b) The dashed white lines mark the regions where ERA results have been extracted. The opposing pressures highlight the PiOES impact across the spatial region of the image with the higher pressure confining the stimulated emission to the lower electrode and the plasma clearly in a capacitive mode (plot (b)). Gas mixture is O ₂ /Ar (98%/2%) and the plasma is operated at 200 W.	107
6.13	Dissociation degree profile for 50 and 100 Pa measurements within the region between the two electrodes. The highest dissociation degree occurs at the centre of the plasma where losses through surface recombination are lowest. Gas mixture is O ₂ /Ar (98%/2%) and the plasma is operated at 200 W.	109
6.14	Mean electron energy plot of the inter-electrode gap for 50 and 100 Pa pressure plasmas, calculated assuming a Maxwellian EEDF. The highest electron energies are present in the sheath region due to heating from the plasma sheath and TVW. Gas mixture is O ₂ /Ar (98%/2%) and the plasma is operated at 200 W.	110
6.15	Comparison of atomic oxygen densities calculated using ERA and measured with TALIF in a 200 W O ₂ /Ar plasma (98%/2%) plasma, with an additional literature measurement (blue triangle) by Gomez et al at 50 Pa and 250 W in a GEC operating in an oxygen chemistry [4], showing good agreement in the capacitive plasma regime.	111
6.16	Mean electron energies calculated using ERA as a function of pressure, a decreasing trend in mean electron energy is observed over the pressure increase with possible discrepancies in the EEDF used to calculate the 20 and 50 Pa results. Gas mixture is O ₂ /Ar (98%/2%) and the plasma is operated at 200 W.	112

7.1	Hydrogen density plot as a function of plasma power and pressure (a) and effective lifetime (b) illustrating similar trends to the oxygen experimentation. Increasing H atom density with pressure and power as a result of increased electron impact dissociation. Effective lifetime is also increasing with power due to the higher gas temperatures and lower gas densities.	117
7.2	Dissociation degree at a T_{gas} value of 400 K as a function of plasma power and pressure. The higher pressure (100 - 250 Pa) results stay fairly linear while 20 and 50 Pa demonstrate much larger dissociation degree increases.	118
7.3	Atomic hydrogen density plots of pressure (20 Pa) plot (a) and plasma power (200 W) plot (b) highlighting a much later E-H mode transition between 800 - 1000 W at low pressures. While the constant power case only increases gradually with no steps or jumps.	118
8.1	Plot (a) TVW design that focuses excitation and emission at the plasma-surface interface, while (b) tailors a waveform that allows axial measurements between the electrodes.	123
B.1	Plasma discharge region with quartz glass cylinder placed on the lower electrode, operated at 1000 W and 250 Pa	128
B.2	1000 W 6/1 He/H ₂ plasma at 250 Pa with 400 V _{pp} , negative polarity pulse applied.	129
B.3	far field amplification figure (a) is a 1 kw 250 Pa ICP plasma treated carbon sample, whereas (b) is an untreated sample	130
B.4	Mid range magnification figure (a) is a 1 kw 250 Pa ICP plasma treated carbon sample, whereas (b) is an untreated sample.	130

Acknowledgments

My thanks and appreciation to Prof. Timo Gans and Prof. Deborah O'Connell for providing excellent guidance and helpful discussion during my time in the low temperature group, the past 6 years have been challenging but immensely rewarding.

To those lucky few, Andy West, Andrew Hurlbatt and Dave Shaw who have sat in ear shot of me throughout my time in the YPI I am grateful for your friendship and excellent conversation. To Andrew Gibson my sincerest thanks for your technical input no matter how ridiculous the question.

The lab crew; managed by the excellent Kari Niemi and Richard Armitage whose solution to every problem was always truly inspired.

Many thanks to Jerome Bredin and Sandra Schroeter for their assistance during the TALIF measurements, to James Ellis for your help with PROES data collection and finally Andrew Gibson for your assistance with ERA analysis.

To my peers and friends in the LTP group and York Plasma Institute, I am thankful for your good humour and friendship.

To my partner Liv, your understanding and patience in my most emotional stages of the PhD have been a source of true comfort. I am truly excited for our next step, wherever that may be.

Declaration

I declare that this thesis has been written by me and has not previously been accepted for any degree and is not being concurrently submitted in candidature for any degree other than Doctor of Philosophy at the University of York. This thesis is the result of my own investigations, except where otherwise stated. All other sources are acknowledged by explicit references.

The two-photon absorption laser induced fluorescence set up was constructed by Dr. Jerome Bredin and Dr. Kari Niemi. Analysis software for the TALIF experiments was developed by Dr. Jerome Bredin and Dr. Sandra Schroeter. Data from this setup was taken, analysed and interpreted by the author. The numerical simulations were made possible by the HPEM code which was provided by Prof. Mark Kushner of the University of Michigan, the oxygen chemistry set was used under permission from Dr Andrew Gibson. The simulations were run and analysed by the author. The phase resolved optical emission spectroscopy data was collected by the author, with the assistance of James Ellis, and analysed and interpreted by the author. The ion energy distribution function data were collected, analysed and interpreted by the author. The data for the Energy Resolved Actinometry analysis was collected by the author, while the software development and analysis of this data was carried out by Dr. Andrew Gibson. The data was interpreted by the author. The reactor setup and implementation of the nanosecond pulse for the pulse induced optical emission spectroscopy measurements was carried out by the author with the help of Dr. Andrew Gibson, Dr. Kari Niemi and Dr. Arthur Greb.

Chapter 1

Introduction

1.1 Motivation

Low temperature plasmas are widely used for nanoscale etching and deposition processes. These processes are crucial in a range of industries; an example of this is the production of computer chips and hard drives. Rapid growth and development within these industries towards atomic scale resolution requires greater understanding of plasma properties, especially at the plasma-surface interface. As surface processing is carried out mainly by reactive neutrals and ions, their densities are particularly important. A major challenge in industry is to measure and control the densities of these species in the complex and dynamic environment produced by a plasma [5]. This research will investigate possible diagnostics tailored to regions of the plasma with little or no observable emission.

A key challenge associated with measuring plasma properties inside industrial reactors is the limited diagnostic access, as physical probes and windows have the potential to influence processes. This results in poorly characterised processes with no definitive monitoring system. Electrical diagnostics are used in industry as they do not disturb the plasma. For example, plasma impedance measurements can be used in combination with models to estimate plasma densities and etch rates [6]. Lynn et al have demonstrated that these measurements can also be used in combination with Virtual Metrology (VM) models to control etch rates in industrial reactors [6].

A tool or process change in industry is typically measured by optical emission spectroscopy (OES) using broadband spectrometers [7,8]. Interpretation of OES data is dif-

difficult and relies on a range of assumptions, such as time and space integrated measurements, where the electron dynamics in a technological CCP/ICP plasma are modulated on ns timescales this means ns time resolution OES is required to analyse the electron dynamics accurately, this has resulted in a nanosecond resolution Andor camera being used throughout this work.

The use of OES allows process engineers to detect general changes in plasma conditions during a manufacturing cycle, for example, to determine the end-point of an etching process [9]. This helps engineers control day-to-day process stability and outcomes. OES can also be used in combination with control algorithms to monitor process instabilities [10]. Alternative techniques using OES and a digital imaging technique have shown that comparing image patterns of process conditions between the captured data and a standardized model will show significant changes during the plasma etch process, it highlights a shift from the baseline model and alerts the operator [11]. A disadvantage of OES is that it only gives indirect and not quantitative information, it would be more useful to develop a higher precision model.

The focus of this study is to develop and test a novel non-invasive plasma diagnostic for use in a range of low temperature plasmas. It aims to calculate reactive neutral species directly at the lower electrode in low power plasma conditions, which are important for surface modification processes requiring precise neutral densities to minimise surface or wafer damage. This study focusses on oxygen plasmas, however the method for measuring and collecting this data will form a process for other gases and plasma conditions in the future. Since the electron density in the plasma sheath is low (refer to chapter 2) there is no strong emission in the region above the lower electrode, and therefore OES measurements under normal conditions do not give any information. To address this a novel process has been successfully tested on the GEC in a low power oxygen plasma.

The technique is a pulse-induced OES (PiOES), where a short ns voltage pulse is applied to the substrate electrode of the plasma at a low frequency, causing a small amount of detectable emission to be produced and collected via a ns resolution camera, in an otherwise dark region of the plasma. An advanced actinometry technique is applied to calculate the species densities, by tailoring the voltage waveform to achieve a short pulse width and low frequency the overall plasma properties should not be affected, resulting in

a diagnostic that can be applied to an environment where its important that the plasma is not perturbed for long time periods (tens of ns). This will be compared with two-photon absorption laser induced fluorescence (TALIF) which will provide a reference to the absolute species densities measured using the PiOES technique, ordinarily TALIF is not able to operate in a processing plasma due to the lack of access and line of sight requirement, however this is not an issue for the gaseous electronics conference (GEC) cell.

The diagnostic developed in this research goes beyond basic broadband spectrometer collection and instead combines PiOES with a benchmarked analysis technique. As in the lab based measurements, it would utilise the small viewing port holes present on processing chambers to collect the OES. By manufacturing a pulse inside the plasma chamber it doesn't rely on predictive models or apparent baseline shift but instead manufactures and collects a known quantity. The PiOES pulse will have small influences on short timescales but not on the same order as a probe placed directly in the system. A range of pulse conditions are compared in this work and tested on an ion energy probe, to ascertain the ideal operating conditions.

Plasmas used in industrial processes are still not completely understood, therefore measurements across a broad range of operating conditions will be examined with the aim of understanding the scaling of reactive species densities with both TALIF and actinometry techniques. Inductively coupled (ICP) plasmas are commonly operated in industry with gas mixtures of Ar/O₂, and He/H₂, these particular gas mixtures are both frequently used for etching and cleaning during the multi-stage process. The role of gas temperature variations in these systems is also considered, as this is a property of industrial plasmas that is typically not well characterised, but affects other plasma properties.

All this research will take place in a laboratory environment with a scaled down version of the reactor used in industry i.e. the GEC cell. It is representative of the typical properties of industrial scale reactors but has better access to allow a wide variety of diagnostic configurations.

An outline of what is included in the individual chapters is given below.

1.2 Outline

Chapter 2 gives a fundamental overview focussing on inductively coupled plasmas operated within a low temperature, low pressure regime. With particular emphasis on the plasma sheath region and ion energy distribution function of the operating conditions.

Chapter 3 introduces the theoretical background to the diagnostics used in this work, including the operational set-up used to study the plasma.

Chapter 4 discusses the low temperature plasma modelling approach using a hybrid model with the key theory, chemistry and model configuration.

Chapter 5 contains the characterisation of an electrical pulse applied to the GEC cell, which is used to generate OES and operate in a minimally invasive regime.

Chapter 6 calculates the key atomic species density and gas temperature in an oxygen plasma, while monitoring plasma behaviour using a range of diagnostics. It compares each of the values under the same parameter regime and validates PiOES-ERA against TALIF and HPEM.

Chapter 7 A hydrogen plasma is analysed using TALIF, with a wide parametric study to compare its behaviour and plasma condition under similar process driven conditions to the previous chapter.

Chapter 8 Concludes the research presented in this project and proposes future work and ideas for the novel plasma diagnostic developed in this work.

Chapter 2

Theory of processing plasmas

This chapter introduces plasma concepts and properties that are of interest for understanding industrial plasmas. A general low temperature plasma overview will be described with emphasis on the physics, including ionisation and sustainment mechanisms in Radio Frequency (RF) plasmas. It highlights the importance of low temperature, low pressure Inductively Coupled Plasmas (ICPs), a key processing technology within the semiconductor industry.

2.1 Definition of a plasma

Low pressure, low temperature inductively coupled plasmas (ICP) with high plasma density are used for an array of technical processing applications. This includes processes such as etching and deposition [12–14], in particular, oxygen and hydrogen containing plasmas are commonly used due to the high reactivity of atomic oxygen and hydrogen and their ability to modify surfaces [15, 16].

The electromagnetic field is created by flowing RF current through the coil, generating magnetic and electric fields inside the plasma chamber as RF power is coupled through the dielectric window. This process results in a gas mixture within the closed system breaking into components of electrons and ions. The resulting system has approximately equal electron and ion charge densities which allows it to be in a quasi-neutral state. This is defined as an ionised gas, also referred to as the fourth state of matter.

For a system with charged particles we have to consider 'collective behaviour' [17]. This

refers to the movement of the individual charged particles, which produce local positive or negative charges and subsequently electromagnetic forces which can act over long distances. Resulting in a plasma that produces a much more complex environment in comparison with a neutral gas.

Quasineutrality and the Debye length are also key parameters in defining the conditions of a plasma. Firstly the Debye length λ_D is defined in equation 2.1 and then the concept of quasineutrality will be explained relative to it.

$$\lambda_D \equiv \left(\frac{\epsilon_0 k_b T_e}{n e^2} \right)^{\frac{1}{2}} \quad (2.1)$$

Due to the electron mobility and temperature T_e (Kelvin) within the system being far greater than that of the ions, the ions are perceived as stationary for simplicity, but do form a positive background charge. The plasma density is represented by n and the fundamental electron charge e . The permittivity of free space ϵ_0 , and the Boltzmann constant k_b . For this work, the ICP plasma has electron densities of 10^{14} to 10^{17} m⁻³, effective bulk electron temperatures of 1 to 5 eV, and gas pressures of 1 Pa to 250 Pa. The corresponding range of Debye lengths is 0.01 mm to 0.52 mm. The sheath thickness should be on the same order of thickness as the Debye length.

One characteristic property of a plasma is its ability to shield electric charges on a length scale less than the system dimensions, L . For example a positive point charge within a plasma will attract electrons due to their charge, however the concentration of electrons surrounding the point charge will be affected differently depending on its relative distance to the positive charge, where electrons on the outer edges are governed also by their thermal energy and not held fully by the electrostatic potential. Equation 2.1 shows that the larger the electron energy, $k_b T_e$, the bigger the plasma must be to screen the charges. Whereas, if there is a greater number of charge carriers, the plasma is more effective at screening them and the Debye length is smaller.

From the Debye length definition it is clear that on a microscopic scale the plasma will have electric fields of varying sizes in different local regions, therefore it is referred to as being in a quasineutral state, however when referring to it on a macroscopic scale then $n_i \approx n_e$, where n_i refers to the total ion density and n_e is the electron density with zero

net system charge. So to conclude, a plasma can be defined as a partially ionised gas, which consists of charged and neutral particles which display a collective behaviour and exists in a quasineutral state.

2.2 Low temperature plasmas

Low temperature plasmas are made up of partially ionized gases; which are a small proportion of the plasma density when compared with the large neutral gas density. The lack of thermal equilibrium is due to the relative mass difference between the electrons and ions. Where a rapidly varying electric field is applied to the gas that selectively heats the electrons more effectively due to their mobility and smaller mass. This results in an environment where $T_e \gg T_i$ i.e. the neutral gas temperature tends to be similar to or lower than the ion temperature.

The benefit of working with low neutral gas temperatures, is they can be used to treat or modify sensitive surfaces both within the semiconductor manufacturing industry and for biomedical applications. The relatively high temperature of plasma electrons also lead to the production of a highly reactive plasma chemistry. This is dependent on the type of gas, pressure and the mode of power deposition into the system.

All measurements carried out in this research are done so on a plasma operated in a low pressure, low temperature mode to investigate the gas phase chemistry by varying plasma power, pressure and gas mixture. This testing aims to develop a greater understanding of where existing plasma processes can be applied more effectively. In the following sections, important properties of ICPs, namely plasma sheaths and the relevance of monitoring ion energies will be explained in more detail.

2.3 Inductively coupled plasmas

The use of inductive coupling for the generation of plasmas with high ion densities, radicals and electrons is popular when considering the processing of integrated circuits (IC) [18]. The RF is coupled across a dielectric window instead of a direct electrode as in a capacitively coupled plasma (CCP) configuration. Low voltages across the sheath in ICPs are

also an advantage for various high precision manufacturing applications. If necessary, the lower electrode can be separately powered to modify ion energies. ICPs are perceived to be the most efficient way to produce a high density plasma at low pressures, which factors in system design and cost [19].

The ICP coil used in this research is pictured in figure 2.1. The electrode and coil configurations of the GEC allows for either an inductively or capacitively coupled plasma regime. When operating the planar inductive circuit via the copper coil in the upper electrode, the energy to sustain the plasma is coupled from the RF generator through the coil and quartz window into the GEC chamber. A match box is placed before the coil to tune the inductor [14, 20].

The inductor requires accurate tuning by electrical reactance to achieve the most reliable resonance at the industrially relevant 13.56 MHz driving frequency. The time-varying currents that exist within the coil generate time-varying magnetic fields which generates electric fields in the low pressure gas in the reactor. This process is described by Faraday's law and can be used to explain the RF electric field induced by the time varying RF magnetic field. Equation 2.2 shows the usual form of the Maxwell-Faraday equation. Where $\mathbf{E}(\mathbf{r}, t)$ is the electric field vector and $\mathbf{H}(\mathbf{r}, t)$ is the magnetic field vector. The electric field created by the inductive coil is what sustains the plasma.

$$\nabla \times \mathbf{E} = -\frac{\delta \mathbf{B}}{\delta t} \quad (2.2)$$

The discharge is capacitively driven at low plasma densities with a transition region dependent on gas, pressure and power coupled in. As the plasma densities increase a transition from E- to H-mode occurs, which signals a move from a capacitively coupled plasma to an inductively coupled one.

At low absorbed power, the copper coil is driven in an electrical resonance mode, high potentials with lower plasma density are characteristics of a capacitive discharge. This mode is characterised by an observable sheath, for industrial purposes this mode is ideal for sputtering as ions are accelerated across the sheath [21, 22]. For plasmas with larger absorbed powers a transition into a fully inductive mode occurs, this produces a higher plasma density and an increase in luminosity. Outside the IC industry they are also

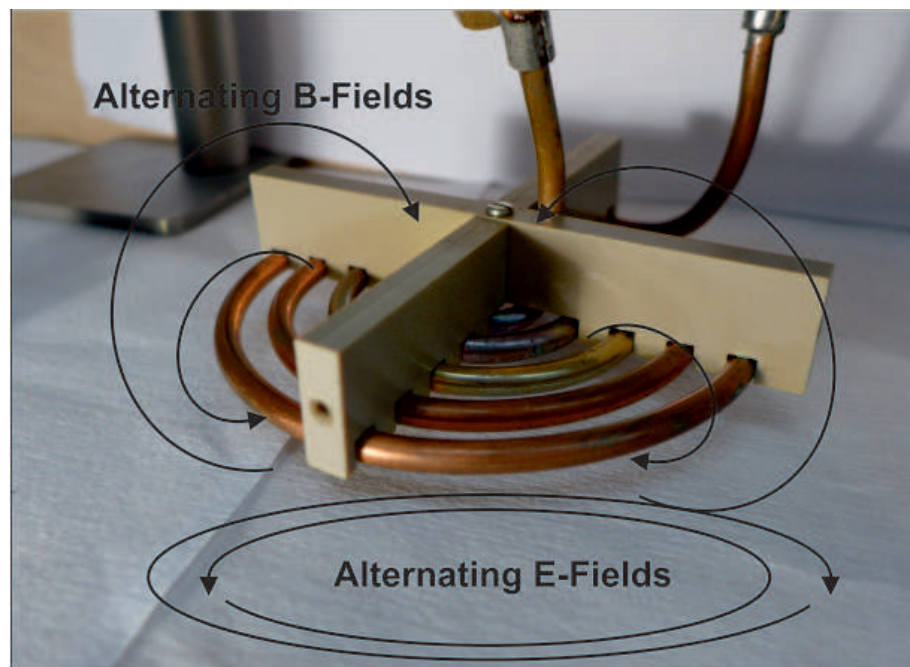


Figure 2.1: Electric (E) and magnetic (B) fields in the planar ICP configuration, with field lines and direction indicated by the arrows

applied to space propulsion research (e.g. ion thrusters). A key factor is the high density, low pressure plasma created in an electrodeless environment. Minimising the constraints capacitively coupled plasma (CCP) experience with RF sheaths.

Inside an ICP, electron heating occurs as the electric field excites the plasmas electrons at a skin depth layer by ohmic and collisionless heating processes. These occur when electrons in the bulk of the plasma encounter the oscillating inductive electric field.

The collisional part of the absorbed power is defined by the electron-neutral collision frequency which occurs within the induced RF field. For applications in manufacturing the increased gas temperature will have a direct effect on the gas density. The work of Godyak and colleagues showed the main mechanism for gas heating at low pressure (< 5 Pa) is the energy transfer from an ion to atom due to a charge exchange collision. At higher pressures it is due to electron collisions [23].

2.3.1 Plasma sheath

The function of a sheath in a vacuum system as considered in this work is to confine the more mobile species, in this case electrons by forming a potential barrier. This prevents electrons from escaping to the walls and leaving the system with a net positive charge. So

a barrier allows an equal number of positive and negative charge carriers to reach the wall to maintain a net zero charge within the plasma bulk [17].

When starting to apply RF power to the matching box and coil, a small amount of current will produce a capacitive or E-mode plasma. One of the main defining elements for a CCP is the sheath that is formed in front of the coil, in the same way it would for a planar CCP set up. The sheath formed in this mode has the largest variation, where the PROES emission in figure 3.6 illustrates the excitation and collapse of the sheath under these conditions. The electron heating during an RF cycle in the capacitive mode occurs when the sheath is expanding, which can be seen in figure 3.7, and thus accelerates the electrons due to this expansion [24, 25].

The onset of the E-H mode transition requires different voltages depending on the operating gas mixture; for a pure oxygen plasma it requires higher voltages when compared with a pure argon plasma, this is due to higher collision frequencies creating larger energy losses [26]. The transition characteristics can be very different with argon exhibiting a more step like transition whereas a more gradual transition is observed for oxygen. Electron temperature is also influenced by the increasing gas pressure, this is due to an increase in the number of inelastic electron-heavy particle collisions resulting in a decreased electron temperature [27].

A pure inductive mode (H-mode) has a very different excitation pattern, due to the electric field influence as shown in figure 2.1. The sheath voltages are much lower and plasma density higher, the transition between the two modes can happen gradually or produces a more step like process, again this depends on the gas and pressure of the system.

The industrially relevant region of interest is focussed at the plasma-surface interface on the lower electrode, the aim is to develop a novel technique to measure species densities within this region. The sheath that forms at the lower electrode is again influenced by the plasma mode. The flux of ions to the lower electrode does depend on a number of the plasma bulk conditions, such as the plasma density; specifically at the sheath edge, as well as the energy of the ions. The power deposited into the plasma in either of the operational modes will have an influence on the plasma density and whether the lower electrode is grounded or floating will influence this behaviour.

The plasma potential and charged particle density profiles as shown in figure 2.2 with the key reference parameter being its position to the wall or boundary of the plasma [14]. The plasma potential is described by the red line figure 2.2 and shows the potential profile that starts positive within the bulk of the plasma but reaches zero at the wall, which is grounded, as the net charge density of the sheath region is positive. This quantifies the behaviour of a collisionless sheath with the decreasing electron density n_e , as the electric fields within the sheath deflect the electrons back into the plasma bulk. Therefore, the highly negative wall potential with respect to the plasma potential attracts the positive ions $n_{i,+}$ that pass into the sheath and are accelerated towards the walls.

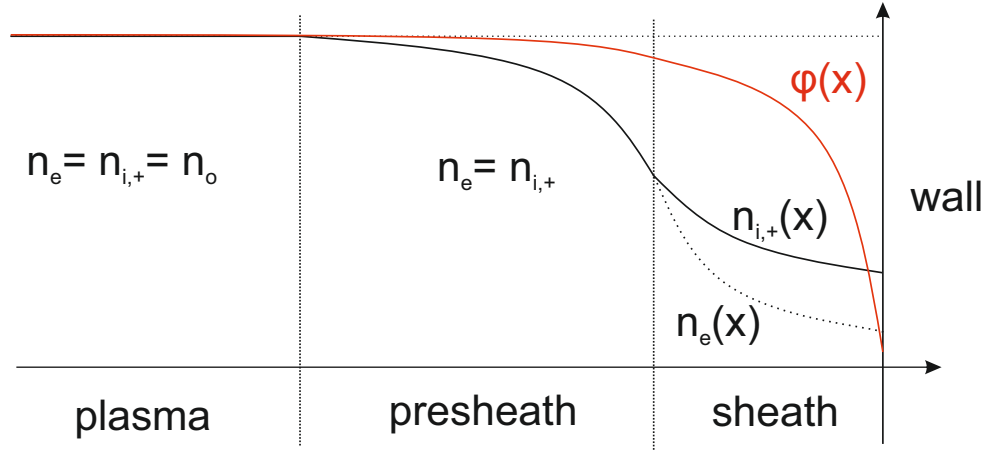


Figure 2.2: Charged particle density and electric potential representation, starting at the plasma bulk before transitioning into the sheath region and finishing at the reactor wall

The plasma behaviour up to the boundary can be defined in three stages, the first being the plasma bulk region where quasi-neutrality applies and the species densities can be defined as $n_e = n_+ = n_0$ this refers to similar densities where the plasma potential is at a constant value. When ions enter the pre-sheath region they require a threshold energy to surpass the Bohm criterium and enter the sheath [28]. Furthermore, the wall has a negative potential with respect to the bulk plasma so the electrons are repelled and a decrease of n_e can be observed. Ions have an opposite charge and are therefore attracted by the large negative potential, resulting in the sheath region boundary containing mostly positive ions n_+ leading to an in-balance in the local space charge. However, when referring to the plasma bulk quasi-neutrality is preserved.

2.3.2 Ion Energy Distribution Function (IEDF)

The ability of a technological plasma to provide a highly advanced surface treatment has been very advantageous for the manufacturing of semiconductors. The key process control for deposition or etching is tailoring of the energetic ions with respect to their flux and energy, however modern plasmas are capable of high plasma density and variable ion energies depending on the manufacturing process. Every etching or deposition application phase will be highly dependent on process control and monitoring of the plasma's interaction with the surface to provide a predictable and repeatable outcome [29]. The experimental configuration used in this research will focus on the ions produced around the lower electrode. This region of interest is where a sample would be placed in a similar manufacturing plasma. During the experimental phase a number of different signal waveforms will be produced at this electrode and it is important to assess whether ions are heavily influenced by these external waveforms as any variation in ion energies can damage fine surfaces formations, this will be explored further in chapter 5 [30].

The system conditions provide the ion energy parameters, these include the plasma potential and sheath voltage drop. But further loss mechanisms include scattering and charge exchange, where scattering causes the ion to lose some energy due to a neutral being in its path and charge exchange is involved in a transfer of its charge to a neutral that subsequently causes a fast moving neutral and much slower ion. Both of these loss mechanisms detract from the ions energy and also trajectory. The type of sheath produced by either a capacitive or inductive plasma will provide a difference in the sheath voltage. This can be further modified by applying a bias voltage to the substrate [31, 32]. The degree of collisionality (α) in the sheath can be given by the number of collisions in a Debye length.

$$\alpha \equiv \frac{\lambda_D}{\lambda_{mfp}} = \lambda_D n_g \sigma_s \quad (2.3)$$

Where (α) is proportional to the background gas density (n_g) and the mean free path of ions (λ_{mfp}) as expressed in equation 2.4, σ_s is the cross section at the ion acoustic speed [33]. The mean free path will vary depending on the background gas density as the system pressure is varied between 1 and 250 Pa.

$$\lambda_{mfp} = \frac{1}{n_g \sigma_s} \quad (2.4)$$

If we consider a higher system pressure where the ion-neutral collisions are more frequent, the IEDF will consist of more low energy ions. As mentioned earlier this occurs when ions transitioning through the sheath experience either scattering or charge exchange collisions. A collisional sheath $\alpha = 1$ consists of a short enough Debye Length or suitably high gas density while a collisionless case $\alpha = 0$ is the limit of the zero gas density. In plasma material processing applications requiring energetic ion bombardment or control of the time-averaged IEDFs to the plasma-surface interface it is key to discriminate between processes that require different threshold energies; plasma deposition requires lower thresholds so as not to damage fine structures where higher system pressures or longer processing times are considered. In the case of etching applications the system is also highly dependent on pressure, power and gas mixture, the density of neutrals at higher pressures will inform the rate of collisions resulting in ions with larger deflection angles [34]. Figure 2.3 shows two cases, one with sidewall damage caused by ions not bombarding perpendicular to the substrate. Quantifying these collisions in the sheath on a GEC reference cell for an E-mode (capacitive) and h-mode (inductive) plasma will highlight the system changes in later chapters when investigating tailored voltage waveforms [35].

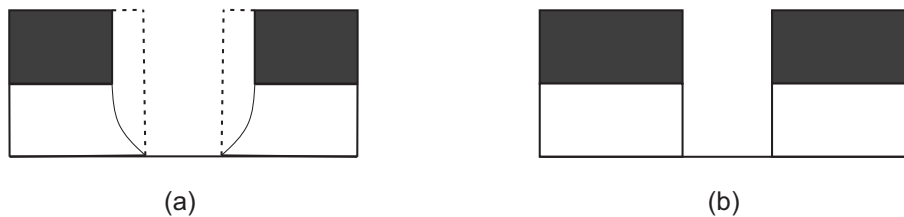


Figure 2.3: Isotropic etching (a) for when sidewall slope doesn't matter and to undercut the mask for easy removal and (b) completely anisotropic etching; preferred pattern transfer method for nano and atomic scale processes

The main requirement by industry is to ensure that any process is performed with high repeatability regardless of batch scale. Careful consideration must be given to the collisional effects in the sheath as these will influence ion energy and fluxes. In order to illustrate the role of sheath collisionality in defining the IEDF. Measurements of high and low plasma powers have been compared, with two system pressures of 5 and 10 Pa in a

98% oxygen and 2% argon plasma. These measurements help to visualise the large ion energy difference within the two plasma operation modes (E and H mode) as well as the increased sheath collisionality at the higher 10 Pa pressure.

Figures 2.4 (a) and (b) show ion energy distribution function trends with a floating lower electrode. The distribution function properties for these cases are summarised in table 2.1. The plasma was operated at powers of 100 and 1000 W with a fundamental driving frequency of 13.56 MHz, the dotted black lines represent E-mode measurements (100 W) and red dotted lines the h-mode IEDF measurements (1000 W). A complete description of the equipment used for these measurements is given in chapter 3.

Figure 2.4a illustrates the ion energy and flux measurements in a 5 Pa system operating the plasma at low power (black dotted line) with an ion energy of 18.6 eV, when compared with figure 2.4b at a higher pressure the ion energy is further reduced by the additional collisions experienced in the sheath along with the flux of ions now reaching the probe surface. In the higher power case (red dotted line) a significant ion energy and flux increase is observed, noting that for the h-mode (red dotted line) measurement in 2.4b an additional collision contribution in the form of a broadening can also be observed.

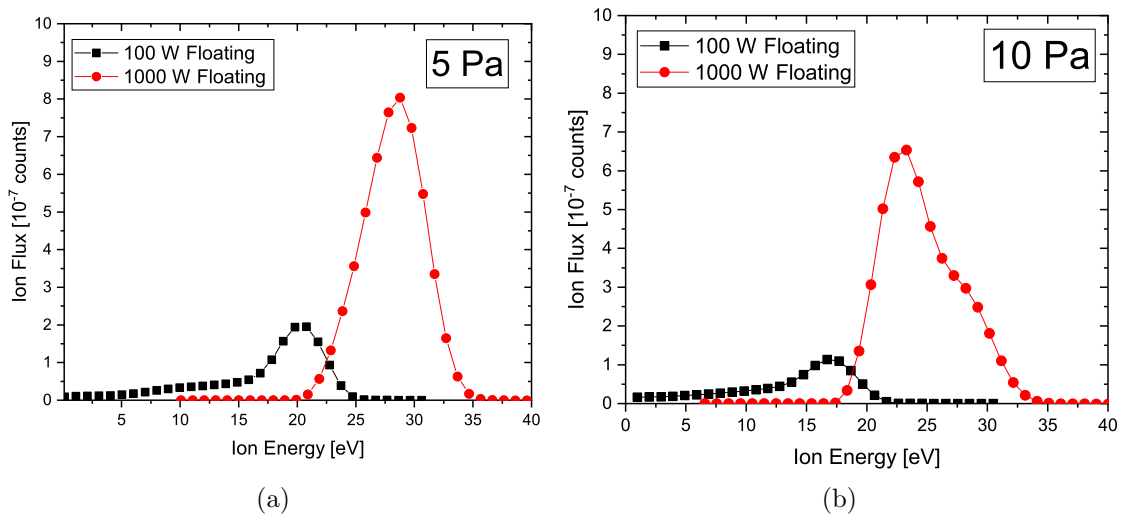


Figure 2.4: Floating lower electrode comparison of a 100 W E-mode (black dotted lines) to 1000 W H-mode (red dotted lines) IEDFs at 5 Pa (a) and 10 Pa (b)

In general, at lower pressure the degree of collisionality is also lower as illustrated in equation 2.3, this exhibits higher ion energies for both E and H mode plasmas as ions experience less collisions as they move through the plasma sheath ((n_g) background gas

density is lower). In addition, the IEDF has more low energy ions in E-mode compared to H-mode, as the plasma sheath is larger and the ions have more collisions within the sheath. In H-mode, the sheath is smaller and with less of the low energy ions this results in a pronounced peak at an energy equal to the plasma potential.

	E-Mode		H-Mode	
	Ion Energy	Ion Flux	Ion Energy	Ion Flux
<u>5 Pa</u> Floating	18.6 [eV]	1.26 [A/m^2]	27.9 [eV]	4.51 [A/m^2]
<u>10 Pa</u> Floating	16.4 [eV]	0.82 [A/m^2]	24.2 [eV]	4.11 [A/m^2]

Table 2.1: Ion energies and fluxes in an ICP plasma driven at 13.56 MHz, with a floating lower electrode at 100 and 1000 W with pressures of 5 and 10 Pa, gas mixture is 98% O₂, 2% Ar.

Figure 2.4 measurements illustrate a significant ion energy shift between the low power capacitively driven plasma and high power inductive scenario. This consideration will need to be examined further when a tailored voltage waveforms are applied to the same region. As significant ion energy and flux influence with negate any benefits from the diagnostic.

Chapter 3

Diagnostic and experimental configuration

This chapter describes the experimental set-up of the chamber and associated diagnostics used throughout this research project. The plasma reactor used in this work is hybrid inductive/capacitive Gaseous Electronics Conference (GEC) reference cell, where the capacitive (lower) electrode can be operated in a grounded, floating or powered mode. The setup of this system and implementation of various diagnostics (laser spectroscopy, phase resolved optical emission spectroscopy and retarding field energy analysis) on this system will be introduced.

3.1 Experimental configuration

The experimental set-up consists of interchangeable diagnostics and the hybrid inductive/capacitive plasma source is capable of various modes of plasma operation. The primary diagnostic tool used is a high temporal resolution ICCD camera (Andor, iStar) positioned to capture emission from the plasma discharge region, the camera is aligned to one of the two large windows, which are 225 mm in diameter, to give a clear view of the whole inter-electrode gap. The four smaller ports provide access for a pressure gauge (MKS, Baratron), Retarding Field Energy Analyser (Semion, RFEA) and modular spectrometer (Ocean Optics, HR series) fibre feed through. A nanosecond resolution laser system (Continuum Surelite laser and Horizon OPO) is also focused across the electrode

region to provide absolute density measurements of atomic species using Two Photon Absorption Laser Induced Fluorescence (TALIF). Together, these diagnostics allow for the measurement of atomic species densities, time resolved electron dynamics and ion energies incident on the substrate electrode.

3.1.1 Chamber geometry

The chamber geometry used in this work is a hybrid Gaseous Electronics Conference (GEC) reference cell [20, 36]. A schematic of the chamber and basic operating components is illustrated in Figure 3.1. Inductive power is coupled through a 5 turn copper coil positioned at the top of the cell. Power can also be capacitively coupled through a cylindrical lower electrode. The inductive coil consists of a hollow pipe measuring 3/16" in diameter which is water cooled at $20 \pm 0.1^\circ\text{C}$ through the centre of the copper tube. An automatic matching box (Advanced Energy, RF Navio) is affixed to the top of the reference cell and connected to the copper coil which passes through the top of the chamber. The coil rests against the quartz window which is vacuum sealed to the surrounding chamber.

The lower electrode is based on the capacitively coupled plasma electrode geometry used in the work of Olthoff and colleagues [37]. For this work the lower electrode is not powered by an RF source and is instead either grounded, floating, or powered by the tailored ns-pulse waveform described in section 5.1.2. The lower electrode is cylindrical, surrounded by a grounded guard ring, as illustrated in the inset shown in figure 3.1, and is water cooled through the bottom to a constant temperature of $20 \pm 0.1^\circ\text{C}$. The total diameter of the lower electrode is 120 mm including the guard ring, and the distance between the powered electrode and the top quartz window is set at 43 mm. The two-dimensional CCD chip of the Andor iStar camera contains a square block of 1024 x 1024 pixels each with a size of $13 \times 13 \mu\text{m}$, once focussed on the discharge region this offers spatial resolution up to the image intensifiers limit of $30 \mu\text{m}$. The resolution of a typical PROES measurement is $157.4 \mu\text{m}$ for two-dimensional images. This image includes the whole of the top electrode plus stainless ring (165 mm) and the discharge region including an additional 3 mm of each electrode, resulting in a total vertical image axis of 49 mm.

The chamber is pumped down to typical operating pressures of 10 - 250 Pa using a rotary-slide-vane pump (Pfeiffer Vacuum, Duo 20MC). Lower pressures (1 - 10 Pa) are also

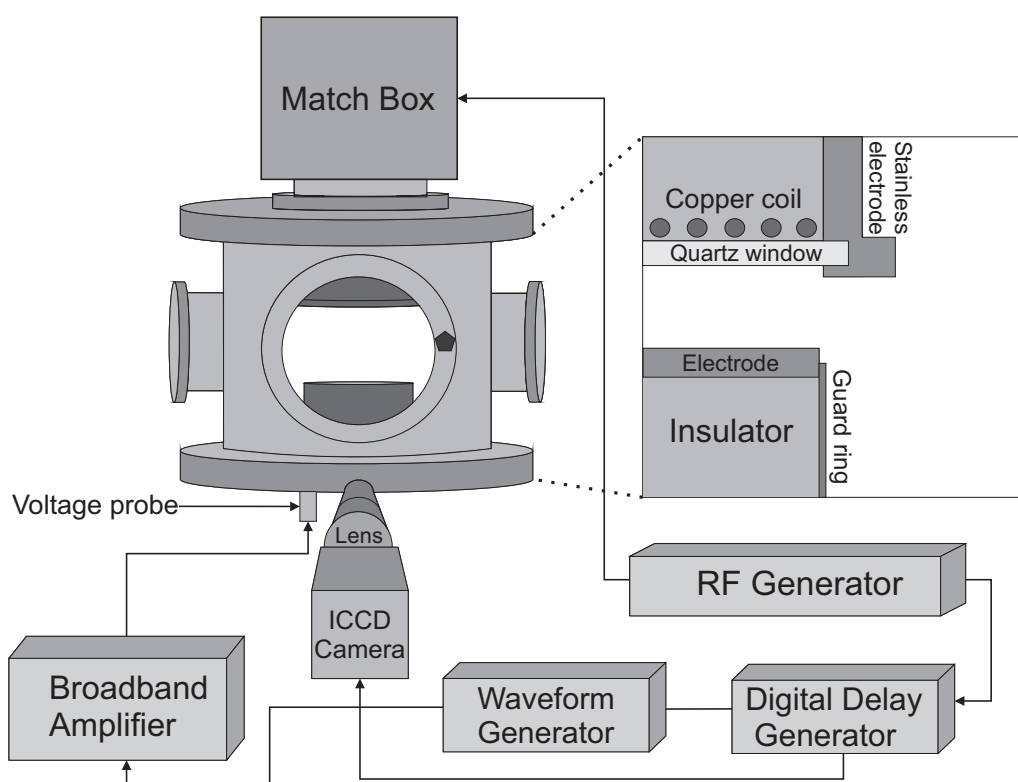


Figure 3.1: Schematic of the GEC, with RF and pulse generation mechanisms. A voltage probe measures the amplified pulse at the lower electrode and nanosecond resolution camera to capture pulse induced OES

attainable through the use of an additional turbo molecular pump (Oerlikon, Turbovac MAG W 600iP). The system pressure is regulated via a throttle valve (MKS 253A). Gas is fed into the system through a variety of MKS mass flow controllers (MKS, GE250A, GE50A, 1179A) these allow for the use of different gas mixtures, of either Ar/O₂ or He/H₂.

In this chapter a description of how electrical components and diagnostics are applied to the GEC reference cell is described, in order to monitor plasma changes as the operating conditions are varied.

3.1.2 Electrical components

The electrical set up is also illustrated in figure 3.1 with a fixed frequency 13.56 MHz (Advanced Energy Cesar 1310) generator used to drive the inductive coil. It also acts as the sync reference source to which all the other electrical components are synchronised. The 13.56 MHz generated RF waveform is fed into the automatic matching unit (Advanced Energy, RF Navio) which quickly and repeatedly matches the plasma impedance to the

set operational range. This occurs so seamlessly as both units are designed and manufactured by Advanced Energy, this was an intentional system upgrade part way through my research, due to the previous system not maintaining impedance matching for longer measurements.

A Transistor-Transistor Logic (TTL) output trigger amplitude from the Cesar 1310 RF generator is fed into a digital delay generator (Stanford Research Systems DG 645), which scales the signal to a user specified repetition rate (<500 kHz) for triggering of the Andor camera (Andor iStar DH344T-18U-73). The highest synchronisation frequency used in this work is 452 kHz (as the camera is limited to 500 kHz). The chosen repetition frequency is a multiple of the 13.56 MHz driving frequency, which ensures that the plasma and the camera do not drift with respect to one another in time. This can be decreased to allow longer time steps between each camera image acquisition. The camera is then in sync with the output of the RF generator and phase resolved images of the plasma emission across the discharge region can be observed. A voltage probe (Tektonix P5100A) is attached to the underside of the lower electrode in order to provide in situ voltage measurements on the oscilloscope (LeCroy WaveSurfer 104MXs-B 1 GHz 10 GS/s).

3.2 Diagnostic techniques

The diagnostics presented are focussed on increasing the fundamental understanding of different aspects of the plasma, including the electron dynamics using Phase Resolved Optical Emission Spectroscopy (PROES), this is possible due to ultra-fast optical techniques which allow the nanosecond resolution of plasma emission within the RF cycle to be captured. Selecting appropriate emission lines and correlating specific electron dynamic data with observed emission allows the plasma dynamics to be monitored when additional processes are applied to the GEC system. Energy Resolved Actinometry (ERA) allows the simultaneous measurement of atomic oxygen densities and local mean electron densities to characterise regions of interest for manufacturing processes, it uses PROES data to analyse and configure the measurements. In order to validate the ERA calculation, Two Photon Laser Induced Fluorescence (TALIF) provides quantitative atomic species densities in regions of the GEC cell it can be calibrated for. Measurements will be carried

out under different gas mixtures and powers, including studying the E-H transition of the ICP. Ion energies and fluxes will be measured at the lower electrode using a Retarding Field Energy Analyser (RFEA) placed on top of the lower electrode and operated to characterise the plasma operation via a broad parametric variation. The aim is to develop monitoring and optimisation tools, to better understand how the ion energies/fluxes and neutral properties vary over a wide range of operational parameters.

3.2.1 Retarding Field Energy Analyser (RFEA)

For measuring the ion energy distribution function (IEDF) and ion flux at the plasma-surface interface, an RFEA (Impedans, Semion system) is placed on the lower electrode with the probe and outer casing covering the whole 102 mm electrode surface, this excludes the outer guard ring.

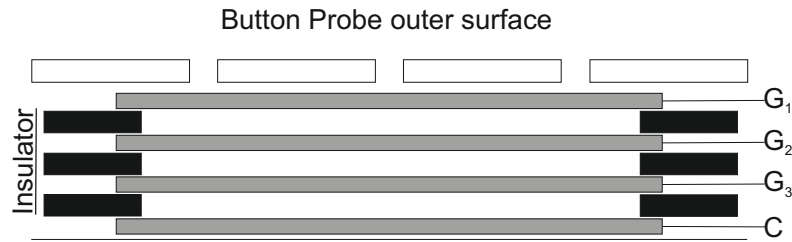


Figure 3.2: Schematic of the RFEA probe with grids (G_1 to G_3) and collector plate (C) as illustrated

The button probe used in this work is shown in figure 3.2 with a series of openings that allow a sample of ions to enter into the grid system, the probe is connected to the surface of the electrode electrically and therefore floats at the same potential experienced by the surface. The figure only illustrates part of the grid system with a whole button probe being made up of a series of $800 \mu\text{m}$ holes and a total probe grid system diameter of 33 mm. The button probe sits inside an anodised aluminium holder with the same thickness as the button probe and an outer diameter of 102 mm to cover the rest of the electrode surface. The holder is used to keep the surface of the probe exposed to the plasma flat to avoid disturbing the plasma. The probe consists of a series of grids to prevent electrons reaching the detector and help discriminate between ions with different energies. The first is G_1 which is electrically connected to the underside of the probes upward facing surface,

to sample the area and minimise the effect of the probe on the plasma sheath. The next stage G_2 is negatively biased to -60 V DC relative to the bias voltage measured through the probes feed through box. This grid repels electrons that have also entered through the holes on the surface. The third grid G_3 is used to discriminate ions. This is done using a potential sweep from the bias voltage measured using a multimeter to a value approximately 50 V above this dc bias voltage. C represents a collector plate that is a negatively biased to repel electrons and collect only the ion current at each value of the voltage on G_3 . By varying the voltage on G_3 and collecting the current at C, the RFEA produces a current voltage curve. By differentiating this curve the current of ions at each energy is obtained. The integral under the IEDF curve also gives the total ion current, this is demonstrated in figure 3.3.

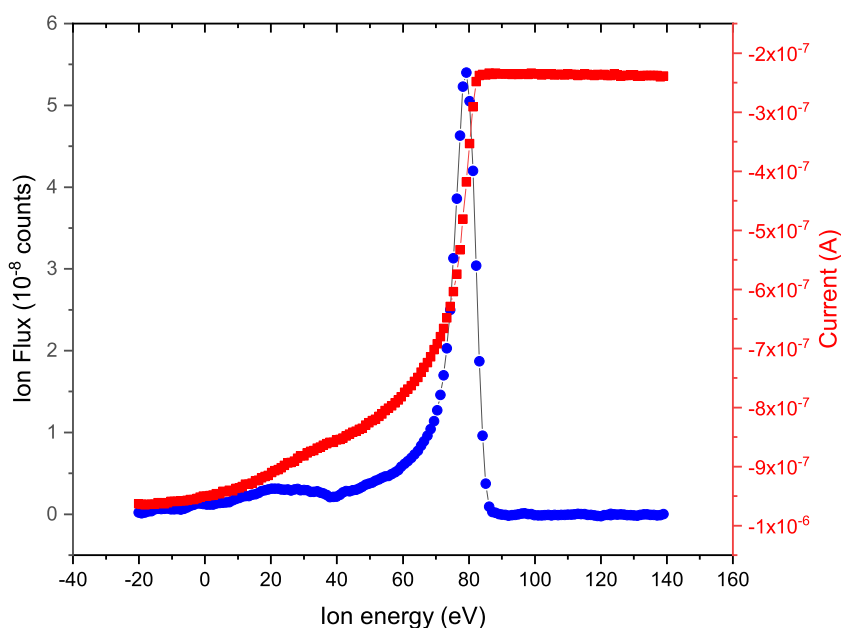


Figure 3.3: Sketch of a typical current voltage curve produced during a defined voltage range sweep (-20 to 140 eV) with associated current values

The RFEA used in this work is limited to certain operational parameters as stated by the manufacturer, during this work it is operated up to its maximum pressure of 12 Pa.

3.2.2 Optical emission spectroscopy

Optical emission spectroscopy (OES) is commonly used to investigate the properties of plasmas [11, 38, 39]. In OES, the fluorescence of an excited state, populated by electron

impact in the plasma is detected and related to plasma properties, such as electron temperatures or atomic species densities, using a model. An advantage of using OES to measure atomic species densities is that it is a passive approach that does not require physical access to the plasma device therefore it will not directly interfere with the discharge, which is a critical component for any potential diagnostics looking to be implemented into a processing plasma [40]. OES is used to determine conditions in specific regions of the plasma, however it relies on stable and consistent emission which is caused by fast dynamic excitation processes involving energetic electrons. In this work, OES will be used to measure the densities of atomic oxygen and the mean electron energy in the plasma using Energy Resolved Actinometry (ERA). This section will introduce the theory behind OES, conventionally used actinometry approaches, and ERA, and describe how ERA is applied to the GEC reference cell in this work.

3.2.3 Population of excited states

For low pressure, low temperature plasmas with electron densities typically around 10^{14} to 10^{15} m^{-3} the corona model provides a simplified approach to describing the population of excited states through electron impact excitation, in which the excitation into a state is only produced by electron impact excitation and de-excitation processes also only occur due to spontaneous emission into lower states [41] thus providing a very simplified model.

$$\frac{dn_i(t)}{dt} = n_0 k_e n_e - \sum_k A_{ik} n_i(t) \quad (3.1)$$

Here, n_i is the density of atoms in the excited state i , n_0 is the density of atoms in the ground state 0 , k_e is the electron energy dependent excitation rate coefficient and n_e is the electron number density which is equal the excitation rate $E_i(t) = k_e n_e$, A_{ik} is the Einstein coefficient for spontaneous emission from state i to a lower state k . Figure 3.4 shows an illustration of this process. It also includes the extension of the corona model into a basic collisional radiative model by accounting for quenching; which has an influence on the state i . Other processes that are discounted in this model are cascade processes from higher energy states and electron impact excitation from metastable states [42, 43].

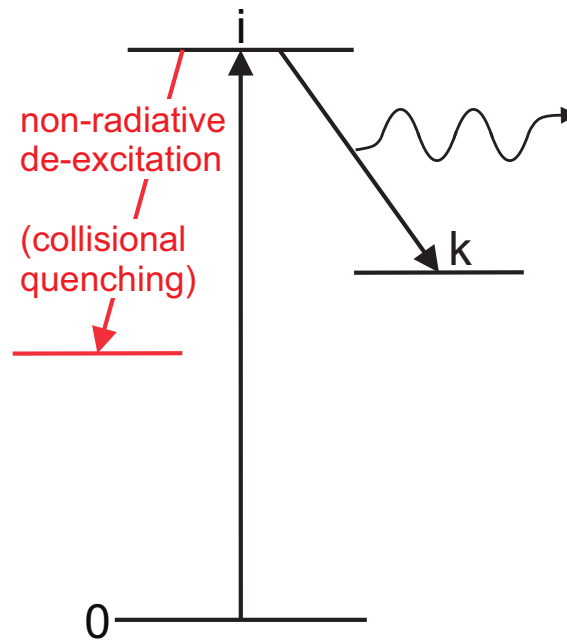


Figure 3.4: Sketch illustrating the population dynamics of the excited states (i and k) in a plasma. The basic corona model is shown in black, while the red lines and text illustrate the extension to the basic collisional radiative model with the addition of non-radiative de-excitation (quenching).

3.2.4 Phase resolved optical emission spectroscopy (PROES)

The measurement of plasma emission from RF plasmas can either be time and space integrated using, broadband spectrometers, or time and space resolved using high resolution cameras. The time and space resolved approach is known as phase-resolved optical emission spectroscopy (PROES). Figure 3.5 illustrates the basic methodology for carrying out the PROES measurements with an Intensified Charge Coupled Device (ICCD) camera (Andor iStar DH344T-18U-73), the camera's CCD chip is made up of a 1024×1024 square pixel array. In this work the gate width has been set to 2 ns which is above the cameras limit of 1.9 ns. The camera is focussed on the centre point between the two electrodes such that it views the entire discharge region. In practise the PROES measurements are performed by synchronising the gate width with the RF generators used to produce the plasma. The maximum synchronisation frequency of the camera is 500 kHz, as such, the frequency of the signal used to synchronise the function generator with the camera were all below this value (i.e 452, 226 and 113 kHz). These values were chosen as they are harmonically related to 13.56 MHz and as such allow for a constant phase relationship to be maintained.

The synchronisation signal between the RF generator and camera is passed via a Digital Delay Generator (DDG) (Stanford Research Systems DG645), this allows for a variable delay to be added to the trigger signal. Once the camera detects the trigger signal it opens the gate and acquires an image on the CCD. This process will then happen continuously depending on the exposure time (typically a couple of seconds, but up to 10 s of seconds) and with a defined repetition rate (e.g 452, 226 or 113 kHz). During each signal acquisition an image builds up on the cameras CCD, once the exposure time has elapsed the image created on the CCD is exported and the 2 ns delay is increased so that the next image occurs 2 ns further along the same RF cycle (red dotted lines in figure 3.5), in this way a picture of the emission dynamics is built up throughout a 74 ns RF cycle which equates to 37 images, these are stitched together as per figure 3.6.

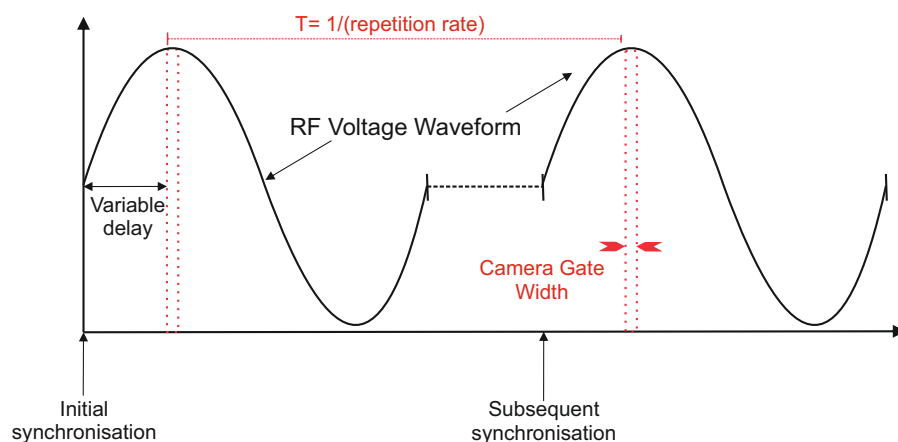


Figure 3.5: Illustration of the PROES principles and how they are obtained experimentally by varying the camera gate position.

The specific wavelength measured is either defined by a custom narrowband filter ± 0.5 nm (Andover Corporation) or broader filters with a range of ± 5.0 nm (Andover Corporation). The entire discharge region is imaged including both electrodes and focussed down onto the ICCD by a commercially available camera lens (SIGMA 18 - 200 mm F3.5 - 6.5II DC OS).

Figure 3.6 shows an example of the phase resolved emission measured using the procedure described above. In this case, the plasma is operated at a pressure of 5 Pa and power

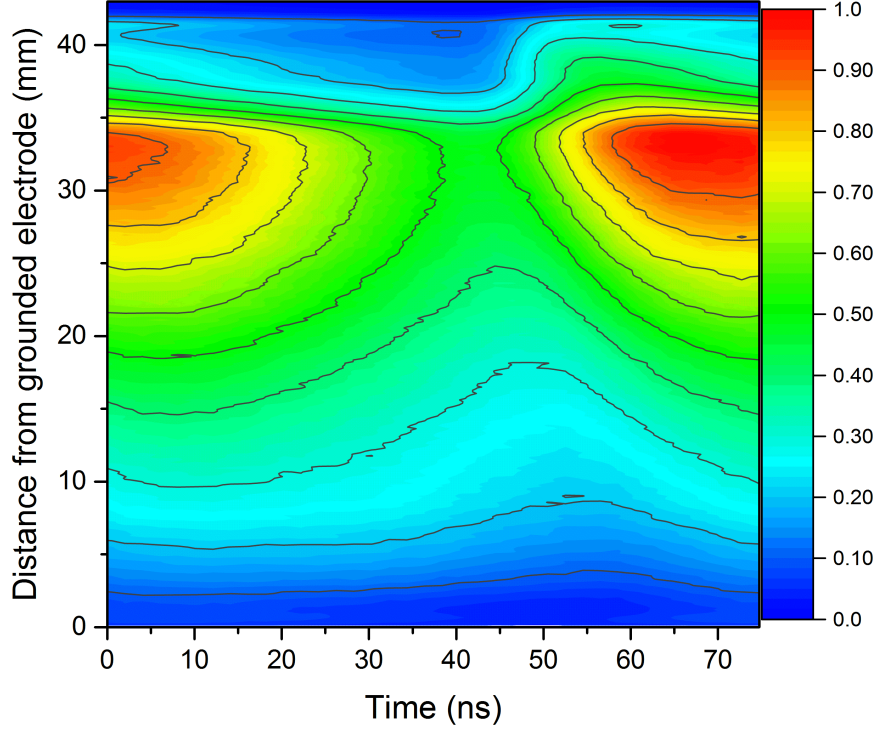


Figure 3.6: PROES measurement over a single RF cycle (74 ns) using a 750 nm narrowband filter to capture emission from an oxygen/argon plasma operated at 100 W and 5 Pa.

of 100 W applied to the inductive coil. The gas mixture is 1:2 O₂/Ar, emission intensity is observed at 750 nm using a narrowband 750 nm filter, corresponding to fluorescence from the Ar(2p₁) state relaxing to the Ar(1s₂) state. Monitoring the emission illustrates the dynamics of electrons above the threshold for excitation of the Ar(2p₁) state (13.48 eV). In Figure 3.6 the phase resolved emission at 750 nm has one excitation structure per RF cycle which begins at the point of highest emission (~ 65 ns). This emission structure illustrates the expanding sheath motion in an E-mode plasma where electrons are accelerated away from the coil by the expansion of the plasma sheath once per RF cycle. The dynamics of electrons observed in PROES under different operating parameters will be discussed further in Chapter 6.

The emission observed from PROES $I_i(x,t)$ can be converted into the electron impact excitation using the collisional radiative model. The equation for the excitation of state i , E_i , is shown in equation 3.2 [44].

$$E_i(t, x) = \frac{1}{n_0 A_{ik}} \left(\frac{dn_i(t, x)}{dt} + A_i n_i(t, x) \right) \quad (3.2)$$

The measurement of photons per unit volume and time is related to the excited state density $n_i(t, x) = I_i(t, x)/A_{ik}$ and includes the transition probability A_{ik} of emission from the higher excited state i to the lower state k . The ground state density is represented by n_0 . Where, k_{iq} denotes the rate coefficient for collisional quenching of excited state i via collisions with species of density n_q . The quenching coefficients in table 3.1 assumes molecular oxygen is the main quencher. Equation 3.3 is the effective decay rate A_i of excited state i and depends on a spontaneous emission, radiation trapping and quenching. Where, g_{ik} is the escape factor of the radiation, For the work presented here, the escape factor is approximately equal to one $g_{ik} \approx 1$ as the plasma is optically thin, meaning no re-absorption of the emitted light (750 - 844 nm) of interest for this work.

$$A_i = \sum_k A_{ik}g_{ik} + \sum_q k_{iq}n_q \quad (3.3)$$

Figure 3.7 shows the emission data from figure 3.6 calculated using equation 3.2 to illustrate the time and space resolved electron impact excitation of the Ar(2p₁) state. The main difference between the time and space resolved emission and excitation is that the excitation maximum is focused to a shorter time period, due to the associated lifetime of the emission. As a result, the pattern of the spatially and temporally resolved excitation features synonymous with oxygen discharges in an ICP configuration are observed.

In this work, three emission lines are used in Ar/O₂ plasmas to calculate the mean electron energy and atomic oxygen density using ERA, described later. Table 3.1 shows the excited atomic states, radiative lifetimes and quenching coefficients of these emission lines.

Wavelength (nm)	Atomic state	Radiative life-time (ns)	Ref.	Quenching coefficient (10 ⁻¹⁶ m ³ s ⁻¹)	Ref.
750.46	Ar(2p ₁)	22.5±0.7	[1]	7.6	[1]
777.45	O(3p ⁵ P)	27.1	[45]	10.6	[3]
844.79	O(3p ³ P)	34.7 ±1.7	[2]	9.4	[2]

Table 3.1: This table highlights the emission wavelength, radiative lifetimes and quenching coefficients of the atomic states used in this work.

The two-dimensional measurements for each of the emission wavelengths will be carried

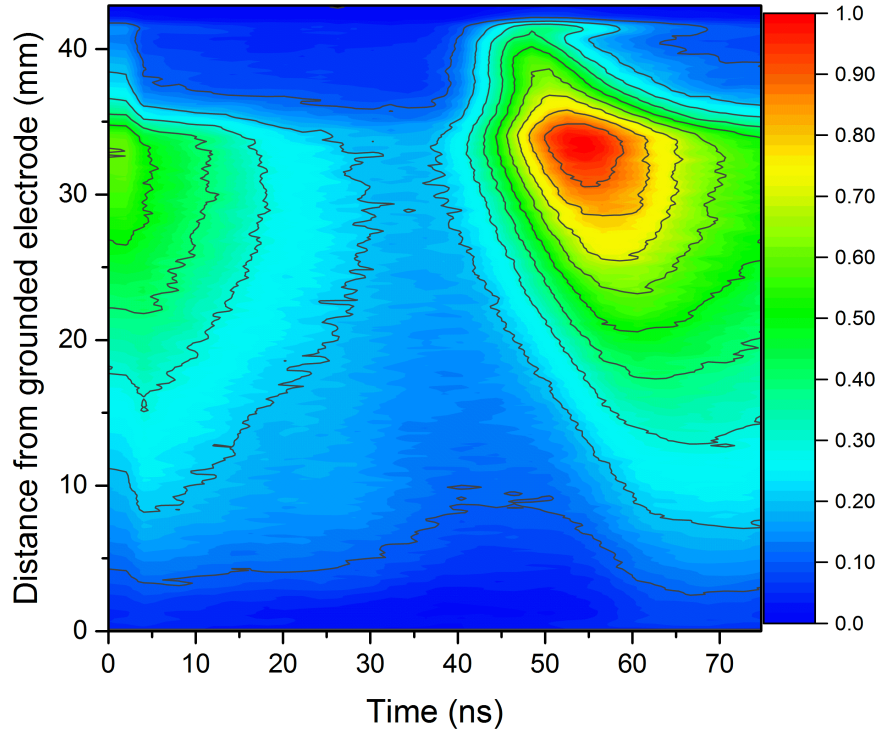


Figure 3.7: The excitation plot is calculated using equation 3.2 from the PROES measurements in figure 3.6

out using precision optical narrow bandpass filters (Andover Corporation), with custom wavelengths to get precision selectivity at the specific wavelengths in table 3.1. Argon at 750.46 ± 0.50 nm and oxygen at 777.45 ± 1.75 nm and 844.79 ± 0.95 nm.

3.2.5 Classic actinometry

Actinometry is a technique for quantifying reactive species concentrations of various gases such as O, N or H. The classic approach calculates the atomic density using the ratio of the emission intensity as shown in equation 3.4. Using a noble gas as an actinometer it enables the emission intensity to be converted into relative number densities.

$$n_O = \frac{I_{O,844}}{I_{Ar,750}} \frac{h\nu_{Ar,750}}{h\nu_{O,844}} \frac{k_{Ar,750,d}}{k_{O,844,d}} \frac{a_{ik,Ar,750}}{a_{ik,O,844}} n_{Ar} \quad (3.4)$$

Here I_O is the time averaged emission intensity of the oxygen 844 nm excited state, $h\nu$ denotes the photon energy, k_O is the atomic oxygen excitation rate coefficient, a_{ik} is the optical branching ratio. Finally n_{Ar} is the argon ground state density. Under these conditions a ratio of the atomic oxygen 844 nm and argon 750 nm measurements

are compared, the atomic oxygen density is calculated under the assumption that both excited states have similar energies and that they are solely populated via direct electron impact excitation. [1, 46, 47]

3.2.6 Advanced actinometry

Advanced actinometry builds on the classical approach by including terms for direct electron impact and dissociative excitation processes. However this does require more specific knowledge of the EEDF as the O(3p³P) state has different thresholds for the direct and dissociative contribution [47–49].

Equation 3.5 includes a second term which accounts for both the direct (d) and dissociative (de) excitation from the 844 nm emission. Resulting in a more accurate density calculation.

$$n_O = \frac{I_{O,844}}{I_{Ar,750}} \frac{h\nu_{Ar,750}}{h\nu_{O,844}} \frac{k_{Ar,750,d}^*}{k_{O,844,d}^*} \frac{a_{ik,Ar,750}}{a_{ik,O,844}} n_{Ar} - \frac{k_{O,844,de}^*}{k_{O,844,d}^*} n_{O2} \quad (3.5)$$

Equation 3.6 describes the effective excitation rate coefficient (k^*).

$$k^* = \frac{\langle k_e n_e \rangle_{rf}}{\langle n_e \rangle_{rf}} \quad (3.6)$$

Equation 3.6 includes the direct (d) and dissociative (de) excitation rate coefficients. In this format, accurate results can only be calculated from states populated via electron impact excitation of ground state atomic and molecular oxygen. If the excited state is populated via other excitation processes it would skew the atomic oxygen densities derived using actinometry. The relevant assumptions will be developed more in the following.

3.2.7 Energy resolved actinometry

Energy resolved actinometry (ERA) is a technique based on direct and dissociative excitation processes. It builds on the previous actinometry technique by including a second oxygen line 777 nm O(3p⁵P) and also uses excitation ratios instead of the emission intensity ratios. This allows for the measurement of atomic species densities and mean electron energies simultaneously, the development of the actinometry technique has been discussed in detail by Greb et al [50]. The ICCD camera and GEC chamber are configured to provide

high spatial PROES images with ns temporal resolution of the region between the plasma electrodes, this allows the excitation rates for the specified excited states to be derived. These excited states are listed in table 3.1.

The excitation ratios obtained through experiment are then compared with the values calculated using a Maxwellian distribution function. The mean electron energy and dissociation degree are varied to match experimental conditions, leading to a comparison of both ratios and the measured mean electron energy and dissociation degree. For plasma processing applications it is then possible to calculate an absolute atomic species density relevant to the region associated with the plasma emission. This is calculated using the ideal gas law with a gas temperature value.

The direct and dissociative electron impact excitation of the oxygen emission lines as shown in figure 3.8 are accounted for by summing all the electron impact excitation rates $E_{i,n}$ that excite species n and end up in state i . The value for f_n is the fractional density of the species n in the gas;

$$E^* = \sum_n f_n E_{i,n} \quad (3.7)$$

Equations 3.8 and 3.9 are the effective excitation rates for the chosen emission lines. With the fraction of molecular oxygen f_{O_2} and argon as the actinometer gas f_{Ar} . The density of the atomic oxygen divided by the molecular oxygen produces the dissociation degree and is written as r_O in the following equations;

$$\frac{E_{750}^*}{E_{844}^*} = \frac{f_{Ar}}{f_{O_2}} \frac{r_O k_{750,d}(\epsilon) + k_{750,de}(\epsilon)}{r_O k_{844,d}(\epsilon) + k_{844,de}(\epsilon)} \quad (3.8)$$

$$\frac{E_{777}^*}{E_{844}^*} = \frac{r_O k_{777,d}(\epsilon) + k_{777,de}(\epsilon)}{r_O k_{844,d}(\epsilon) + k_{844,de}(\epsilon)} \quad (3.9)$$

The local mean electron energy ϵ corresponds to a Maxwellian electron energy distribution function. Figure 3.8 illustrates the cross sections for the direct and dissociative electron impact excitation, this graph highlights the need to include the dissociative contribution particularly for the 777 nm emission as the dissociative cross section becomes larger than the direct cross section at higher energies.

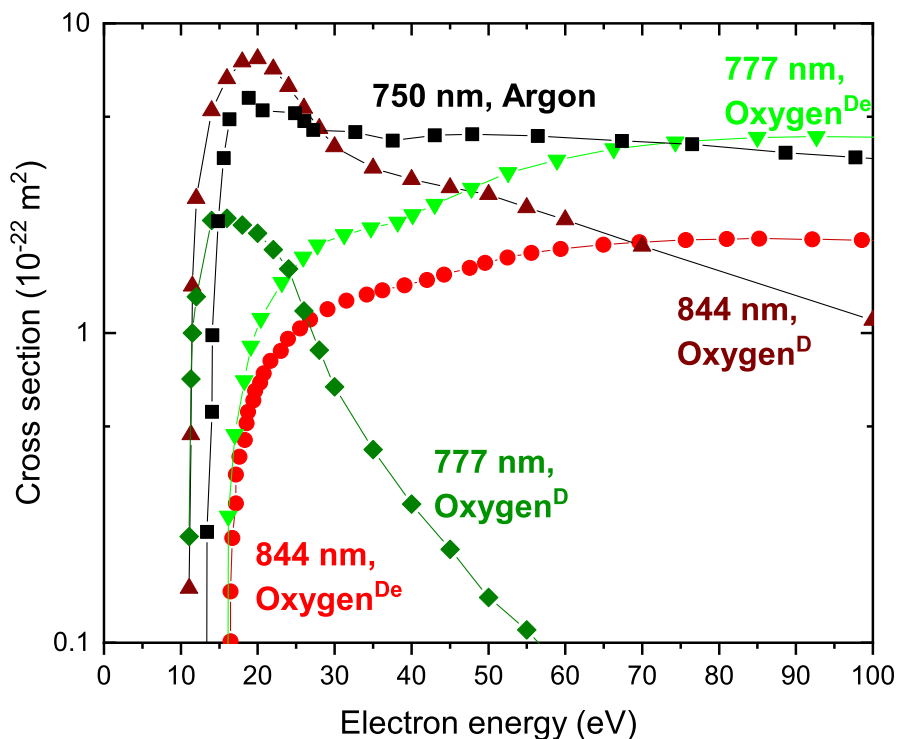


Figure 3.8: Electron impact cross section profiles of the excitation states used in this work (750, 777 and 844 nm). D and De refer to the direct and dissociative excitation respectively [1–3].

The thresholds for the two oxygen states are in the range of 10-20 eV, with the argon state ($\approx 13.48\text{eV}$) sitting approximately between the direct and dissociative levels. The different shapes of the cross sections for direct (D) and dissociative (De) excitation of 777 and 844 nm emission means that, there is a different dependency on the mean electron energy which is beneficial as it allows the mean electron energy to be obtained. The differing dependence of the Ar emission and the O emission on the dissociation degree allows the dissociation degree to be obtained.

To calculate the dissociation degree and the mean electron energy using ERA, the excitation ratios are obtained experimentally from PROES images of the different emission lines. This is carried out in a time and space region where the plasma emission is strong and electrons are being actively heated, such as at sheath expansion. This is key to ensure that electron impact is the dominant process exciting the states being monitored, and that other processes such as cascades or heavy particle excitation are not dominating. Experimental excitation ratios are then compared to those calculated using the cross sections plotted

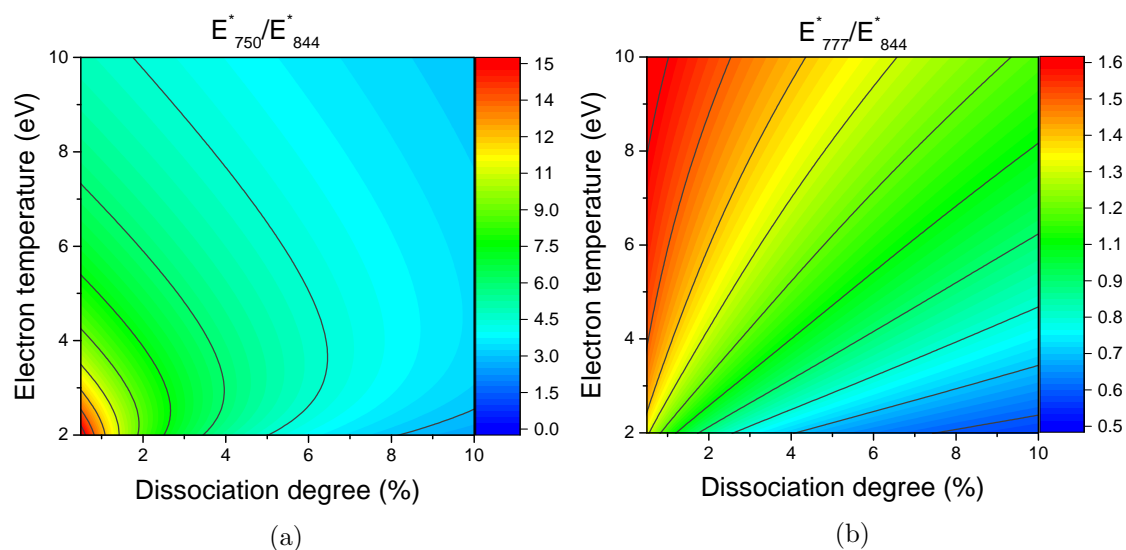


Figure 3.9: Calculated excitation ratios of the 750 and 844 nm line (a) and 777 and 844 nm line (b) as a function of dissociation degree and mean electron energy.

in figure 3.8 for varying mean electron energy and dissociation degree, these are shown in figures 3.9a and 3.9b.

The two excitation ratios are then combined as per figure 3.10 so that the contour lines can be compared over similar parameter space. Each contour line defines a constant value of the respective excitation ratio. The crossing points of the lines from the two different ratios defines a value of the dissociation degree and mean electron energy. By comparing the experimentally measured excitation ratios on this plot the experimental dissociation degree and mean electron energy can be measured.

The quantitative error analysis considers uncertainty in the electron impact cross sections used to simulate the excitation ratio values. These include the measured electron impact cross sections for direct excitation of $\text{Ar}(2p_1)$ at 20 % [51] as well as the dissociative electron-impact excitation of the $\text{O}(3p^5P)$ and $\text{O}(3p^3P)$ levels which are 15 % [48]. Reference [52] does not specify the uncertainty of the direct excitation of $\text{O}(3p^5P)$ and $\text{O}(3p^3P)$ however these are expected to be in the order of 30 %. Therefore the total minimum estimated uncertainty in the electron impact cross sections have been given as 30 %, as this accounts for the largest estimated uncertainty.

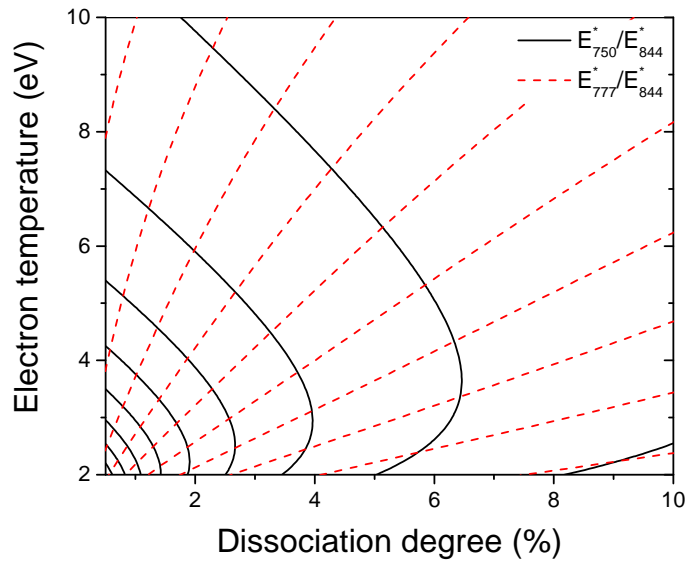


Figure 3.10: This plot represents an overlay of the contour lines for both the excitation ratios shown in figures 3.9a and 3.9b, these excitation ratios are obtained with a 98% O₂ and 2% Ar gas mixture.

3.3 Two-Photon Absorption Laser Induced Fluorescence

To validate the ERA technique and confirm the atomic species densities, Two Photon Laser Induced Fluorescence (TALIF) is operated over the same plasma conditions, it uses specific laser wavelengths to excite the chosen species and measure the wavelength specific fluorescence it produces [53]. This technique is expensive and alignment intensive however the results are accurate, reproducible and widely documented [47,54–57]. The laser system used in this work is a Continuum (Surelite laser and Horizon OPO) with mirrors and a focusing lens that confines the laser energy to a spatial region across the lower electrode, therefore allowing for spatial measurements of the plasma discharge region.

3.3.1 Laser Induced Fluorescence

Laser induced fluorescence (LIF) is an active diagnostic allowing for space and time resolved measurements of atomic ground state absolute densities in plasmas. It uses laser photons to excite species from the ground state into a higher energy one which then relaxes to a lower energy state emitting a photon which can be detected. With a suitable system calibration the absolute density of the ground state can be obtained.

As a number of the allowed optical transitions from the ground to higher energy states

lie in the vacuum ultraviolet (VUV) spectral range 100-190 nm, which increases the likelihood of it being absorbed by other species in the plasma. Alternatively a multi-photon approach can be used instead, this is based on using two or more photons whose energy will add up to the required amount but whose wavelength lies in the more accessible UV $\omega_1 + \omega_2 = \omega_T$ range. The trade off being two photons are less likely to be absorbed simultaneously and therefore larger laser intensities are required [58, 59].

3.3.2 Two-Photon Laser Induced Fluorescence

TALIF is a reliable and well characterised technique for resolving ground state densities, where experimentally determined quenching coefficients are used to correct for any collisional losses [2, 58, 60]. The concept of two-photon laser induced fluorescence (TALIF) as shown diagrammatically in figure 3.11, begins with atoms or molecules being excited from the ground state (E_1) by absorption of two photons from the probing laser beam and into the excited state (E_2), where it subsequently de-excites into a lower energy state (E_3) [58]. For TALIF the fluorescence signal shifts into several emission states with a total rate of $A = \sum_k A_{2k}$ the sum of all the transitions to levels lower than E_2 for which spontaneous emission is permitted. In this case it is simply represented by a transition between the E_2 and E_3 states.

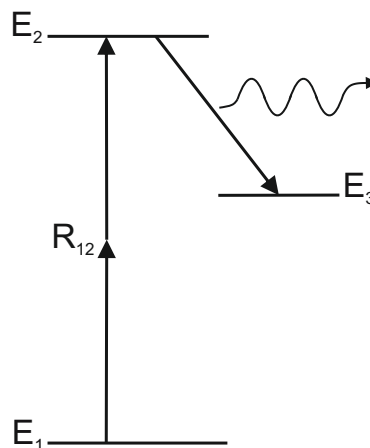


Figure 3.11: Processes in TALIF start with two photon absorption from the ground state (E_1) into (E_2) followed by the various de-excitation processes (radiative decay and quenching).

The process of moving an atom from the E_1 to E_2 state requires it to absorb two

photons simultaneously, this allows it to move from a virtual state with only one photon absorbed to a higher E_2 state. For both the calibrated and actual measurements the laser system needs to have the same power dependence in order to produce an unsaturated two photon excitation. The ground state density is described by equation 3.10 where the negative rate and density is due to the subsequent population of the upper excited state E_2 , however there is little change to the ground state density due to the low laser energy used for the excitation, so we can assume $n_1(t) \approx n_0$.

$$\frac{d}{dt}n_1(t) = -R(t)n_1(t) \quad (3.10)$$

The ground state density will influence the overall density of the higher excited state E_2 which will also be affected by depopulation through a number of processes, this can be seen in equation 3.11, where the density from equation 3.10 is present, followed by the depopulation processes where $A = (A_2 + Q_2)$, such that A is the fluorescence rate from the E_2 state and Q the quenching rate of the upper state.

$$\frac{d}{dt}n_2(t) = R(t)n_1(t) - An_2(t) \quad (3.11)$$

Equation 3.11 also shows that the ground state density is proportional to the excited state population. This is governed through the rate equation 3.12 which is referred to as; the generalised two-photon excitation rate which governs the number of electrons per second that get excited from the E_1 to E_2 state. This is expressed in terms of the excitation cross section ($\sigma^{(2)}$) [58] and the square of the laser energy.

$$R(t) = G^{(2)}\sigma^{(2)}g(\nu)\left(\frac{I_0(t)}{h\nu}\right)^2 \quad (3.12)$$

It includes the photon statistic factor $G^{(2)}$ which takes into account the varying phase within the laser field and the factor 2 probability of absorbing two photons [61,62]. The two photon cross section ($\sigma^{(2)}$) differs from a typical LIF set up as it requires greater laser intensities due to a smaller cross section. The normalised line profile $g(\nu)$ is made up of the effective laser line profile as well as pressure and Doppler broadened atomic absorption line. The last part of the equation represents the photon flux, with the laser intensity I_0

divided by the photon $h\nu$, this is all squared due to the two photon component.

To measure the level of fluorescence from the excited state E_2 the total radiative decay is considered with the effective excited state loss including quenching ($A_2 + Q$), collisional quenching (Q) acts to reduce the lifetime of the upper state by increasing the number of loss channels.

The laser energy is calibrated and measurements are taken below the saturation threshold, this ensures that no laser saturation is observed, hereby limiting processes like photo-dissociation [63,64], photo-ionisation [65] and amplified stimulated emission which would further impact the effective excited state loss.

With minimal ionisation, the decay from the upper state E_2 is written as ($A_2 + Q$). If E_2 is no longer being filled, the recorded signal will be an exponential decay with the lifetime $\tau = 1/A$. Where the ICCD camera with a specific filter will record the selected wavelength $h\nu = E_2 - E_3$

By rearranging equation 3.11, the number of fluorescent photons (n_F) of the excited state E_2 can be expressed as equation 3.13. The optical branching ratio for the transition $a_{23} = \frac{A_{23}}{A}$ where $A = A_2 + Q$ looks at the fluorescence channel from the upper excited state E_2 . It considers both the effective decay rate A and also the radiative decay A_{23} of the state.

$$\begin{aligned} n_F &= A_{23} \int_0^\infty n_2(t) dt \\ &\dots \\ n_F &= n_1 a_{23} \frac{\sigma^{(2)}}{(h\nu)^2} G^{(2)} g(\nu) \int_0^\infty I_0^2(t) dt \end{aligned} \tag{3.13}$$

Lastly, to express the fluorescence signal in terms of the ground state density and laser system efficiency. Equation 3.14 is the detected signal S , where the total number of fluorescence photons measured at a specific wavelength n_F is dependent on the solid angle $\Delta\Omega$ with only the photons falling into this angle being detected. There will also be detector sensitivity at this wavelength η and the probability of transmission through all the experimental optics at the chosen wavelength T to consider.

$$S = \eta T \frac{\Delta\Omega}{4\pi} n_F \tag{3.14}$$

From the equation 3.13, the integral is performed through space and time between the limits of 0 and ∞ and included in the equation 3.14.

$$S = \eta T \frac{\Delta\Omega}{4\pi} a_{23} G^{(2)} g(\nu) \sigma^{(2)} n_1 \left(\frac{E}{h\nu} \right)^2 \quad (3.15)$$

A number of key variables are still required before a density can be calculated, such as the time and space characteristics of the laser intensity profile, the two-photon excitation cross section which need to be taken from literature.

3.3.3 Calibration

To combat the lack of known data needed to provide the ground state density using the fluorescence signal, one calibration technique has been formulated which uses a second noble gas introduced into the GEC system and held under the same operating pressure as the primary gas. The reference gas is matched to the primary gas by determining whether it has a two photon resonance close to the species it is absolutely calibrating [2, 66]. In this case xenon is used to calibrate atomic oxygen as the laser excitation is spectrally similar at 224 nm and 225 nm respectively. For calibration of atomic hydrogen, krypton is used as it has similar laser excitation at 205 nm and 204 nm. The laser temporal and spatial shape is maintained for the calibration to be accurate as well as retaining the same spectral properties of the laser. This procedure is repeated for hydrogen and krypton. Other established calibration methods use flow-tube reactors, where a particle source generates a stationary gas flux of radicals and a reactor is able to measure these via gas-phase titration [67], however this configuration wouldn't be suitable for the GEC cell.

The atomic oxygen ground state density (n_O) is calculated using the reference gas density of xenon via equation 3.16, where the laser light at 225.64 nm excites O atoms from a ground state into the O(3P³P) and measuring the TALIF radiation with a 844 nm filter. A similar measurement is performed using xenon and excited at 224.29 nm into the Xe(6P'[3/2]₂) and emission is captured at 834 nm, for the purposes of this work these excitation and fluorescence wavelengths are similar as shown in figure 3.12. Xenon density is calculated via a pressure measurement, while the O atom density is calculated using

equation 3.16. The values for the transmission and detection sensitivities are calculated prior to taking the measurements.

$$n_O = \frac{\eta_{Xe} a_{23Xe} T_{Xe} \sigma_{Xe}^2}{\eta_O a_{23O} T_O \sigma_O^2} \left(\frac{E_O}{E_{Xe}} \right)^2 \frac{S_O}{S_{Xe}} n_{Xe} = \chi \frac{S_O}{S_{Xe}} n_{Xe} \quad (3.16)$$

The fluorescence signal of oxygen S_O and reference gas xenon S_{Xe} are measured, with the reference gas density of xenon calculated during the calibration phase. Here, the detection sensitivity η and optical transmission T are obtained experimentally or taken from literature. A ratio of the excitation cross sections σ_{Xe}^2/σ_O^2 is taken from literature, as the ratio of the individual values are not known, this has been estimated with a precision of 50% [2]. The laser configuration is identical for both measurements, so only an energy meter is required to measure the stable laser energy, the ratio is given as E_O/E_{Xe} .

A similar procedure has been used for the H TALIF, however different filters are required to observe the hydrogen fluorescence at 656 nm and krypton fluorescence at 826 nm where the excitation wavelengths are 205.08 and 204.13 nm for hydrogen and krypton respectively.

The excitation schemes for O₂/Xe and H/Kr are displayed in figures 3.12 and 3.13, these are taken from the work of Niemi et al [2, 60] and show the fluorescence channel between the upper and lower excited states with the associated excitation wavelength. Xenon and Krypton are chosen as calibrating gases due to the two-photon resonance being as spectrally similar as possible to the gas of interest (Oxygen or Hydrogen).

3.3.4 TALIF experimental technique

With the low pressure plasma environment and stabilised optical configuration, the laser system used in this work is a Continuum Surelite SL-EX series, high energy Nd:YAG laser. The laser beam is positioned into a Continuum Horizon optical parametric oscillator, with a wavelength operating range of 192 - 2750 nm. The system has a pulse width range of 3-5 ns and is pulsed at a frequency of 10 Hz. The laser beam is focussed onto a region of interest between the two GEC electrodes via a lens. The laser path and associated optics are shown in figure 3.14, the laser pulse for the specific wavelength is created and passes onto a variable attenuator this manages the laser pulse energy as set at the CPU. It is

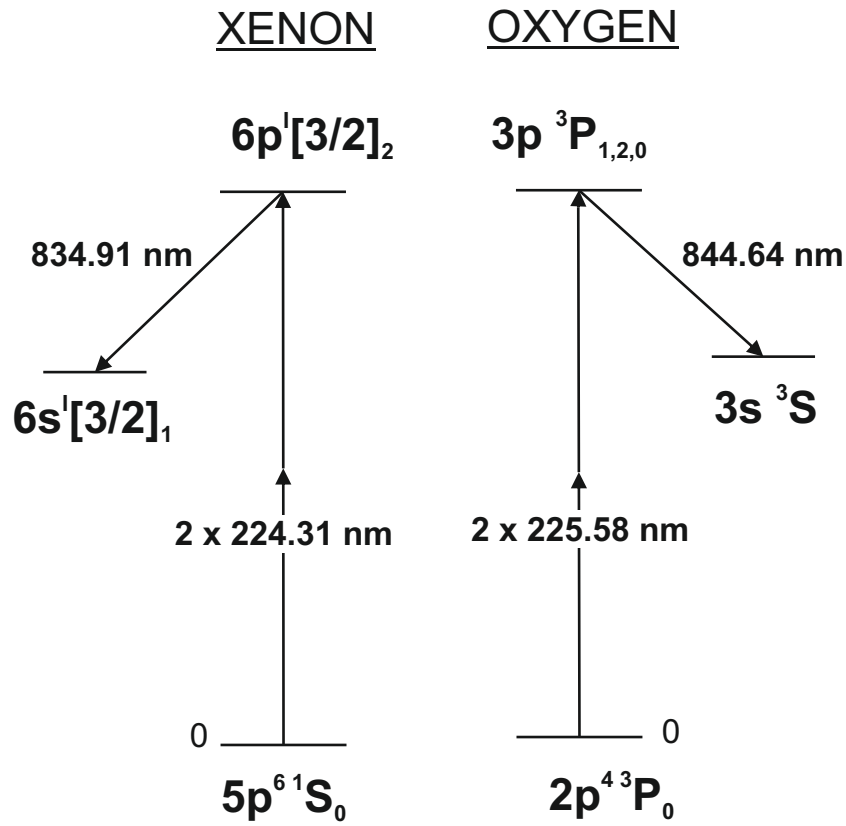


Figure 3.12: Oxygen and xenon TALIF schemes

determined by the angle of the attenuator, which is coated in an anti-reflective material and allows a proportion of laser light through. It is aligned to the second window which is referred to as the compensator, these are both angled using a Zaber T-NM17A04 stepper motor. The outputted energy is monitored by a high speed photodetector Thorlabs DET 10A/M which absorbs 10% of the reflected laser beam, this monitors and corrects for any deviation in laser energy via a PID loop which displays the pulse voltage on an oscilloscope (LeCroy WaveSurfer 104MXs-B 1 GHz 10 GS/s) and loops the value back into the attenuator to make any adjustments. Calibration of the photodetector is done using a Gentec QE25LP-S-MB by placing it in front of the variable attenuator and recording the values into the CPU, it is also placed in front of the beam dump to measure the final laser energy.

The following mirrors control the beam path and guide it through the focussing lens and into the beam dump at the exit of the GEC cell. The beam is focussed across the entire electrode surface, which allows for spatially resolved measurements to be obtained. The

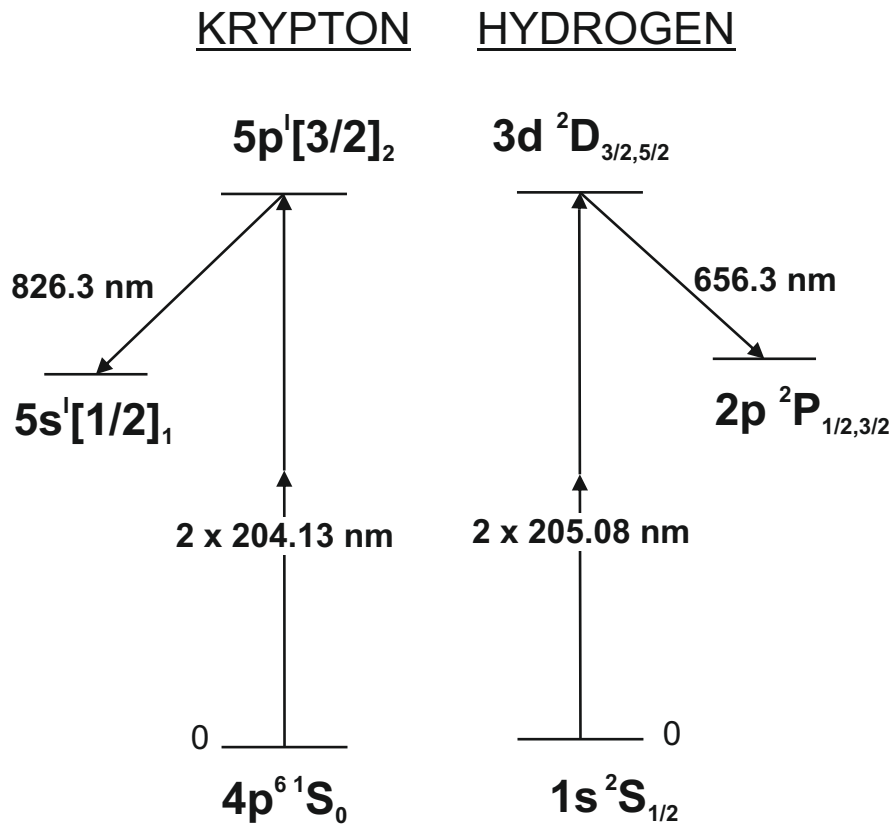


Figure 3.13: Hydrogen and krypton TALIF schemes

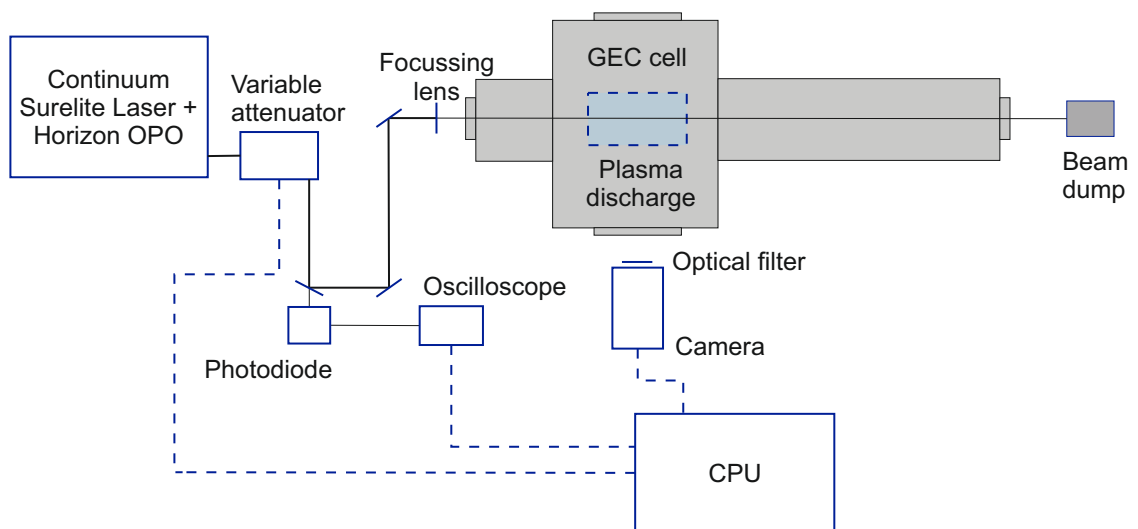


Figure 3.14: Experimental schematic based on the GEC cell including laser set-up and ICCD configuration

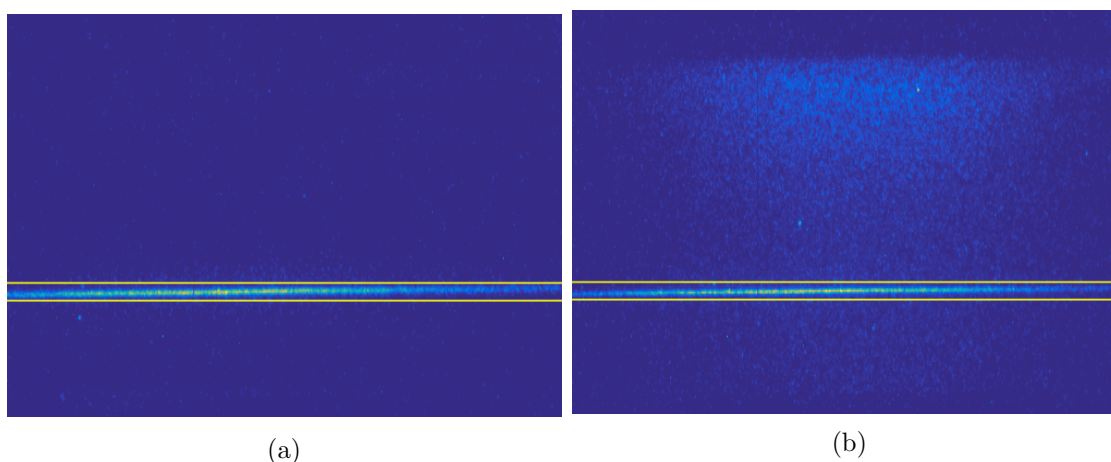


Figure 3.15: TALIF calibration and measurement in the GEC reference cell. Xenon calibration measurement at 20 Pa with a laser energy of $100 \mu\text{J}$ (a) and 20 Pa oxygen/argon plasma operated at 200 W and $800 \mu\text{J}$ laser energy (b)

output trigger of the laser system is set at 10 Hz and keeps the ICCD camera synced. ICCD camera is pointed at the whole discharge region and is used to measure the fluorescence signal and its decay in time.

To obtain absolute density measurements, equation 3.16 uses the spectrally integrated fluorescence signal taken at 844 nm for atomic oxygen and 835 nm for xenon at a bandwidth of approximately 10 nm. The measurements have a spatial element to capture the whole discharge region and temporal integration to observe adequate fluorescence signal.

Figure 3.15 illustrates the shared region of interest (ROI) yellow box which calculates a spatially integrated signal for the enclosed region. The laser beam was positioned 4.4 mm from the lower electrode surface, this coincided with the lowest possible beam position as it entered the GEC cell. The same ROI is used throughout the TALIF measurements to preserve the spatio-temporal characteristics of the laser pulse interaction. As previously mentioned the vertical PROES image size is 49 mm which can be divided by the number of pixels in the vertical axis (1024), to obtain a pixel to real size calibration. The fixed yellow box size is 1024×40 which equates to a yellow box width of $191 \mu\text{m}$ and approximate beam width of $96 \mu\text{m}$.

Figure 3.16 shows the quadratic dependence of the laser energy on the square root of the TALIF signal which eventually saturates via photo-ionisation as the laser energy is increased. This measurement is used to determine the highest laser energy possible

without any saturation influences. The final two points show a deviation from the line of best fit and indicate the point at which the discussed influences occur.

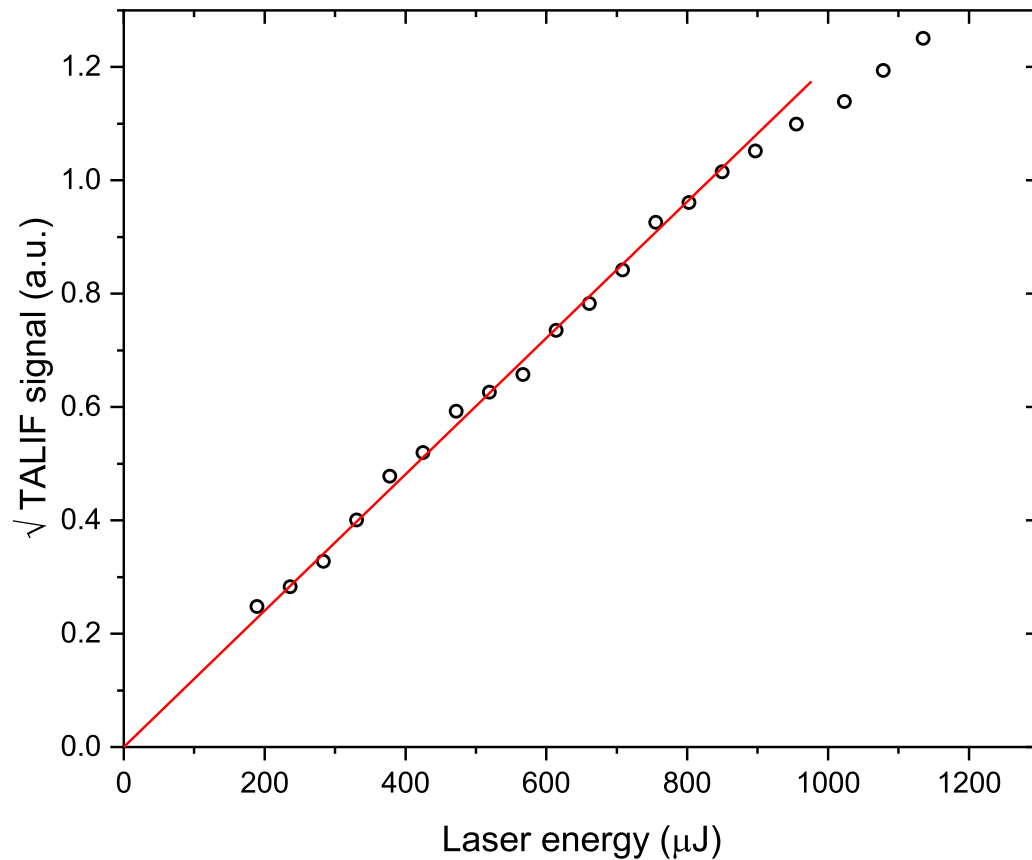


Figure 3.16: Sample oxygen TALIF signal, by increasing the laser energy it highlights the point at which the TALIF signal saturates and no longer exhibits a linear response. Here, a linear response is observed up to 800 μJ . The plasma was operated at 50 W at a pressure of 10 Pa and gas mixture of O_2/Ar (98%/2%).

This is repeated for the hydrogen TALIF with a slightly reduced laser energy, but the same principle to deduce the point of saturation. This occurs around 780 μJ therefore a lower laser energy of 700 μJ was used to ensure no saturation processes would influence the TALIF signal.

Chapter 4

Low temperature plasma modelling

There are number of different ways to characterise low temperature, low pressure plasmas, one is through simulation of the operational environment. This allows for a reference to be made with experimental data. In this work a modular, fluid-kinetic code is used to simulate the GEC cell with a range of operational parameters. Many factors control the gas phase chemistry during operations, this includes the pressure, gas mixture, driving frequency and plasma operation pulsed or continuous, it is a highly complex system to monitor and characterise [68]. These systems can be modelled using one, or a combination of approaches, this work uses a hybrid modelling approach [69]. Key considerations of plasma modelling tools must include the ability to address a whole plasma system such as is used in industry while also dealing with some finely detailed plasma phenomena such as the region of interest above the grounded electrode. The hybrid model approach splits the various physical processes into separate models all of which are on different timescales, the key is to combine them iteratively. This approach allows for a selection in the relevant modules so only conditions that are of interest will be computed. The hybrid modelling (HM) approach will be used to compare experimental data with a pressure range of 1-250 Pa while operated between E and H modes, via the coil in the upper electrode as shown in figure 3.1. The hybrid plasma equipment model (HPeM) is a 2D modular plasma simulation code which has been designed to investigate reaction pathways within a

low temperature, low pressure environment and is capable of simulating a range of reactor geometries. It can analyse different gas chemistries and generate the corresponding plasma parameters. HPEM is made up of a series of modules, the main one is the Electromagnetic Module (EMM) in which the inductively coupled electric fields are calculated, followed by the Fluid kinetics - Poisson module (FKPM) which calculates species densities. These are cycled through and support each other for a predefined number of iterations. The initial input values must also be defined in the model, these include system pressure, ICP power and behaviour of the electrons and ions. These input variables are integral to validating the experimental results which are also compared to TALIF measurements.

4.1 Hybrid plasma equipment model: modules and equations solved

Hybrid modelling combines a mixture of fluid and kinetic approaches that addresses equipment scale plasma processing plasmas. This approach accommodates systems that cannot be fully explained by fluid approaches, but require large computational capacity for a pure particle approach. The plasma modelling described in this research is a two-dimensional hybrid plasma equipment model (HPEM) which is widely used for simulating non-equilibrium low pressure plasmas, this has been developed by Kushner and his colleagues, where an in depth description of the model and its scope can be found at [69]. This code was chosen to simulate the environment as it has been well characterised within a low pressure, inductively coupled plasma environment [70–73].

Figure 4.1 depicts the core operating modules of HPEM, where on an iterative cycle runs through a series of user defined modules. The key module as mentioned is the fluid kinetics Poisson's module (FKPM) which calculates the electrons, ions and neutrals densities as well as solving the electric field potential using Poisson's equation. The FKPM also calculates the momentum, continuity, and energy equations for the heavy particle species. Charged and neutral particle densities are calculated from the continuity equation:

$$\frac{\partial n_i}{\partial t} = -\nabla \cdot \vec{\phi}_i + S_i \quad (4.1)$$

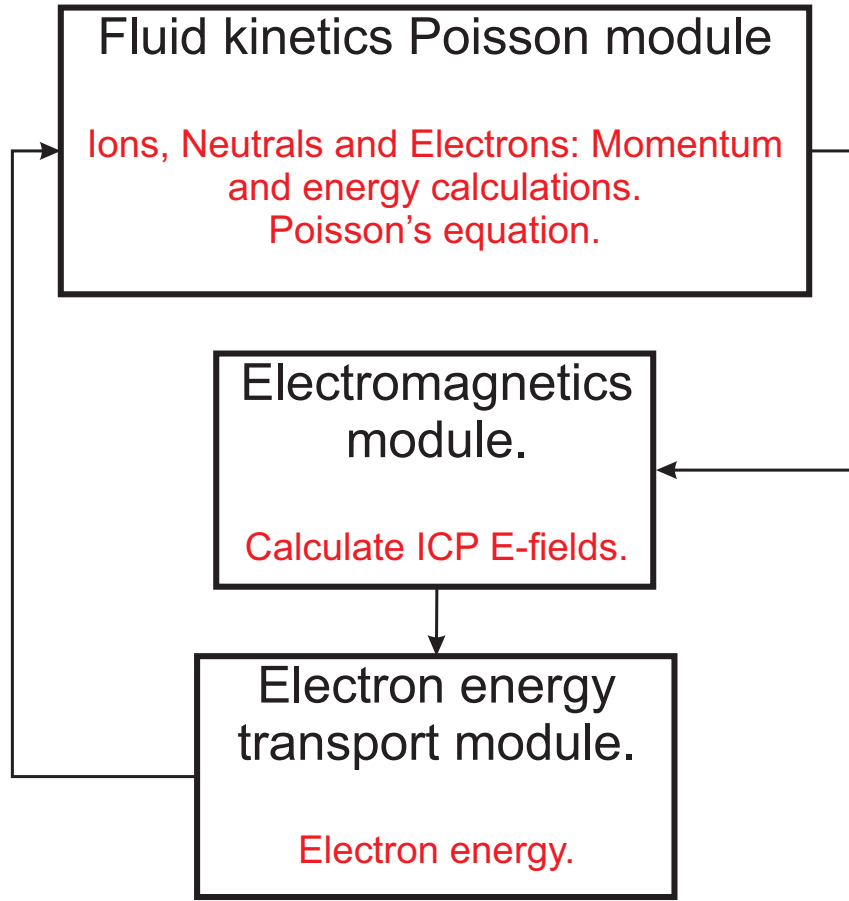


Figure 4.1: List of HPEM modules with the complete life-cycle achieved in one iteration

Equation 4.1 refers to the continuity equation that describes mass conservation, where N_i is the species density, $\vec{\phi}_i$ is the flux and S_i is the source of species i .

For this work, a drift diffusion Scharfetter-Gummel solver was used to compute the electron fluxes, which provided the most stable numerical solution for the simulations. The influence of the flux on the electric field is non-linear [69, 74].

The ion momentum equation is taken in the following form:

$$\frac{\partial \vec{\phi}_i}{\partial t} = -\frac{1}{m_i} \nabla(n_i k_B T_i) - \nabla \cdot (n_i \vec{v}_i \vec{v}_i) + \frac{q_i}{m_i} n_i \vec{E} - \sum_j \frac{m_j}{m_i + m_j} n_i n_j (\vec{v}_i - \vec{v}_j) \nu_{ij} + S_{m,i} \quad (4.2)$$

Here m_i, n_i, k_B, T_i , is the mass, density, Boltzmann's constant and temperature while \vec{v}_i is velocity and ν_{nj} is the collision frequency for the two species (i, j) . The momentum

equation for neutral species takes a slightly reworked form which doesn't include any terms dependent on charge.

$$\begin{aligned} \frac{\partial \vec{\phi}_n}{\partial t} &= -\frac{1}{m_n} \nabla(n_n k_B T_n) - \nabla \cdot (n_n \bar{v}_n \bar{v}_n) \\ &- \sum_j \frac{m_j}{m_n + m_j} n_n n_j (\bar{v}_n - \bar{v}_j) \nu_{nj} + S_{m,n} \end{aligned} \quad (4.3)$$

Both equations consider the fluid velocity with any spatial variations included in the momentum $\nabla \cdot (n_i \bar{v}_i \bar{v}_i)$ term. S_m term in the FKPM module which accounts for the momentum transfer and collisions with other plasma species, in the case that it may change their final state by creating or destroying the species.

The energy equation for charged and neutral species is written as:

$$\begin{aligned} \frac{\partial(n_i c_i T_i)}{\partial t} &= \nabla \cdot \kappa_i \nabla T_i \quad (1) - p_i \nabla \cdot \bar{v}_i \quad (2) - \nabla \cdot (n_i \bar{v}_i \epsilon_i) \quad (3) \\ &\quad + \frac{n_i q_i^2 \nu_i}{m_i (\nu_i^2 + \omega^2)} E_\Theta^2 \quad (4) + \frac{n_i q_i^2}{m_i \nu_i} E_s^2 \quad (5) \\ &\quad + \sum_j 3 \frac{m_{ij}}{m_i + m_j} n_i n_j k_{ij} k_B (T_j - T_i) \quad (6) \\ &\quad \pm \sum_j 3 n_i n_j k_{ij} k_B T_j \quad (7) \end{aligned} \quad (4.4)$$

The heat capacity of the respective fluid is represented by c_i and $\epsilon_i = c_i T_i$. Here p_i is the partial pressure and the thermal conductivity is κ_i . The rate coefficient for the creation of species via heavy particle collisions is k_{ij} and the $\nu_{m,i}$. The terms right of the equals sign in equation 4.4 represent conduction, compressive heating and convection, these are labelled terms one, two and three respectively.

The heating contributions from both electrostatic and electromagnetic fields influence the charged particles. Term four includes a heating contribution in the azimuthal direction by the electric fields created in an inductive coil. The fifth term in the equation is also the heating of ions in an electric field, whereas the sixth and seventh terms are the heating components from elastic and inelastic collisions.

Treatment of the charged and neutral particle transport in the FKPM is finalised by

solution of Poisson's equation which calculates the electric fields in the plasma.

Once the FKPM module has solved for the densities, fluxes and temperatures of the intended species and the electric fields, it passes this information on to the electron energy transport module (EETM) to calculate electron transport coefficient and electron impact source functions. For this work a Monte Carlo simulation of the electrons is used, which calculates the electron energy distribution function (EEDF).

The electron Monte Carlo simulation (eMCS) module accounts for the trajectories of the electrons which are represented in the model by pseudo-particles, released from numerical cells interact with the electric field. The eMCS module has been chosen due to its wide parameter variation in this work, where the lower pressure range (1-250 Pa) can be characterised more accurately using this approach [75]. The electric fields have been taken from the FKPM and EMM modules using a Monte Carlo algorithm [76]. The electron energy distribution function (EEDF) is calculated at each spatial position which is obtained from the Monte Carlo algorithm and its values for the electron transport and electron impact rate coefficients which are implemented into the following FKPM iteration. This cycle is then repeated and continues until a convergence is reached.

The electromagnetic module (EMM) is used to calculate Maxwell's equations for the electromagnetic fields of the inductively coupled plasma coil, which requires a user set coil current that varies to meet the input power.

Once the geometry and chemistry set (discussed below) have been implemented, the simulation is run for several thousand radio frequency cycles until all species and temperatures reach convergence.

4.2 Geometry

The chamber geometry has been modelled on the geometries of the GEC cell, this was accomplished during the integration of the auto matching box and also attachment of the lower electrode voltage probe. The GEC cell was stripped down and the electrode and wall surfaces were measured and a custom mesh geometry was created. The chamber geometry mesh is 120 x 120, where the inter-electrode distance is represented by 43 mesh points. While the lower electrode is 51 mesh points to represent 51 mm from the centre of the

electrode to the edge.

A slight deviation from the experimental configuration was a 4 turn copper coil in the simulation, as the inner coil on the experimental system doesn't complete a full final turn, as shown in figure 2.1. Equally the gas inlet and outlets illustrated on the wall and floor of the chamber are in contrast to the experimental configuration, as the outlet port is split between a four way system based at the bottom of the chamber for uniform pumping. The inlet is incorporated into one of the chambers four diagnostic ports and far enough back from the main electrode region to not disturb the plasma due to low gas flow rates. These differences from the experiment are not expected to have a large effect on the results of the simulation.

Plasma parameters are extracted from the simulation in the region close to the electrode for comparison with TALIF results in chapter 6.

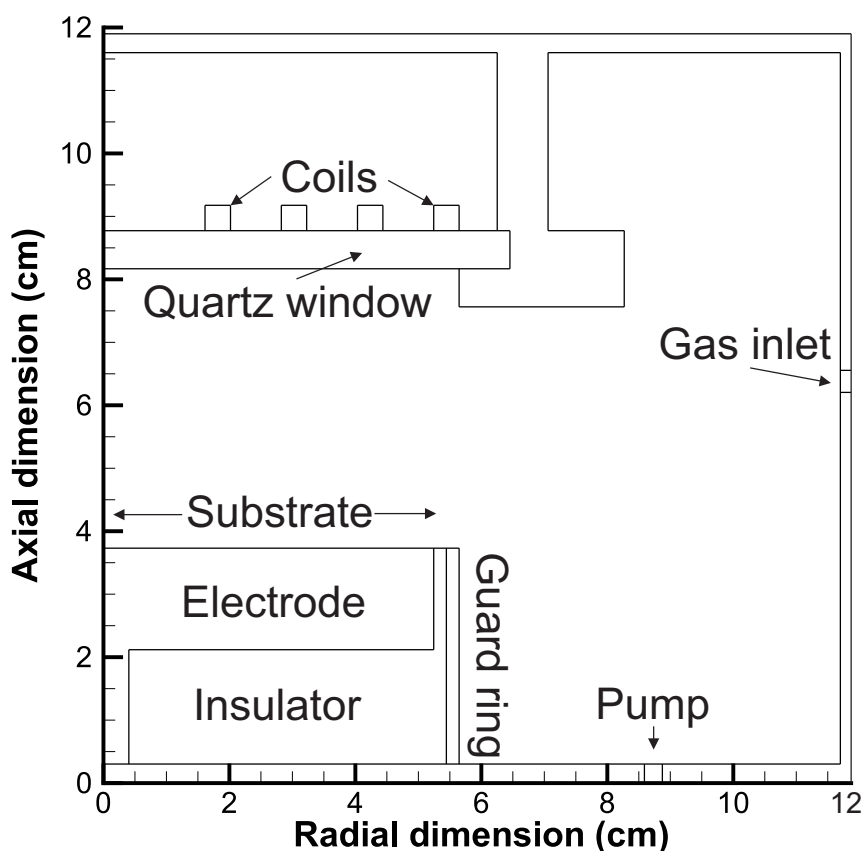


Figure 4.2: Schematic of the plasma geometry used in this work, modelled on the GEC reference cell

4.3 Chemistry

The complete oxygen and argon chemistry set used in this work is included in the table 4.1. The reaction set developed for these simulations is based on the set of reactions and rate coefficients simulated by Rauf et al [77]. Where the key plasma generated species considered are both positive and negative atomic oxygen ions (O^+ , O^- , O_2^+), as well as the atomic oxygen (O) and molecular oxygen in the ground state ($O_2(X^3\Sigma_g^-)$) and metastable states ($O_2(a^1\Delta_g)$, $O_2(b^1\Delta_g)$) and electrons (e). The complete oxygen only set is taken from the published work of Gibson et al [70].

Table 4.1: Complete chemistry set used in these HPEM simulations

No	Reaction	Rate ^{a,b}	Ref.
<i>Argon only reactions</i>			
R1	$Ar + e \rightarrow Ar^* + e$	$f(\epsilon)$	[78]
R2	$Ar + e \rightarrow Ar^+ + e + e$	$f(\epsilon)$	[79]
R3	$Ar^* + e \rightarrow Ar^+ + e + e$	$f(\epsilon)$	[80]
R4	$Ar^* + Ar^* \rightarrow Ar^+ + Ar + e$	5.00×10^{-10}	[81]
R5	$Ar^* + e \rightarrow Ar + e$	$f(\epsilon)$	[77]
R6	$Ar^+ + Ar \rightarrow Ar + Ar^+$	5.66×10^{-10}	[77]
<i>Argon and Oxygen reactions</i>			
R7	$Ar^* + O_2 \rightarrow O + O + Ar$	2.10×10^{-10}	[82]
R8	$Ar^* + O \rightarrow O^* + Ar$	4.10×10^{-11}	[83]
R9	$O^- + Ar^+ \rightarrow O + Ar$	1.00×10^{-07}	[77]
R10	$Ar^+ + O_2 \rightarrow O_2^+ + Ar$	5.10×10^{-11}	[84]
R11	$Ar^+ + O \rightarrow O^+ + Ar$	1.00×10^{-11}	[85]
R12	$O^* + Ar \rightarrow O + Ar$	5.00×10^{-13}	[77]
R13	$O_2^* + Ar \rightarrow O_2 + Ar$	1.00×10^{-19}	[77]
<i>Oxygen only reactions</i>			
R14	$e + O_2(X^3\Sigma_g^-) \rightarrow e + O_2(X^3\Sigma_g^-)$	$f(\epsilon)$	[86]
R15	$e + O_2(a^1\Delta_g) \rightarrow e + O_2(a^1\Delta_g)$	$f(\epsilon)$	[87]
R16	$e + O_2(b^1\Delta_g) \rightarrow e + O_2(b^1\Delta_g)$	$f(\epsilon)$	[87]

Table 4.1: Complete chemistry set used in these HPEM simulations

No	Reaction	Rate ^{a,b}	Ref.
R17	$e + O(^3P) \rightarrow e + O(^3P)$	$f(\epsilon)$	[88]
R18	$e + O(^1D) \rightarrow e + O(^1D)$	$f(\epsilon)$	c
R19	$e + O_2(X^3\Sigma_g^-) \rightarrow e + O_2(a^1\Delta_g)$	$f(\epsilon)$	[86]
R20	$e + O_2(X^3\Sigma_g^-) \rightarrow e + O_2(b^1\Sigma_g^+)$	$f(\epsilon)$	[86]
R21	$e + O_2(a^1\Delta_g) \rightarrow e + O_2(b^1\Sigma_g^+)$	$f(\epsilon)$	[89]
R22	$e + O_2(b^1\Sigma_g^+) \rightarrow O_2(a^1\Delta_g) + e$	$f(\epsilon)$	d
R23	$e + O_2(a^1\Delta_g) \rightarrow O_2(X^3\Sigma_g^-) + e$	$f(\epsilon)$	d
R24	$e + O_2(b^1\Sigma_g^+) \rightarrow O_2(X^3\Sigma_g^-) + e$	$f(\epsilon)$	d
R25	$e + O_2(X^3\Sigma_g^-) \rightarrow O_2^+ e + e$	$f(\epsilon)$	[86]
R26	$e + O_2(a^1\Delta_g) \rightarrow O_2^+ e + e$	$f(\epsilon)$	e
R27	$e + O_2(b^1\Sigma_g^+) \rightarrow O_2^+ e + e$	$f(\epsilon)$	e
R28	$e + O_2(X^3\Sigma_g^-) \rightarrow O(^3P) + O^-$	$f(\epsilon)$	[86]
R29	$e + O_2(a^1\Delta_g) \rightarrow O(^3P) + O^-$	$f(\epsilon)$	[90]
R30	$e + O_2(b^1\Sigma_g^+) \rightarrow O(^3P) + O^-$	$f(\epsilon)$	f
R31	$e + O_2(X^3\Sigma_g^-) \rightarrow O(^3P) + O(^3P) + e$	$f(\epsilon)$	[86]
R32	$e + O_2(a^1\Delta_g) \rightarrow O(^3P) + O(^3P) + e$	$f(\epsilon)$	e
R33	$e + O_2(b^1\Sigma_g^+) \rightarrow O(^3P) + O(^3P) + e$	$f(\epsilon)$	e
R34	$e + O_2(X^3\Sigma_g^-) \rightarrow O(^3P) + O(^1D) + e$	$f(\epsilon)$	[86]
R35	$e + O_2(a^1\Delta_g) \rightarrow O(^3P) + O(^1D) + e$	$f(\epsilon)$	e
R36	$e + O_2(b^1\Sigma_g^+) \rightarrow O(^3P) + O(^1D) + e$	$f(\epsilon)$	e
R37	$e + O(^3P) \rightarrow e + O(^1D)$	$f(\epsilon)$	[52]
R38	$e + O(^1D) \rightarrow e + O(^3P)$	$f(\epsilon)$	e
R39	$e + O(^3P) \rightarrow O^+ + e + e$	$f(\epsilon)$	[52]
R40	$e + O(^1D) \rightarrow O^+ + e + e$	$f(\epsilon)$	e
R41	$e + O^- \rightarrow O(^3P) + e + e$	$f(\epsilon)$	[91]
R42	$e + O_2^+ \rightarrow O(^3P) + O(^3P)$	$3.72 \times 10^{-9} T_e^{-0.7}$	[92, 93]
R43	$e + O_2^+ \rightarrow O(^3P) + O(^1D)$	$7.44 \times 10^{-9} T_e^{-0.7}$	[92, 93]
R44	$e + O_2^+ \rightarrow O(^1D) + O(^1D)$	$7.44 \times 10^{-9} T_e^{-0.7}$	[92, 93]

Table 4.1: Complete chemistry set used in these HPEM simulations

No	Reaction	Rate ^{a,b}	Ref.
R45	$O_2^+ + O^- \rightarrow O_2(X^3\Sigma_g^-) + O(^3P)$	$2.60 \times 10^{-8} T_e^{-0.44}$	[94]
R46	$O_2^+ + O^- \rightarrow O(^3P) + O(^3P) + O(^3P)$	$2.60 \times 10^{-8} T_0^{-0.44}$	[94]
R47	$O^+ + O^- \rightarrow O(^3P) + O(^3P)$	$4.00 \times 10^{-8} T_0^{-0.43}$	[94]
R48	$O(^3P) + O^- \rightarrow O_2(X^3\Sigma_g^-) + e$	$1.50 \times 10^{-10} T_0^{-1.30}$	[95]
R49	$O_2(a^1\Delta_g) + O^- \rightarrow O_2(X^3\Sigma_g^-) + O(^3P) + e$	1.10×10^{-10}	[96]
R50	$O_2(b^1\Sigma_g^+) + O^- \rightarrow O_2(X^3\Sigma_g^-) + O(^3P) + e$	6.90×10^{-10}	[97]
R51	$O^+ + O_2(X^3\Sigma_g^-) \rightarrow O_2^+ + O(^3P)$	2.30×10^{-11}	[98]
R52	$O^+ + O_2(a^1\Delta_g) \rightarrow O_2^+ + O(^3P)$	1.00×10^{-11}	[98]
R53	$O^+ + O_2(b^1\Sigma_g^+) \rightarrow O_2^+ + O(^3P)$	1.00×10^{-11}	g
R54	$O_2^+ + O_2(X^3\Sigma_g^-) \rightarrow O_2(X^3\Sigma_g^-) + O_2^+$	4.00×10^{-10}	[99]
R55	$O_2^+ + O_2(a^1\Delta_g) \rightarrow O_2(X^3\Sigma_g^-) + O_2^+$	2.00×10^{-10}	h
R56	$O_2^+ + O_2(b^1\Sigma_g^+) \rightarrow O_2(X^3\Sigma_g^-) + O_2^+$	2.00×10^{-10}	h
R57	$O(^3P) + O(^1D) \rightarrow O(^3P) + O(^3P)$	8.00×10^{-12}	[100]
R58	$O_2(X^3\Sigma_g^-) + O(^1D) \rightarrow O_2(X^3\Sigma_g^-) + O(^3P)$	$0.32 \times 10^{-11} \exp(67/T_g)$	[101–103]
R59	$O_2(X^3\Sigma_g^-) + O(^1D) \rightarrow O_2(a^1\Delta_g) + O(^3P)$	$0.32 \times 10^{-11} \exp(67/T_g)$	[101–103]
R60	$O_2(X^3\Sigma_g^-) + O(^1D) \rightarrow O_2(b^1\Sigma_g^+) + O(^3P)$	$2.56 \times 10^{-11} \exp(67/T_g)$	[101–103]
R61	$O_2(a^1\Delta_g) + O(^3P) \rightarrow O_2(X^3\Sigma_g^-) + O(^3P)$	2.00×10^{-16}	[104, 105]
R62	$O_2(a^1\Delta_g) + O_2(X^3\Sigma_g^-) \rightarrow O_2(X^3\Sigma_g^-) + O_2(X^3\Sigma_g^-)$	$3.60 \times 10^{-18} \exp(-220/T_g)$	[105]
R63	$O_2(a^1\Delta_g) + O_2(a^1\Delta_g) \rightarrow O_2(X^3\Sigma_g^-) + O_2(b^1\Sigma_g^+)$	$1.81 \times 10^{-18} T_0^{3.8} \exp(700/T_g)$	[106]
R64	$O_2(b^1\Sigma_g^+) + O(^3P) \rightarrow O_2(X^3\Sigma_g^-) + O(^3P)$	8.00×10^{-14}	[105]
R65	$O_2(b^1\Sigma_g^+) + O_2(X^3\Sigma_g^-) \rightarrow O_2(a^1\Delta_g) + O_2(X^3\Sigma_g^-)$	3.90×10^{-17}	[105]

^a Rate coefficient units are in cm^3/s , T_e has units of eV, $T_0 = T_g/300$ where T_g has units of K.

^b $f(\epsilon)$ states that the rate coefficients were obtained from the electron energy distribution function (EEDF) calculated via the electron Monte Carlo simulation module eMCS.

^c Assumed to be the same as $O(^3P)$.

^d Superelastic cross section, which have been calculated from the corresponding excitation process.

^e The cross section has been approximated using scaling of the ground state via excitation threshold of the metastable.

^f $O_2(a^1\Delta_g)$ is scaled and shifted to estimate the cross section for this reaction.

^g This reaction cross section is presumed to be the same as for the $O_2(a^1\Delta_g)$ state.

^h As per the work of [98] an assumed lower rate of collisions of O_2^+ with metastable molecules.

Due to the plasma being operated across a wide parameter variation Gibson et al has investigated the thermal accommodation and atomic species recombination coefficients of the chemistry set 4.1. These are important as they influence the plasma in a number of ways at different input powers and system pressures. The chemistry set presented was tested against the mesh geometry of the GEC, where multiple iterations were run for GEC specific input parameters such as the low and high power and system pressure configurations on the updated GEC cell. This required custom values for reactive and neutral particles to ensure that the investigated species were fully converged for modelling accuracy. With further consideration for the ion and neutral momentum equations to complement the speed at which the model converges.

Chapter 5

Pulse-induced OES: influence on plasma emission and substrate ion energies

This chapter looks at the development of Pulse induced Optical Emission Spectroscopy (PiOES), as a novel diagnostic for imaging regions of low plasma emission around the floating lower electrode. Power and gas mixture variations produce complex technological plasma environments, these directly impact the spatial distribution of the electron and ion densities between the powered and floating electrodes of the GEC. By applying a tailored voltage waveform at the plasma-surface interface of the lower electrode, the manufactured emission can be captured and analysed to understand the behaviour of atomic species densities under different operating conditions.

The PiOES development will be discussed with results and method for the initial and final designs compared. The influence of the pulse on the ion energy distribution function at the lower electrode is also investigated in line with plasma processing conditions.

5.1 Tailored voltage waveform development

The applications outlined in this research are based on requirements from industry partners to monitor reactive neutrals and ions within regions of interest, to better understand how varying plasma conditions can affect the production of reactive species. [107–109]

Tailored voltage waveforms (TVWs) are used for a variety of applications, these include sustaining plasma discharges through pulse type or sawtooth waveforms. This results in a more advanced control of the particle flux and energy distributions by altering the number of harmonics in the waveform [110]. In this work a pulse type waveform will be used to not drive the plasma but create enough induced emission in a defined region of interest to analyse [111, 112].

The requirement is for a pulse waveform to provide sufficient and targeted emission under normal operating conditions but also be minimally invasive to plasma. These are the development steps for the first TVW design, with an aspiration to initially observe the pulse and then with a better understanding of its impact be able to reduce its presence. By looking at the range of possible ion-surface interactions and the typical ion energies; film deposition is operated between 0.1 — 500 eV and etching from 10 — 10k eV, both these processes occupy a large ion energy range however when considering plasma-assisted Atomic Layer Deposition (ALD) this is characterised at ion energies of 10 — 100 eV and ion fluxes of 10^{13} to 10^{15} $\text{cm}^{-2} \text{s}^{-1}$ [113] [114]. Profijt et al examined ion-surface interactions using an Oxford Instruments FlexAL reactor operated with an oxygen plasma at pressures of 0.5 — 25 Pa and powers of 100 — 500 W. Ion energies in this configuration didn't exceed 35 eV, but were shown to be low enough to prevent ion-induced film damage [115, 116], this provides a benchmark for system measurements when a TVW is applied and will be referred back to when measurements on the GEC system are evaluated.

5.1.1 Initial TVW design

The initial stages of the pulse development were focused on detecting pulse emission 0-4 mm above the lower electrode. This focussed on a plasma operating in both E and H mode with powers ranging from 20 - 300 W. The primary measurements were all taken in an Ar/O₂ plasma with the argon percentage admixture ranging from 50 % to 2 %.

The initial TVW electrical configuration was based on a less capable electrical configuration with a 40 MHz arbitrary waveform generator (TTi TGA12104) and broadband amplifier (ifi SCCX100). A TVW was created manually in the wave select and edit function of the waveform generator, this is represented in figure 5.1 where the 3 larger black circles are the configurable part in the arbitrary waveform. Timescales of a waveform span one

complete RF cycle (74 ns), with a 452 kHz repetition rate. The above hardware is synced via the fixed frequency 13.56 MHz RF generator (Advanced Energy Cesar 1310). The TVWs are monitored on an oscilloscope (LeCroy WaveRunner 204MXi-A 2GHz 10GS/s), which is collected via a voltage probe (Lecroy HVP) placed in line with an n-type cable to measure the TVWs losses after the amplifier.

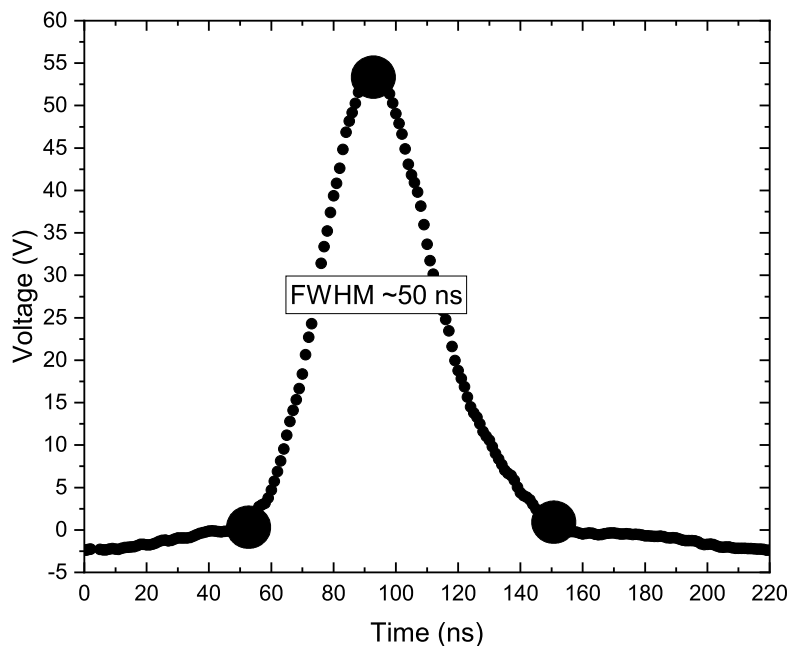


Figure 5.1: Initial pulse shape, with the shortest achievable pulse width (50 ns) at FWHM and voltage varied between 30—70 V, the large black dots represent the points at which the waveform can be manually modified from.

Initial observations on the oscilloscope showed distortions in the cable between the broadband amplifier and lower electrode due to the added voltage probe connection which was impacting the measured pulse shape. To overcome this the original probe was removed from the inline T piece and a new more slimline model (Tektonix P5100A) was mounted against the underside of the lower electrode, this allows measurements of the background plasma voltage to be taken and no longer influence the TVW. This modification also allowed the pulse polarity and phase shift to be more accurately mapped as the voltage probe was measuring at the same surface as the effect was being applied. The phase shift refers to the position of the TVW in the RF cycle (0-360°) relative to the background plasma voltage. The shift accounts for phase changes to the sheath and plasma bulk which will impact a positive or negative pulse.

The initial configuration stages were designed to create and detect a pulse waveform regardless of impact, however to accurately implement a more controllable pulse shape, system modifications were required. These include the purchase of a more advanced waveform generator and automatic matching unit as well as changes to how the pulse is constructed.

5.1.2 Developed TVW design

The updated system hardware was integrated (waveform generator (Keysight 33622A, 120 MHz) and automatic matching box (Advanced Energy, RF Navio)), these were purchased to facilitate the modified pulse design and implementation. The arbitrary waveform generator is capable of ≥ 3 ns pulse rise times and pulse widths of ≥ 8 ns. This allows a greater number of harmonics to be added to the RF frequency (previously 40 MHz limit), in these measurements the largest number of harmonics is 8 ($13.56 \text{ MHz} \times 8 = 108.5 \text{ MHz}$) due to the 120 MHz generator upper limit. The auto matching system creates a stable and matched impedance with zero reflected power, which has been designed to interface with the Advanced Energy fixed frequency 13.56 MHz RF generator.

The waveform generator output is sent to the broadband amplifier as shown in figure 3.1, in the latest TVW design configuration a laptop is connected via USB to the waveform generator to generate and configure the pulse waveforms without having to do some manually. The TVW design script is written in labVIEW and interfaces with the waveform generator to allow user defined pulse amplitudes and harmonics. A voltage probe placed at the underside of the lower electrode measures and displays the voltage waveform applied to the plasma, it also detects the background plasma voltage of the RF waveform produced by the driving frequency and is used as a marker to alter the pulse's phase with respect to the background plasma voltage and polarity during operation.

To generate a TVW at the lower electrode the equation below is used:

$$V_{(t)} = \sum_{k=1}^N V_k \cos(2\pi k f t + \theta_k) \quad (5.1)$$

Equation 5.1 can be tailored to N harmonics by setting the variables; $\theta_k (k = 1, \dots, N)$ as the phase angles and V_k the amplitudes of the individual harmonics, with the fundamental frequency f . These values are derived from equations 5.2 [110, 117].

$$V_k = V_0 \frac{N - k + 1}{N}, \quad V_0 = \frac{2N}{(N + 1)^2} V_{pp} \quad (5.2)$$

The positive pulse waveform is generated by setting θ_k to zero as shown in figure 5.2a while the negative pulse shapes are generated by setting the phase angles of all even harmonics to π as illustrated in figure 5.2b. V_{pp} is the peak to peak voltage.

By varying the number of harmonics a more defined pulse shape can be achieved as shown in figure 5.2, relative to its rise time and width at FWHM. This is based on the number of harmonics specified by the user, beginning with a sine wave at a single harmonic ($N=1$) and increasing the number of harmonics to $N=4$ and $N=8$. This method of creating harmonic specific TVWs allows a much narrower pulse width and shorter rise time over the previous method.

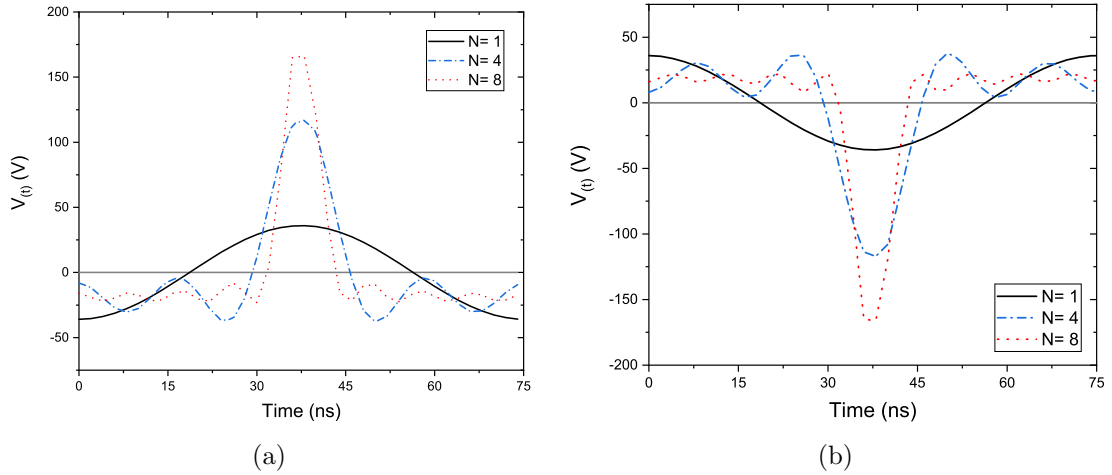


Figure 5.2: Tailored voltage waveforms with a positive (a) and negative (b) polarity. Generated using equation 5.1 with an increasing number of harmonics (1, 4 and 8). The timescales (x-axis) are over one full RF cycle of 74 ns. The peak to peak voltage (V_{pp}) is set according to the pulse shape and experimental configuration.

The phase of the electrical processes is synced to allow PROES images of one or more RF cycles of the ICP driving frequency to be collected, where the pulse shape is included in the first cycle and the next is also documented to capture any subsequent plasma interference the TVW may provoke.

5.1.3 Initial TVW design results

Accuracy and repeatability of the initial pulse design was achieved by using the highest number of configuration points (large black dots in figure 5.1) in one RF cycle to provide the most points that could be manually manipulated, this method achieved a pulse FWHM of 50 ns which was the shortest pulse width and rise time on this setup. The preliminary results focussed on producing a TVW and applying it to an oxygen plasma with sufficient argon to image the fluorescence from the argon $\text{Ar}(2p_1)$ state using a 750 nm filter. This can be observed in figure 5.3, here the emission around the top electrode confirms the plasma is operating in a capacitive mode due to the sheath expansion. The PiOES emission is clearly visible at the surface of the lower electrode, for the results presented here a positive polarity pulse was used. The TVWs were applied to a gas ratio of 1:2 Ar/O₂ and triggered with a repetition rate of 452 kHz (every 30 RF cycles). The plasma had a system pressure of 10 Pa and operated at 50 W, as this produced a stable E mode plasma.

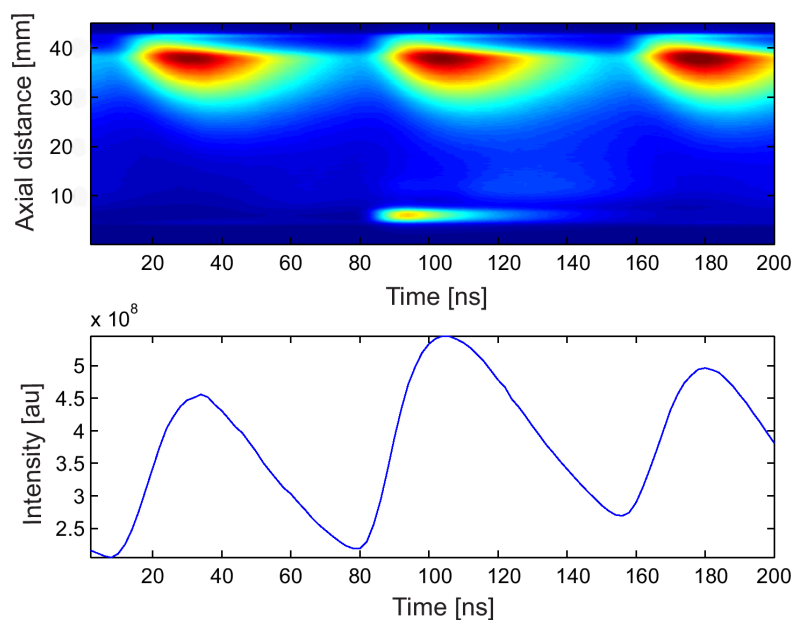


Figure 5.3: This figure illustrates a 70 V positive pulse applied at the lower electrode over multiple RF cycles, the line plot is a spatial integration and shows the additional emission from the pulse during the plasma sustainment mechanisms. These measurements are taken at system pressures of 10 Pa with a 1:2 Ar/O₂ gas ratio operated at 50 W

The spatially integrated intensity plot in figure 5.3 illustrates the influence of the pulse emission feature on the RF cycle it is applied to as well as a small increase on the following

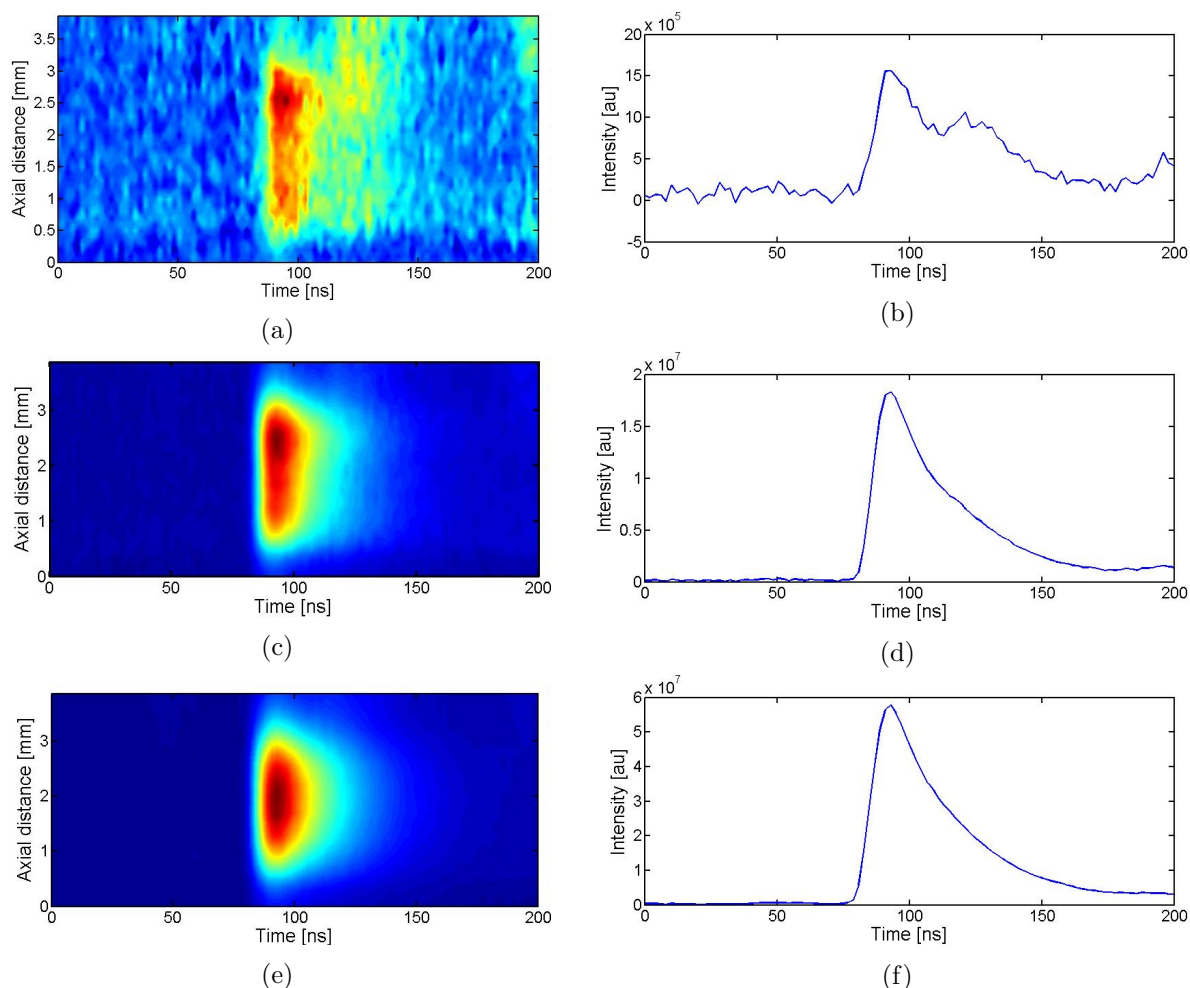


Figure 5.4: Initial PiOES emission measurements, a peak to peak voltage increase of 30, 50 and 70 V_{pp} in figures a,c and e respectively. Spatial integration (0-4 mm) as a function of time (ns) for each of the PiOES images b, d and f. The plasma is operated with a gas ratio of 1:2 Ar/O₂ and a system pressure of 10 Pa at 50 W.

RF cycle. This needs to be minimised, as a large impact on the ion properties will influence the energies outside the acceptable plasma-assisted ALD range.

Figure 5.4 includes PiOES results focussing on a positive pulse voltage increase from 30 V_{pp} in figure 5.4a, 50 V_{pp} in figure 5.4c and 70 V_{pp} in figure 5.4e.

In figure 5.4 the spatio-temporal PiOES images shows a 100 image kinetic series resulting in a temporal timescale of 200 ns (2 ns per image). The spatial axis doesn't include the full inter-electrode distance only 0-4 mm above the lower electrode. PiOES images 5.4a,5.4c and 5.4e with corresponding spatially integrated intensity plots as a function of the TVW region of interest (0-4 mm) and 200 ns timescale. Due to the application of a positive pulse, electrons are accelerated from the bulk plasma towards the lower electrode causing

the excitation which produces observable PiOES emission. Figure 5.4a and intensity plot 5.4b illustrate that for a lower TVW voltage, less PiOES emission will be observed which will impact any further analysis due to the signal-to-noise (SN) ratio. Alternatively with a larger $70 V_{pp}$ pulse voltage as seen in figure 5.4f, more excitation and observed PiOES emission from the $\text{Ar}(2p_1)$ state, results in a larger number of electrons being accelerated and impacting the plasma operationally.

Additional testing to help quantify the TVWs impact on the plasma operation is done by altering the phase at which the TVW is applied within the RF cycle. This is done at the four positions outlined in figure 5.5, a 90 degree spacing is applied between each phase measurement, these will be combined with IEDF measurements at the same positions to compare the electron and ion behaviour.

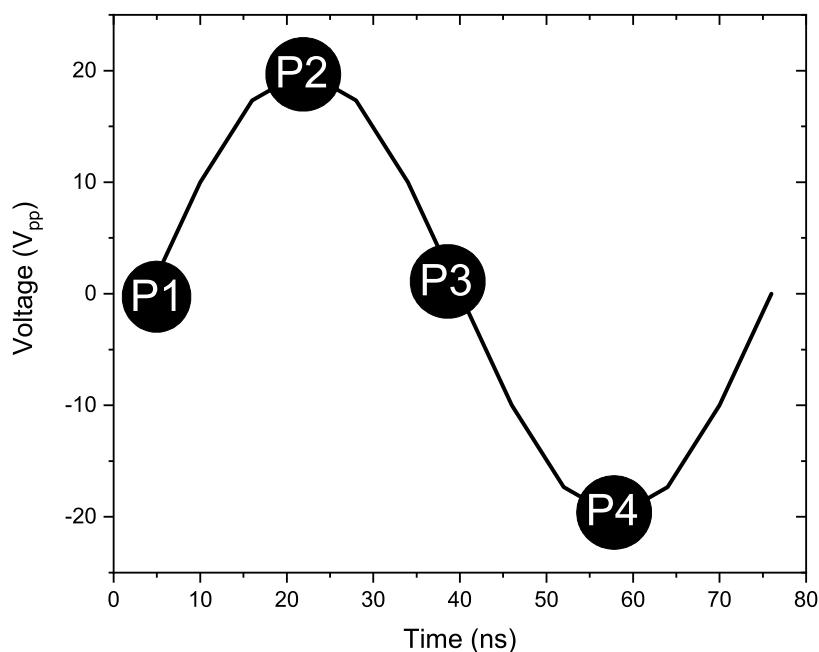


Figure 5.5: The four phase positions assigned to the plasma background voltage waveform detected by the voltage probe and displayed on the oscilloscope, these are spaced 90° apart and are selected prior to the pulse being applied at the lower electrode.

To measure the pulse voltages at the different phase positions (P_1 to P_4), a 70 V pulse was applied to a 50 W O_2/A_2 plasma operating at 13.56 MHz with a system pressure of 10 Pa. The aim to analyse any large fluctuations in ion energies or impact on the ICP operation. An overlay of the individual TVW configuration at the four phase positions illustrates the impact of the initial TVWs width on the adjacent phase positions as shown

in figure 5.6.

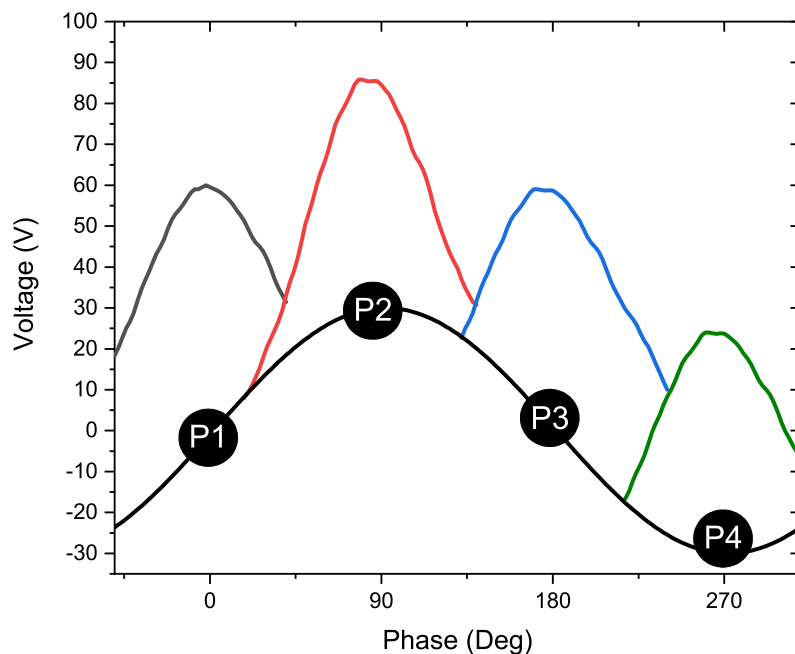


Figure 5.6: Initial TVW design applied to the plasma background voltage at the four phase positions, the plasma needs to be operational before the phase positions are apparent, at which point the phase can be selected and a pulse applied

The voltage probe measurements at the four positions were compared against the generated 70 V TVW, with P1, P2 and P3 producing a combined pulse feature (sine waveform and pulse) of 60 V, while the largest deviation was seen at P4 with an amplitude reduction to 55 V, these were measured individually on the oscilloscope; initially without the plasma ignited to baseline the pulse and then with the plasma on and the phase varied. The pulse is impacted by the phase of the sheath and plasma bulk. At P4 in figure 5.6 the sheath is fully expanded; the sinusoidal voltage is most negative and the electrons are repelled from the electrode, resulting in a reduced electron presence during the pulse application. For P2 in figure 5.6 the sheath is fully contracted and the sinusoidal voltage is the most positive resulting in more electrons at the surface which would contribute to the PiOES emission, when considering a positive polarity pulse.

Figure 5.7 is an investigation into the TVW impact on the ion energies at the plasma-surface interface, these measurements were taken in the same conditions as the PiOES data in figure 5.4. The Impedans RFEA probe was placed on the lower electrode and TVW applied to the same electrode, only positive polarity pulses were investigated in

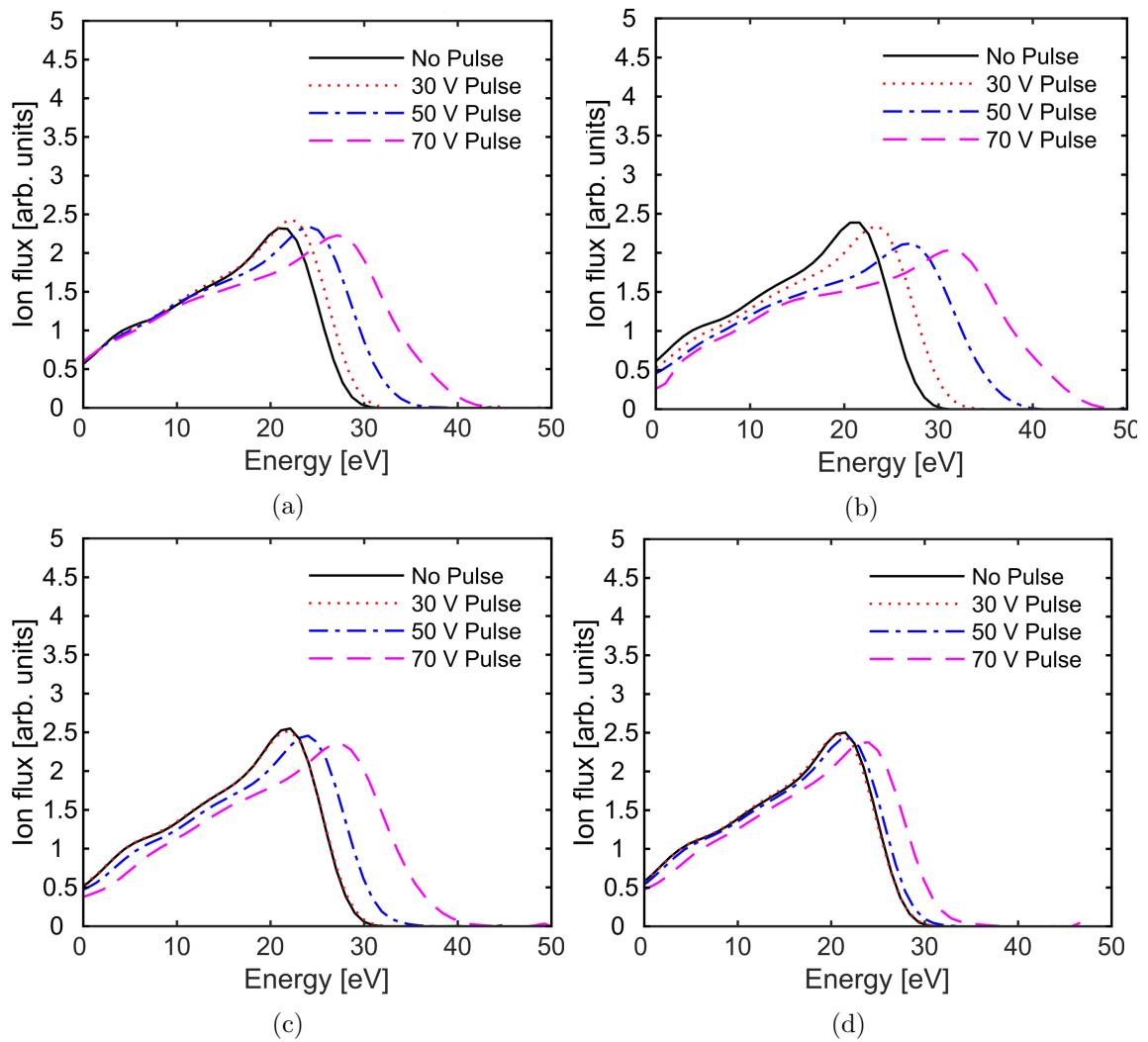


Figure 5.7: IEDF measurements of a positive pulse at the four phase positions P1 (a), P2 (b), P3 (c) and P4 (d) as highlighted in figure 5.5, with a baseline taken using the Impedans RFEA probe and no pulse. An ideal pulse will have minimal deviation from the baseline value across all pulse voltages, the plasma is operated at 50 W in a 1:2 Ar/O₂ gas mixture, with a system pressure of 10 Pa

this dataset. The collector grids were set according to the bias voltage measured using a multimeter and values of approximately 50 V above the dc bias voltage were inputted. As demonstrated in figure 3.3 the current voltage curve allows for the ions at each energy to be measured. The number of user defined scans over this range is set at 10 per measurement. Due to the relatively low pressure (10 Pa) and some collisional effects in the sheath at the floating electrode, the low energy tail at the start of the sweep voltage is due to the effect of collisions. Figures 5.7b and 5.7d have the largest and smallest ion energy variations respectively. The black line, consistent throughout all four different measurements represents the background IEDF measurement without a TVW applied to the system. The same number of RFEA sweeps and scan times are set for each figure, the higher ion energies in figure 5.7a are offset by the larger ion fluxes in figure 5.7c. As previously mentioned the pulse width is the limiting factor in qualitatively determining whether the phase and TVW amplitudes have the desired effect and minimal influence.

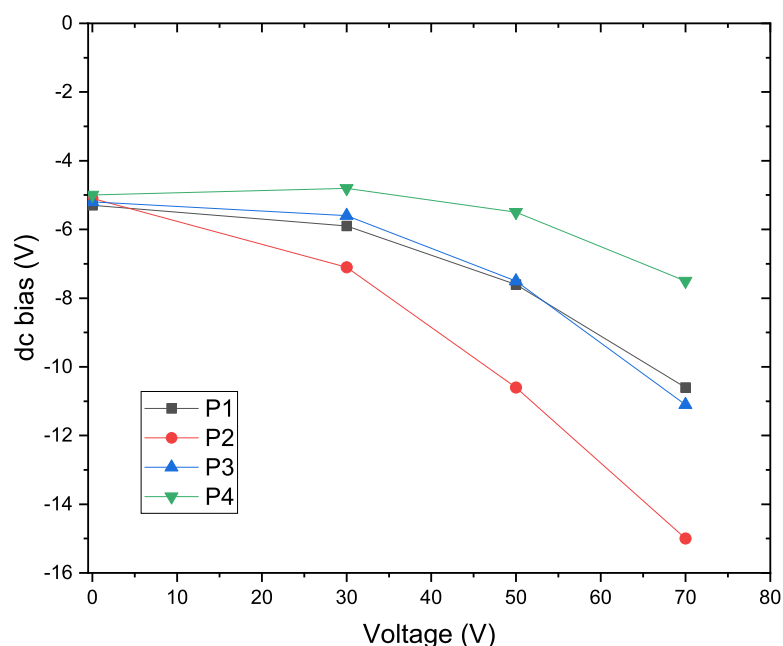


Figure 5.8: DC bias for the pulse voltage variations at the different phase positions as shown in figure 5.7, P2 has the largest ion energy variation ($\sim 20 - 35$ eV) is represented by a more negative DC bias in order to counteract the increase in electrons at the surface.

Figure 5.8 is the dc bias voltage for the IEDFs in figure 5.7, a background reading is taken at 0 V and the subsequent measurements at 30, 50 and 70 V. A positive pulse attracts electrons and repels ions for the short period it is applied for, so a dc bias becomes

more negative to attract positive ions back and even up the ion and electron fluxes on a time averaged basis. These results show that figure 5.7b has a series of larger ion energies at a point in the RF cycle when the sheath is fully contracted resulting in higher electron densities at the electrode surface due to a positive sinusoidal voltage, this requires more highly negative dc biases to counteract this, whereas figure 5.7d has consistently lower energies with a lower electron density as the sinusoidal voltage is negative, therefore requiring less negative dc biases to attract ions to the surface. These results illustrate the impact of a TVW on the ion energies, which are important when considering the sensitivity of plasma assisted ALD processes. As previously mentioned examples of titanium oxide film deposition at 200 W in an oxygen ICP require ion energies of 19 - 27 eV, this would only be possible with pulse voltages of 50 V and below in all but figure 5.7b where the impact on the ion energies is too large [116].

5.1.4 Modified TVW design results

As outlined in section 5.1.2 the modified TVW design and updated waveform generator are capable of generating pulses with narrower widths. For these measurements the plasma was operated in E-mode by applying 50 W into the inductive coil. A TVW consisting of a base frequency of 13.56 MHz with eight consecutive harmonics ($N=8$) and a repetition frequency of 452 kHz (every 30 RF cycles) is used to demonstrate the PiOES concept. The system pressure is 10 Pa and an initial gas ratio of 1:3 Ar/O₂. Example pulse waveforms measured at the bottom electrode under these conditions with different voltages (30 and 70 V_{pp}) and polarities (positive and negative) are shown in figure 5.9. Each pulse is applied with a phase at P4 (reference figure 5.5) where the sheath is fully expanded and the electrons are being repelled from the lower electrode. Figure 5.9a is a negative polarity pulse over several pulse periods, while 5.9b shows zoomed in version of several pulses to better identify the details of the pulse waveform. Under these conditions, the pulse rise/fall times are around 10 ns, with a total width of just over 20 ns. These short pulses should mainly result in electron acceleration, as the heavier ions should not be able to respond to the fast change in the applied voltage.

Figure 5.10 shows the excitation of the O (3p 5P) state (emission at 777 nm) over the full discharge region with two full RF cycles analysed. Figure 5.10 (a) shows a case

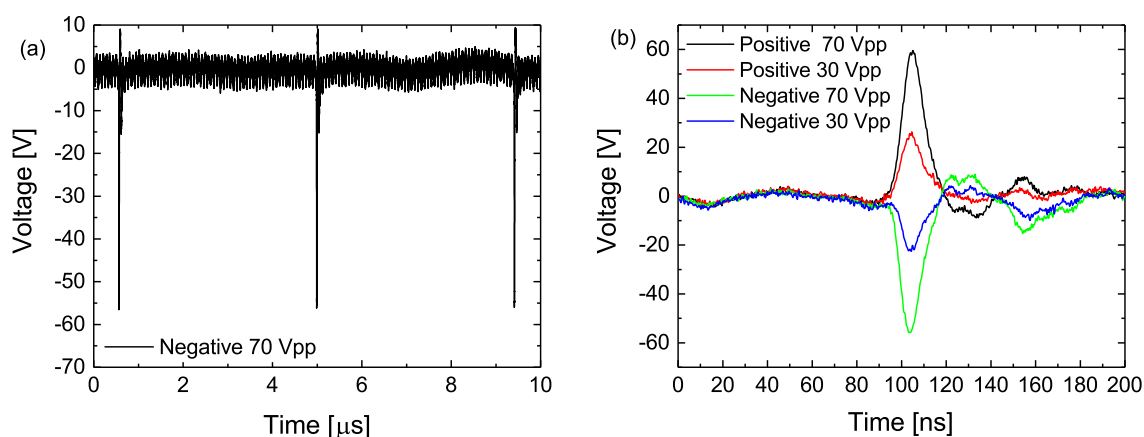


Figure 5.9: Plot (a) is a negative 70 V pulse waveform over multiple RF cycles, while (b) depicts both positive and negative pulses over a shorter timescale, highlighting the reduced pulse width and rise times. The plasma is operated at 50 W with a pressure of 10 Pa and gas mixture of O_2/Ar (98%/2%).

where a 70 V_{pp} positive polarity pulse is applied, while (b) shows the case where a 70 V_{pp} negative polarity pulse is applied. In both cases, the main emission from the plasma is seen just below the coil as a result of sheath expansion, typical to an E-mode ICP. In the positive polarity case, emission resulting from the pulse can be seen close to the bottom electrode (circled). This emission results from excitation due to electrons accelerated towards the electrode from the plasma on application of the positive pulse. In the negative polarity case, a different emission pattern is seen. In this case electrons are accelerated away from the electrode and into the bulk plasma in the direction of the arrow. These electrons influence the sheath expansion emission occurring below the coil, which is seen to be brighter in the cycle following the pulse, compared to the sheath expansion emission occurring around the time the pulse is applied. When comparing figure 5.10 and the initial pulse shape in figure 5.3, it is clear that the modified pulse shape has a much lower emission at the plasma-surface interface despite having the same 70 V pulse voltage, this is due to the faster rise time and more refined pulse width.

Figure 5.11 shows the same data zoomed in to the region closest to the bottom electrode. Here, it is clear that the positive pulse causes more emission in this region compared to the negative polarity pulse. From this we can see that the positive pulse is better for causing emission close to the electrode to carry out PiOES in this region. The negative polarity pulse causes more emission across the entire gap and may be more useful for

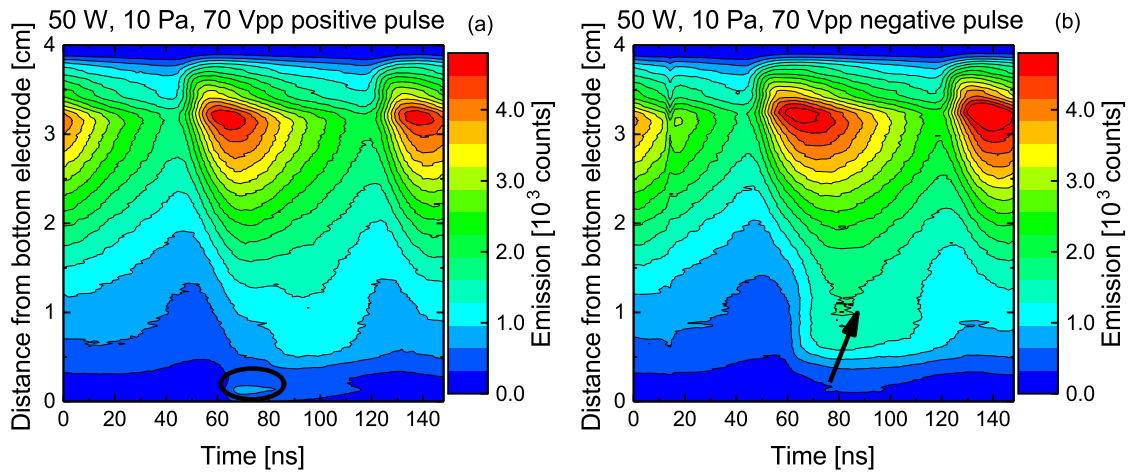


Figure 5.10: Plots (a) is a positive 70 V pulse waveform, while (b) is a negative 70 V pulse with opposite polarity, these plots show the varying impact of the polarity on the bulk of the plasma due to the electron and ion behaviour. The plasma is operated at 50 W with a pressure of 10 Pa and gas mixture of O_2/Ar (98%/2%).

carrying out PiOES across the gap when emission at the plasma centre is weak.

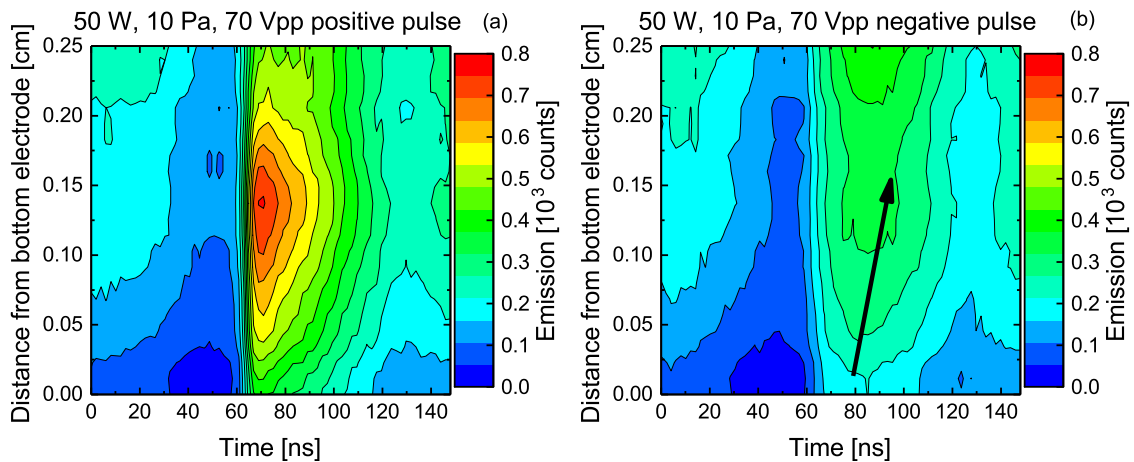


Figure 5.11: PROES measurement of the lower electrode region <25 mm with a 70 V_{pp} positive (a) and negative (b) pulse applied, these are a close up of the same region with the negative pulse emission shifting towards the plasma bulk as the negative pulse repels the electrons at the lower electrode surface. The plasma is operated at 50 W with a pressure of 10 Pa and gas mixture of O_2/Ar (98%/2%).

Figure 5.12 is the same axial region as figure 5.11, but the pulse voltage has been reduced to 30 V. There is little conceivable difference between the two PROES plots at 30 V_{pp} , the pulse is not bright enough to clearly observe under these plasma conditions. The conclusion being that for any future work the pulse voltage under similar conditions will need to be closer to 70 V or more. Where the plasma power is increased, the pulse

voltage will need to scale accordingly.

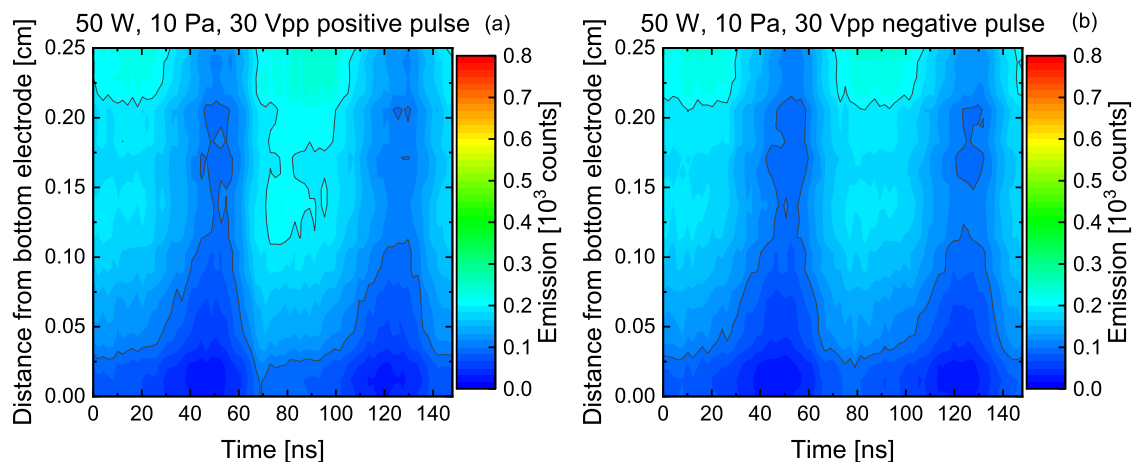


Figure 5.12: PROES measurement of the lower electrode region <25 mm of a $30 V_{pp}$ positive (a) and negative (b) pulse, they show no clear pulse induced emission. The plasma is operated at 50 W with a pressure of 10 Pa and gas mixture of O_2/Ar (98%/2%).

These results show that higher voltages are better, as it produces a more defined image of pulse induced emission. While these results are specific to the test case considered here (10 Pa, 50 W plasma power) the trends with pulse polarity and voltage are expected to be similar for other plasma conditions. Another factor is the pulse needs to minimally invasive in order to preserve the overall operation of the plasma, this is important for industrial processes.

5.2 Pulse influence on ion energy

Having established the primary aim of observing pulse induced emission at the bottom electrode using the modified TVW design, it is important to establish knowledge of other plasma parameters which are influenced by the new pulse. This includes the ion energies and fluxes at the bottom electrode. A Semion retarding field energy analyser (RFEA) was used in this work to determine ion energies at the bottom electrode. The probe is described in section 3.2.1. The DC bias voltages were measured using the probe during plasma operation. The next iteration is to apply a TVW to the GEC system with RFEA in situ to directly measure any fluctuation in either the flux or energy.

Here, the role of the pulse voltage, polarity and repetition frequency are investigated. Figure 5.13 shows ion energy distribution functions comparing (a) positive pulses of varying

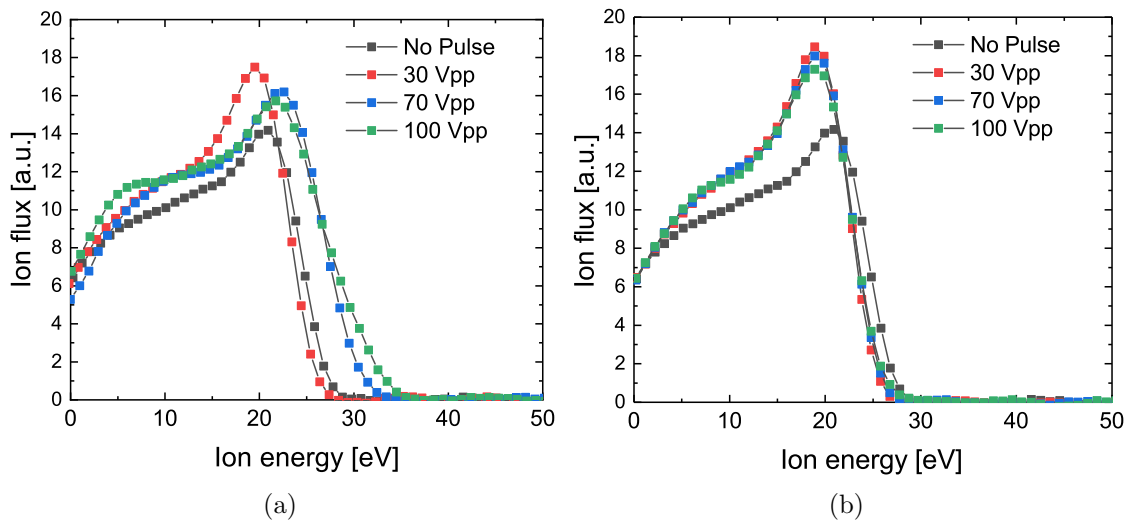


Figure 5.13: These plots illustrate the ion energy and flux for a positive (a) and negative (b) pulse voltage variation, these results show that a positive pulse has a greater influence on ion properties and DC self bias. The plasma is operated at 50 W with a pressure of 10 Pa and gas mixture of O_2/Ar (98%/2%). Pulse voltage is 100 V_{pp}

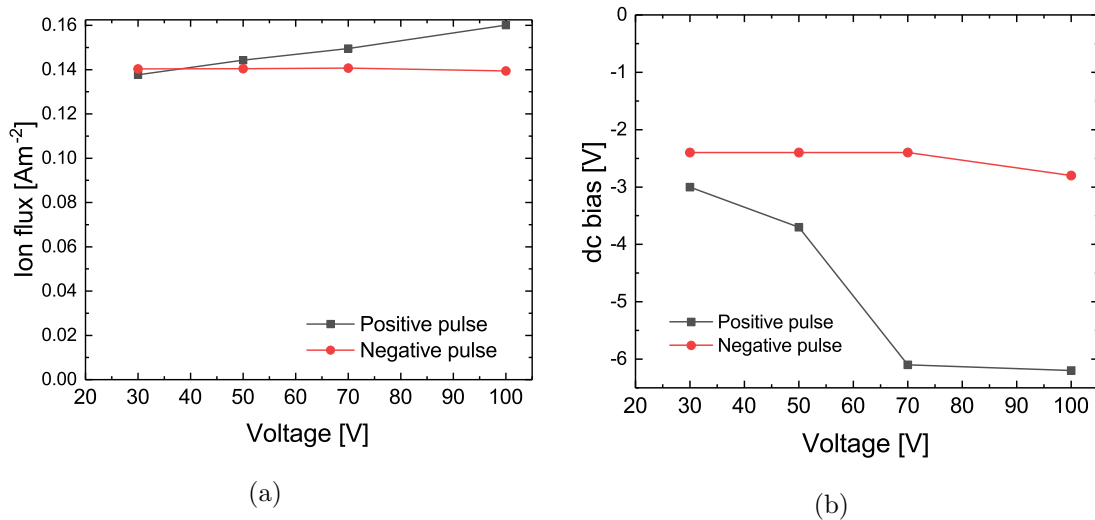


Figure 5.14: Ion flux (a) and DC bias (b) for the IEDF pulse voltage variation. The positive pulse has a larger ion flux variation and more negative DC self bias at the electrode surface. The plasma is operated at 50 W with a pressure of 10 Pa and gas mixture of O_2/Ar (98%/2%), Pulse voltages measured are 30, 50, 70 and 100 V_{pp} .

voltage and (b) negative pulses of varying voltage, with the case where no pulse is applied. For the positive polarity cases the change in the IEDF increases as the voltage is increased, leading to higher ion energies. For the negative polarity cases the IEDFs do not vary much with increasing voltage, but in general show lower ion energies compared to the no pulse case.

Figure 5.14 illustrates the ion flux (a) and dc bias voltage (b) for the IEDFs shown in figure 5.13. From these figures it can be seen that the positive polarity pulse has a generally stronger influence on the ion properties and dc self bias at the electrode. While the ion flux is not largely impacted by the pulse polarity, it can be observed that the positive pulse has a higher ion flux at the 100 V pulse measurement, which coincides with the larger dc bias attracting more ions back to the probe surface. The negative pulse is largely unchanged for both flux and dc bias, which shows a reduced impact on the ion energies and flux. Bias is created to balance electron and ion currents to the electrode. A positive pulse repels positive ions from the electrode for a short time and attracts electrons, therefore the dc bias must become more negative to attract more positive ions to balance the electron and ion fluxes on time average. A negative pulse accelerates positive ions towards the electrode for a short time, and repels electrons, therefore the value of the dc self bias required to balance electron and ion currents to the electrode becomes less negative.

In figure 5.15 the subtraction of the background ion energy distribution function from the varying pulse voltages is plotted in figure 5.13. This data highlights the IEDFs with a greater deviation from the no pulse or background measurement. As previously noted the positive polarity pulse had a more significant ion energy increase with respect to the background measurement, this is shown in figure 5.15a. Figure 5.15b has a largely similar set of pulse measurements and this is mirrored in the overall higher ion fluxes but lower ion energies, this highlights a regime that has a smaller pulse voltage dependence, meaning a lower impact on ion energies and subsequent RF cycles while still maintaining values that would be suitable for ALD processes and stable enough to preserve process uniformity. Unfortunately single measurements occurring at the time of the pulse application cannot be singled out as the RFEA collects its data via the voltage sweep and examines the overall ion energy change not the instantaneous value.

Having considered the polarity and amplitude of the pulse a final consideration is the repetition at which it is applied. As mentioned the pulse is typically confined to a single RF cycle which limits its impact on the following RF cycle, however using the RFEA, ion energy and flux data to represent a scenario that focuses on the average over a 60 second data acquisition period, allowing the time averaged effect of using different repetition frequencies to be shown.

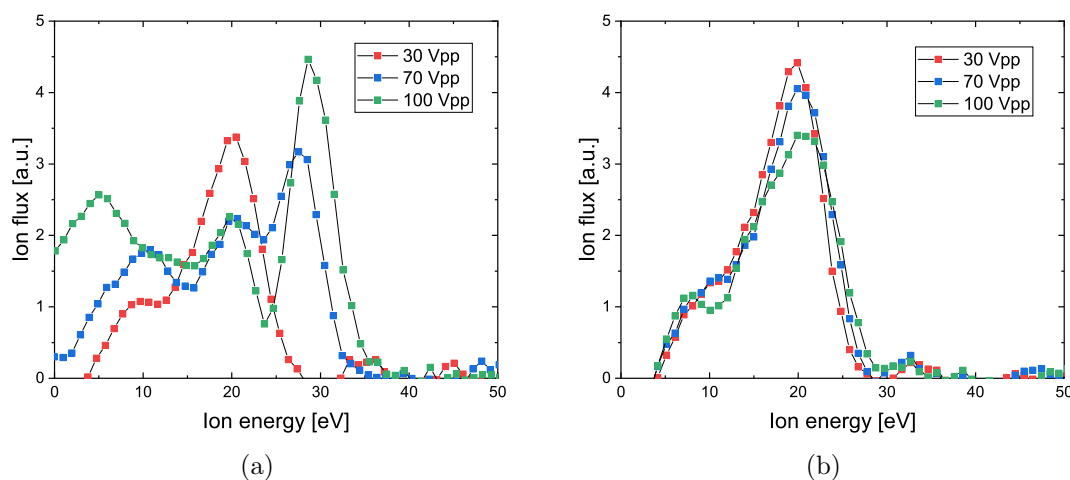


Figure 5.15: Positive (a) and negative (b) pulse voltage variation with the background ion flux subtracted from each pulse voltage plot. Highlighting the baseline change from the background measurement taken for both sets of measurements. The plasma is operated at 50 W with a pressure of 10 Pa and gas mixture of O₂/Ar (98%/2%). Pulse voltage is 100 V_{pp}.

Figure 5.16 examines the ion energy shift at different repetition frequencies between 113 and 452 kHz, for the case of 100 V_{pp} positive polarity pulses, which have been shown to have the greatest effect on the ion properties. The black solid line and symbols represents the plasma background values without any additional inputs. The equipment limitations of the ICCD camera impose an upper limit of 500 kHz, which prompts the 452 kHz rate. 226 and 113 kHz are chosen as lower frequencies which are also multiples of the 13.56 MHz, the driving frequency of the plasma.

The data in figure 5.16 illustrates the importance of control over the pulse's characteristics. There is an increased overall change in the ion energies when presented with the higher repetition rates; with the higher repetition rates leading to higher ion energies in the tail of the distribution function. The ion flux and dc bias for these cases are plotted in figure 5.17. It can be seen that the ion flux increases and the dc bias decreases with increasing repetition frequency, illustrating the stronger effect of the pulse on the plasma.

The phase is investigated in order to compare the changes at the four phase positions in the RF cycle using the developed TVW, in figure 5.18, the negative polarity pulse illustrates lower ion energies with comparable ion fluxes for the four phase positions as outlined in figure 5.5. The negative pulse attracts ions but due to the timescale it is operating on the ions are not influenced, instead electrons are repelled and the dc bias

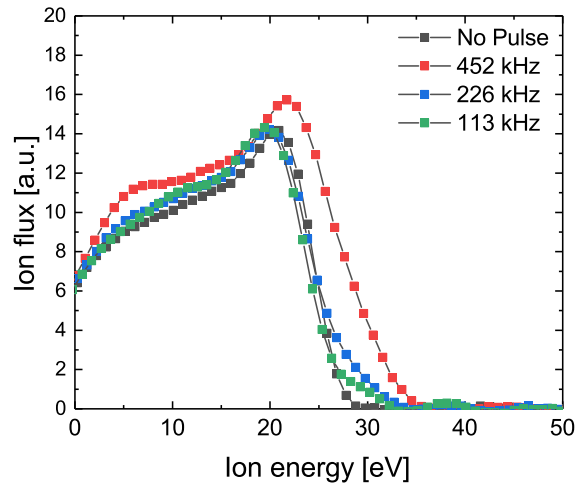


Figure 5.16: Ion energy data taken for different repetition rates 452, 226 and 113 kHz, with identical plasma powers of 50 W and system pressure maintained at 10 Pa, the gas mixture is O_2/Ar (98%/2%). At the highest repetition frequency (452 kHz) the ion flux and energy impact is observed, with a positive pulse voltage of 100 V_{pp} .

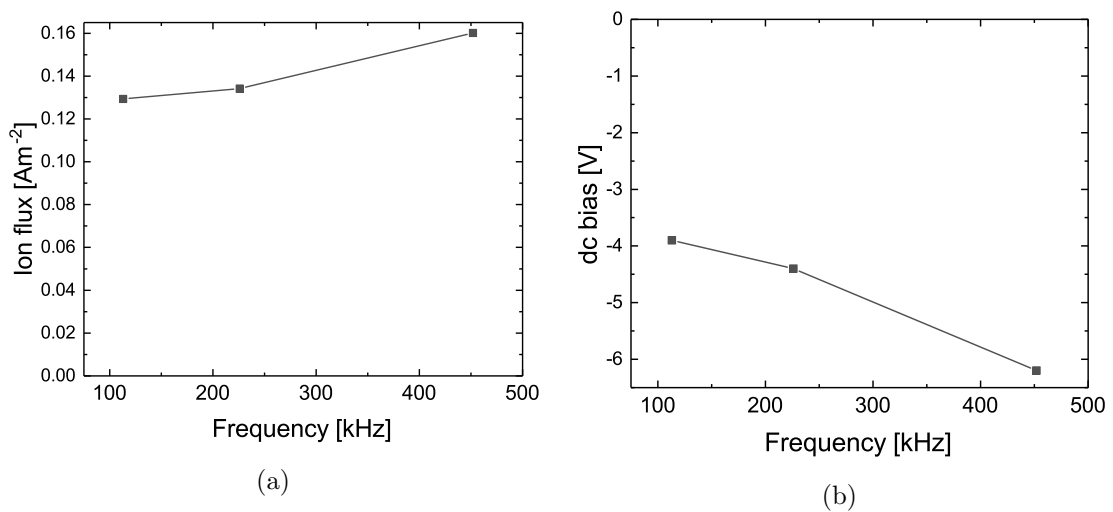


Figure 5.17: Ion flux (a) and DC bias (b) for the IEDF pulse frequency variation, both plots exhibit an increasing trend with increased repetition rates. Highlighting the importance of creating enough induced emission while keeping the repetition frequency low. The plasma is operated at 50 W with a pressure of 10 Pa and gas mixture of O_2/Ar (98%/2%).

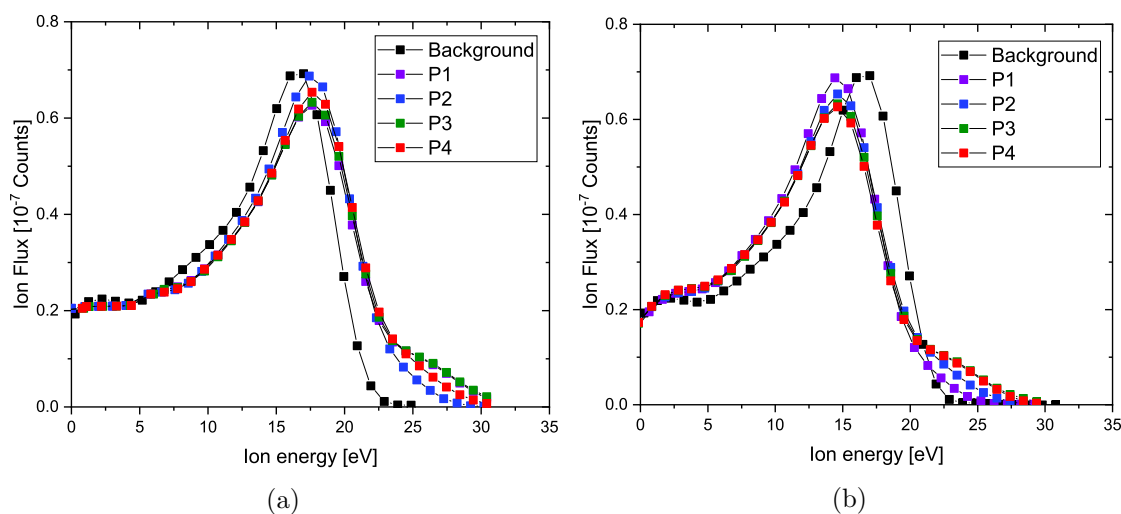


Figure 5.18: Ion energy data taken for a positive (a) and negative (b) polarity pulse at the four phase positions as outlined in figure 5.5, the negative pulse shows an overall lower ion energy value and greater consistency, which is preferential for the measurements taken in chapter 6. The plasma is operated at 50 W with a pressure of 10 Pa and gas mixture of O₂/Ar (98%/2%), with a pulse voltage of 100 V_{pp}.

becomes less negative to ensure that fewer ions hit the surface. This explains the small decrease in ion energy but largely similar pulse structure. For the positive pulse electrons are repelled, as the dc bias becomes more negative resulting in more ions at the surface with higher energies. There is much less difference between the phases when a narrower and more controlled pulse is implemented for both the positive and negative pulse case. The background measurement has an ion energy of 17 eV with the positive phases extending no further than 3 eV above the background ion energy measurement ≤ 20 and in the negative pulse case ≥ 14 . As the plasma assisted ALD environment develops further, there is an expectation that all ion energies will have limited operational ranges e.g (19 - 27 eV) which are dependent on the process and material.

In this case the background ion energy is approx. ~ 5 eV below the first set of measurements taken on the GEC cell using the initial TVW this is due to the alterations of the hardware and diagnostic configuration thus outlining the importance of a stable system to baseline these measurements on.

Combining the above conclusions, it has been demonstrated that a major consideration in the use of pulse induced OES will be the compromise between having easily observed emission with a high signal-to-noise ratio and minimising the influence of the pulse on the

plasma. These are specific to the test case, but are likely to be valid for other plasma conditions as well. The ion bombardment of semiconductor materials has been researched by Wang et al [118] in a GEC reference cell with a Ar/O₂ plasma, while Gudmundsson has also investigated an oxygen plasma looking at ion energy distributions of O⁺ and O₂⁺ [119]. Both demonstrate similar ion energies with Gudmundsson observing a mean ion energy increase from 10 eV at 2.7 Pa to 25 eV at 0.4 Pa. As previously mentioned Profijt et al examined ion-surface interactions for oxygen plasmas in an Oxford Instrument FlexAL reactor; used primarily for engineering nanoscale structures in remote plasma assisted atomic layer deposition (ALD) processes. These measurements were performed at pressures of 0.5 - 25 Pa and powers of 100 - 500 W [115]. The ion energies didn't exceed 35 eV and the conclusion being that the ion energies were low enough to prevent ion-induced film damage for ALD processes. In comparison with this work, only ion energies in the initial TVW design exceeded the 35 eV value, for the modified design these values were typically in the region of 17 ± 3 eV. Based on the conclusions in this chapter we can say that high pulse voltages lead to more observable emission and a higher signal-to-noise ratio, but lead to a greater influence of the pulse on the ion properties, which may be a disadvantage for processes. The use of positive polarity pulses allows for greater emission closer to the electrode surface than negative polarity pulses. However, negative polarity pulses are better for imaging the centre of the plasma. In this way, the two pulse polarities may be used to diagnose different parts of the plasma. Positive polarity pulses tend to lead to a greater effect on the ion properties, which again may be a problem for applications. The pulse repetition frequency was found to have a strong effect on the influence of the pulse on the ion properties. This does not change the pulse emission on individual images, but does change how often the ICCD camera can image the pulse. This means that lower repetition rates require longer camera exposure times to achieve the same signal-to-noise ratio. However, they have the advantage of influencing the ion properties less.

In conclusion, the PiOES measurements in the following chapters will focus on using a negative pulse polarity (less influence on ion properties) and an intermediate pulse frequency (less influence on ions) along with a variable pulse voltage in order to clearly observe pulse induced emission. The pulse voltage will need to be greater than $70 V_{pp}$ and will therefore occur in the region of $100 - 350 V_{pp}$ to allow sufficient pulse induced emission

across the 200 - 1000 W power range. The greatest improvement was seen when switching from the initial pulse design to the modified TVW, this highlighted the inefficiencies of the initial hardware and pulse design. The ion energy variation is reduced from 0 - 12 eV (initial TVW design) across a single RF phase measurement down to 0 - 5 eV for the developed tailored waveform. The discrepancies in phase and polarity have been reduced for the developed TVW design with only minor ion energy changes $17 (\pm 3)$ eV between the phases and polarity measurements which suggests the modified design is less impactful on the ion energies and therefore more applicable to a range of plasma processes.

Chapter 6

Measurements and simulations of atomic oxygen densities and gas temperatures

A central feature of semiconductor processing is to produce high quality final products onto the wafer substrate via plasma assisted processes, these include the addition, modification or removal of material under closely monitored conditions. This is captured in the etching rate, which must be controllable and highly uniform across each individual feature and the entire wafer.

This chapter presents atomic oxygen and gas temperature measurements on the GEC reference cell using the TALIF technique to investigate a wide power and pressure range, in both capacitive and inductive modes. The trends in these measurements are presented as a function of the gas mixture, pressure and plasma power. Specific trends including atomic density and gas temperature are compared with HPEM plasma modelling results. These results are used to benchmark PiOES-ERA as a method of obtaining atomic oxygen densities in a low pressure oxygen plasma. These comparisons are used to identify the strengths and weaknesses of the PiOES-ERA technique in its current form.

Oxygen as a primary feed gas have been chosen due to its extensive use in the semiconductor manufacturing industry. It provides an alternative to wet stripping techniques which are messy and leave corrosive by-products, oxygen plasmas are able to clean resid-

ual polymers from surfaces, such as SiO₂ wafer layers as oxygen plasmas can do so with minimal damage and precision accuracy [120]. They are also used for removal of organic polymers and in lithography processes for resist thinning, which is key for reducing the gate length without complicating the lithography process [121,122]. Photoresist ashing also uses O₂ chemistries to remove photoresist mask layers [123]. Finally, O₂ based chemistries are also used to etch organic and hybrid low-k dielectrics, which can be patterned using SiO₂ [124]. In high pressure oxygen discharges (50 - 600 Pa) the primary etchant is O atoms [125,126]. Where the etching rate of the O atoms is depended on power and gas mixture of the plasma, it has been shown that the thermal accommodation coefficient α_E is key in determining the neutral gas temperature which also impacts the O density and ion bombardment energy [70]. A change in the plasma properties will result in reduced atomic oxygen density and thermal energy for surface interactions, therefore a wide parameter study will look at these properties across the two plasma modes with an aim to develop a pulse technique to extract atomic oxygen values and gas temperatures without impacting the plasma processes.

6.1 TALIF measurements of O atom densities and gas temperature

In order to benchmark the PiOES-ERA results TALIF measurements using identical plasma conditions will be compared in order to quantitatively assess the effectiveness of the minimally invasive pulse induced OES technique. TALIF excites oxygen atoms (with a 2% argon admixture) in order to obtain absolute atomic oxygen densities as discussed in section 3.3. A calibration of the system is also performed using a xenon gas and identical system parameters. By generating laser pulses of 5 ns width at energies of 800 μ J and a laser wavelength of $\lambda = 225.58$ nm, two photon excitation of ground state atomic oxygen is achieved. Continually monitoring and stabilizing the shot-shot pulse energy through a feedback loop attached to the attenuators, it is possible to maintain a stable laser pulse around the baseline. The experimental procedure for obtaining the time resolved emission from atomic oxygen after excitation is interchangeable to that of the PROES measurements, with an identical camera position relative to the chamber window and only a filter

change required. The fluorescence radiation of the atomic oxygen is measured at $\lambda = 844$ nm, with the camera now synchronised to the laser pre-trigger. The temporal fluorescence decay is measured in 2 ns time increments as per the PROES measurements.

The laser and plasma both require a warm up and stabilisation period, both for the gas chemistry and also temperature. For normal operation the laser was left for up to 2 hours and the plasma a similar time frame, the lab space was also air-conditioned to keep the room temperature at 20 °C. The laser energy was measured before passing through the GEC cell and again at the beam dump after, this was performed at the start and end of the day as well as before and after each separate set of measurements. Within this typical operational time frame the laser energy would drift 0.5—1% an hour over the course of a day (7 hours) resulting in a total 3.5 - 7% error estimation for the 7 hour period. When changing the plasma parameters such as power or pressure, the system is left for an additional 10 minutes to allow the new plasma conditions to stabilise. Figure 6.1, is an example of the laser induced emission relative to the plasma emission at the top of the figure. It is an O₂/Ar plasma (98%/2%) at 150 Pa and operated at 800 W, these measurements include a PiOES pulse voltage that varied from 100 to 350 V_{PP} with increasing power and pressure. Under these conditions, the plasma is just beyond the transition between E- and H-mode. The laser beam passing through the discharge region is subsequently focussed down in front of the lower electrode and the excitation of the ($2p^4 \ ^3P_0$) ground state into ($3p \ ^3P_{1,2,0}$) state and subsequent decays into the 3s 3S state emitting a photon at 844.64 nm. The TALIF fluorescence is detected perpendicular to the incident laser beam. The beam size has been calculated according to the size of the ICCD chip and distance between the electrodes, this results in a beam width of 0.96 mm.

To ensure the laser pulse energy does not induce any photoionisation due to high laser fluence, the square root of the TALIF signal as a function of the laser energy is measured and plotted as shown in figure 3.16. For atomic oxygen, the saturation occurs around 850 μJ , as a result, the following measurements were taken at 800 μJ . For the xenon saturation calibration, a central wavelength of 222.17 nm was used, where saturation occurred at 130 μJ so a laser pulse energy of 100 μJ was chosen for calibration. The total systematic error estimation on the TALIF measurements in an O₂/Ar gas mixture considers the 650 to 850 nm emission lines, which are close to the maximum possible quantum efficiency

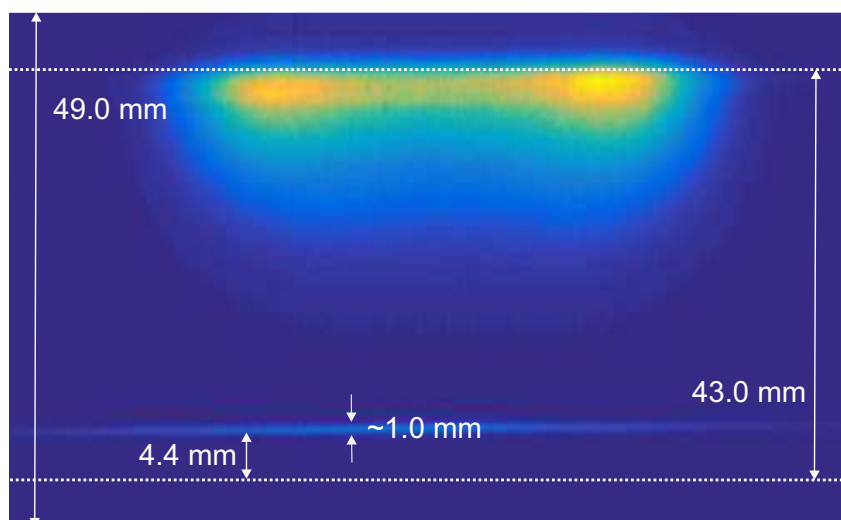


Figure 6.1: 844 nm emission of an O_2/Ar plasma (98%/2%) operated at 800 W with a system pressure of 150 Pa and TALIF laser energy of $800 \mu\text{J}$. The dotted white lines represent the electrode surfaces. This figure represents a 2 ns image taken from the full wavelength sweep, illustrating the position of the plasma and TALIF laser beam.

of the photocathode in the ICCD camera ($> 25\%$). The documentation doesn't specify an error, however when considering the variation in manufacturers for components such as the focussing lens, filters and camera this is estimated to be in the region of $\pm 10\%$. Which includes the ratio of the optical transmission of the ICCD focussing lens and bandpass filters (Andover Corporation) $750.4 \pm 0.5 \text{ nm}$, $777.5 \pm 1.75 \text{ nm}$ and $844.6 \pm 0.95 \text{ nm}$. The radiative lifetimes of $\text{O}(3p^3P_j)$ are 34.7 ± 1.7 and $\text{Xe}(6p'[3/2]_2)$ 40.8 ± 2.0 are taken from the work of Niemi et al [2]. His work also references the two-photon excitation cross section ratio of $\sigma^2_{\text{Xe}}/\sigma^2_{\text{O}} = 1.9$ with an estimated total overall uncertainty of 20 %, which will be applied to the TALIF measurements.

A number of studies have looked at atomic oxygen density [2,56,127,128] and methods for gas temperatures measurements [54, 129] over E-H modes or more specific plasma powers in order to understand how plasma density impacts key plasma processes. This will inform the future fabrication of three-dimensional (3D) nano devices that require atomic scale control of ion-assisted reactions [5]. To baseline these results a power and pressure series will be investigated, using TALIF to study and understand the current limitations of the PiOES-ERA technique.

6.1.1 Atomic O densities

The complete pressure and power study using TALIF is plotted in figure 6.2 with gas pressures ranging from 20 — 250 Pa and input powers starting at 200 W and increasing through to 1000 W in 200 W increments. Figure 6.2a shows an increasing trend of O atom density as a function of power and gas density, the increase in plasma power stimulates more electron impact dissociation of O₂, which is due to an increase in power being deposited into the coil and subsequently heating the electrons directly below it. This results in more dissociation of molecular oxygen using the reaction pathway ($e^- + AB \rightarrow A + B + e^-$) and producing two oxygen atoms with a thermal energy dependent on the dissociation pathway [130]. By considering the increase in system pressure and the availability of gas to dissociate, it provides an obvious and simplistic conclusion to the increasing density, however the change in wall loss rate (k_{wall}) is also impacted by system pressure which directly affects the atomic oxygen density due to a reduction in recombination at the reactor walls. Both these factors will play an important role in the overall atomic oxygen density. This will be explained in more detail later in this chapter.

Measurements taken using the GEC have been benchmarked against other GEC reference cells and similar references studies investigating oxygen plasmas, these studies all fall within the large power and pressure range set out in this work. The atomic oxygen density at 200 W and 20 Pa is $7.43 \times 10^{19} \text{ m}^{-3}$ increasing to $3.53 \times 10^{21} \text{ m}^{-3}$ at 1000 W and 250 Pa, corresponding to an increase of almost a factor of 50. Zeng et al measured atomic oxygen densities in ICP plasmas at powers of 500 and 1000 W at 10 Pa of $1.13 \times 10^{20} \text{ m}^{-3}$ and $2.89 \times 10^{20} \text{ m}^{-3}$ respectively. When compared with the measurements taken in the GEC at 500 and 1000 W it resulted in values of $3.82 \times 10^{20} \text{ m}^{-3}$ and $8.81 \times 10^{20} \text{ m}^{-3}$ which is slightly above Zeng's work, however the GEC system pressure was 25 Pa which could explain the higher O atom density [127]. Gudmundsson et al modelled a planar inductive oxygen discharge at 1000W and 8 Pa which simulated oxygen densities of approximately $1.00 \times 10^{21} \text{ m}^{-3}$ which is in reasonable agreement with the 20 Pa and 1000 W measurement performed on the GEC, noting that the system configuration and gas flow rate are important factors when comparing similar pressure and power measurements [131, 132]. Three different E-H mode transitions were visually observed for 20, 150 and 250 Pa. With

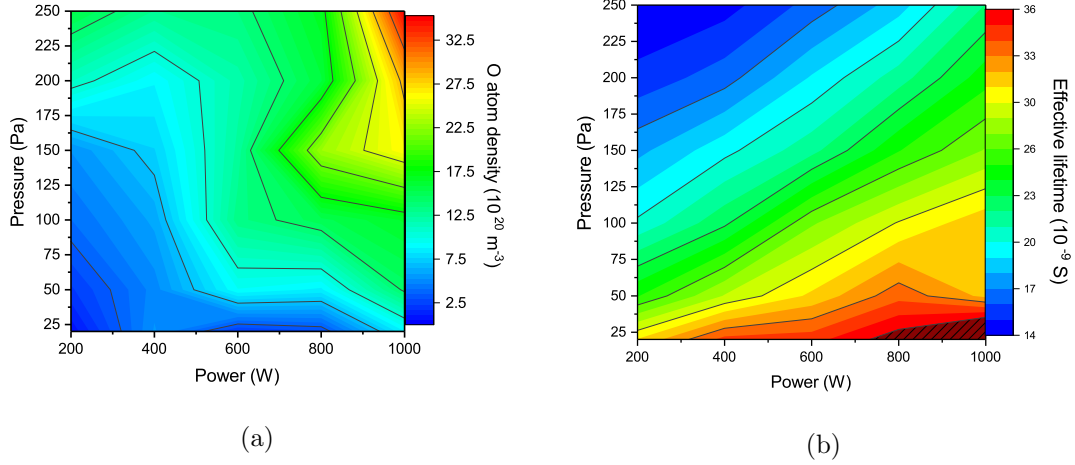


Figure 6.2: Atomic oxygen density contour plot (a) measured in a plasma operating a gas mixtures of O_2/Ar (98%/2%) and increasing pressure (0 - 250 Pa) and plasma power (200 - 1000 W) values, the atomic oxygen densities increase with both pressure and power, while the effective lifetime (b) of atomic oxygen in the same pressure and power parameter range also increases with plasma power.

an increase in the RF power from 200 - 1000 W, the discharge changes from an E-mode to a hybrid E/H-mode and finally pure H-mode, as demonstrated by Wegner et al [22]. The transition points are noticeable in all the chosen pressures; at 20 Pa it occurs between 200 - 300 W which resulted in an O atom density increase of a factor of 5, whereas for the 150 Pa case the transition started at 600 W and was in a pure H mode by 750 W which resulted in an O atom density increase of factor 2 between the modes, finally for 250 Pa measurement the transition occurred between 800 and 1000 W, resulting in an increase of factor 2 from $1.68 \times 10^{21} \text{ m}^{-3}$ to $3.52 \times 10^{21} \text{ m}^{-3}$. While investigating surface loss coefficients in oxygen plasmas, Gomez et al measured O atom densities using TALIF at a pressure of 50 Pa and power of 250 W as $1.00 \times 10^{20} \text{ m}^{-3}$ which closely compares to the 50 Pa and 200 W measurement of $2.23 \times 10^{20} \text{ m}^{-3}$ taken on the GEC using TALIF.

As the pressure increases the O atoms will diffuse less to the walls, which means fewer O atoms are lost due to the increased pressure, this can be observed in figure ?? where the k_{wall} values for a 200 W plasma show a decrease in the wall loss rate at pressure above 100 Pa. This will be described in more detail below, with the introduction of wall loss rate k_{wall} .

The work of Tsutsumi et al [38] considers recombination to the chamber wall as being

one of the largest loss mechanisms for this system configuration and under these operational conditions, when comparing it to loss rates through pumping or destruction via three body processes. In general, as the pressure is increased, surface losses would be expected to decrease as the diffusion of atomic oxygen to the walls becomes more difficult. With few studies looking at the atomic oxygen recombination rate α in low pressure plasmas, Gibson et al. has taken a range of recombination rates from 0.01 [133] to 0.5 [134] and modelled them using HPEM at a low gas pressure of 1.33 Pa and plasma power of 500 W to highlight surface losses [70]. In his work, atomic oxygen density and gas temperature are plotted as a function of the recombination coefficient, where the atomic oxygen density decreases with increasing recombination coefficient from $8.3 \times 10^{19} \text{m}^{-3}$ to $5.9 \times 10^{18} \text{m}^{-3}$ and the temperature remaining relatively constant at 860 - 990 K. The O atom density decreases as a result of the increasing recombination coefficient which converts O to O₂ at the surface. Figure 6.2a illustrates that with increasing pressure, higher O atom densities are measured due to less recombination at the reactor walls, as well as additional molecular oxygen O₂ to dissociate, meaning both the increased dissociation and reduction of wall losses are contributing to the overall density. Gomez et al. has shown that the surface recombination probability of atomic oxygen decreases with increasing pressure, as the small O atom flux to the surface at low pressures means that for each of the chamber surfaces, every arriving atom will have a higher probability of sticking or recombining than those at a higher system pressures. For similar pressures, in an inductive mode plasma the flux of O atoms are higher due to having a greater density and higher velocity [4]. Guha et al investigated photoresist etching in O₂ containing plasmas, where a decrease in etch rate was observed due to deposited materials on the chamber walls decreasing the O atom concentration and increasing the O atom recombination rate [133].

The role of surface processes can be more clearly considered following the approach of Tsutsumi et al [38], Booth and Sadeghi [134], Corr [27] and Chantry [135]. These studies defined the wall loss rate of atomic species, k_{wall} as:

$$\frac{1}{k_{wall}} = \frac{\Lambda_0^2}{D} \frac{V}{A} \frac{2(2 - \alpha)}{\bar{v}\alpha} \quad (6.1)$$

The diffusion length Λ_0 is defined by the reactor geometry, and D is the diffusion

coefficient. The volume of the container V and surface area A are the values for the GEC cell. The atomic oxygen and the mean velocity of atomic oxygen $\bar{v} = \sqrt{(8k_B T)/(\pi m_o)}$ and α is the atomic oxygen wall recombination coefficient. For a cylindrical reactor the diffusion length Λ_0 is defined as;

$$\frac{1}{\Lambda_0^2} = \left(\frac{\pi}{L}\right)^2 + \left(\frac{2.405}{r}\right)^2 \quad (6.2)$$

Where the length (L) and radius (r) refer to the geometry of the reactor. The diffusion coefficient of atomic oxygen within a molecular oxygen gas is taken as;

$$D = \frac{3}{8n_{O_2}\sigma_{12}^2} \sqrt{\frac{k_B T}{2\pi} \left(\frac{1}{m_O} + \frac{1}{m_{O_2}}\right)} \quad (6.3)$$

This expression is taken from the work of Chapman and Cowling [136] and gives the diffusion coefficient from a species in a binary mixture of gases. n_{O_2} is the density of molecular oxygen, masses m_O , m_{O_2} of atomic and molecular oxygen respectively while σ_1 and σ_2 represent the Lennard-Jones collision cross sections for atomic and molecular oxygen, where $\sigma_{12}^2 = (\sigma_1 + \sigma_2)/2$.

Since surface losses are important for O atom density, these equations can be used to help explain the trends observed in figure 6.5b. As the pressure is increased at 200 W, the O atom density increases linearly between 20 Pa and 150 Pa. After 150 Pa, the gradient of its increase gets steeper. A possible explanation for this change of gradient, is a combination of increasing gas density and decreasing gas temperature, which can explain a decrease in the diffusion coefficient of O atoms (equation 6.3), in combination with the decreasing value of α and increasing pressure [4]. The wall loss rate (k_{wall}) has been plotted as a function of pressure and temperature to indicate the regions where wall losses are dominant across the 20 - 250 Pa pressure range at 200 W, it can be seen that the gradient between 100 - 150 Pa reduces, resulting in less recombination at the walls for the higher pressures.

For the 1000 W case, the increase in O atom density with pressure has the same gradient over the pressure range of the measurements. In this case, the higher gas temperatures at 1000 W mean that the diffusion of O atoms to the surface is higher when compared to the 200 W case because the gas temperature is lower. Even though the diffusion coefficient

and α decrease with increasing pressure, the value of the diffusion coefficient is higher than for the 200 W case, resulting in a transition between the two different gradients in the O density as a function of pressure which does not occur in the pressure range of these measurements.

Figure 6.3 is a plot of the dissociation degree, which is defined as the density of atomic oxygen divided by the density of molecular oxygen (n_O/n_{O_2}). The contour plot describes areas of higher dissociation degree that may be of interest for industrial applications, as the O to O₂ ratio changes due to the plasma conditions. A decreasing dissociation degree at higher pressures and lower powers is due to the decrease in electron temperature and therefore lower electron impact dissociation rates.

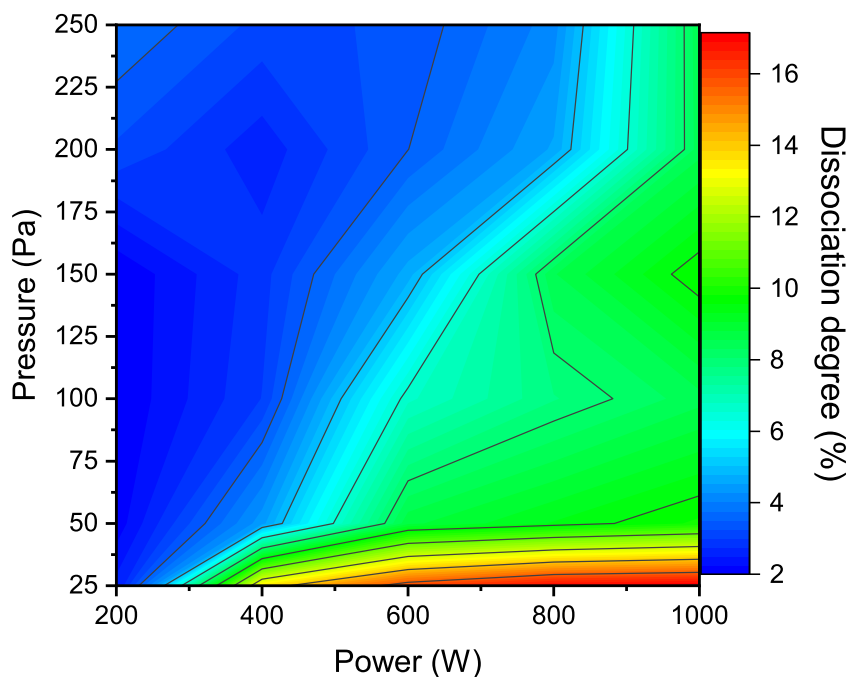


Figure 6.3: Contour plot of the dissociation degree as a function of system pressure and power. Increasing dissociation is observed at higher plasma powers as the electron density increases and influences the electron impact dissociation rates. Gas mixture is O₂/Ar (98%/2%).

Having discussed the general trends in O density, we can now look at some specific trends in more detail. Figure 6.4f shows the O atom density for pressure of 150 Pa at five power increments. A jump in O atom density is observed between 600 and 800 W. This jump corresponds to the E-H mode transition, which is demonstrated in the PROES

images at increasing plasma powers as shown in figures 6.4a - 6.4e. Figure 6.4a shows the plasma operating in E-mode, which typically has low plasma density. E-mode is indicated by one excitation structure in the RF cycle as a result of the motion of the plasma sheath. As the power is increased a critical electron density is reached, causing the plasma to transition into H-mode. This can happen gradually or in a step like manner. At lower pressures a more gradual transition is observed, while at higher pressures it exhibits a more step like transition, as shown in figure 6.5a. This is indicated in the PROES images by a second excitation structure becoming stronger between 400 and 600 W until at 800 W the plasma has fully transitioned into H-mode, indicated by two mirrored excitation structures close to the coil. This is a product of the azimuthal movements of electrons due to the inductive heating. The emission intensity also increases significantly between 600 and 800 W. The point of transition between E and H mode agrees well with the sharp increase in O atom density between ~ 550 and 800 W. The PROES images of the E-H mode transition agree well with those measured previously by Wegner et al [22] and Zaka-ul-Islam [137].

The mode transition in figure 6.4 exhibits an O atom density increase of factor 2 across the E-H mode transition at 150 Pa, this transition occurs between ~ 550 W to 800 W. In the work of Zaplotnik et al, the E-H mode transition at 160 Pa occurs between powers of 600 W and 800 W with a factor 2 increase in O atom density from $1.0 \times 10^{21} \text{m}^{-3}$ to $2.0 \times 10^{21} \text{m}^{-3}$. The plasma is operated at 13.56 MHz, however the experimental configuration is slightly different as the coil surrounds a glass discharge tube [138]. It is noted by the author that O atom density does not depend on the discharge mode when operating below 10 Pa, where the first increase in O atom density across the E-H transition mode is observed at 20 Pa. Zeng et al has investigated the E-H transition region for oxygen gas pressure of 10 - 100 Pa and powers of 0 - 2 kW; at 20 Pa the transition is measured between 600 and 700 W, for 50 Pa it is slightly higher at 900 and 1000 W and finally for 100 Pa the E-H transition region is measured between 1500 and 1600 W. In comparison, the values measured in this work are 200 - 300 W for 20 Pa, 300 - 400 W for 50 Pa and 550 - 750 W for 150 Pa as measured on the GEC system using TALIF. The difference is a factor 2 which is fairly significant, however, Zeng was operating in a much larger system with an inner diameter of 300 mm and height of 463 mm. The measurements carried out in this chapter also follow similar trends to the E-H mode and O atom density measurements and

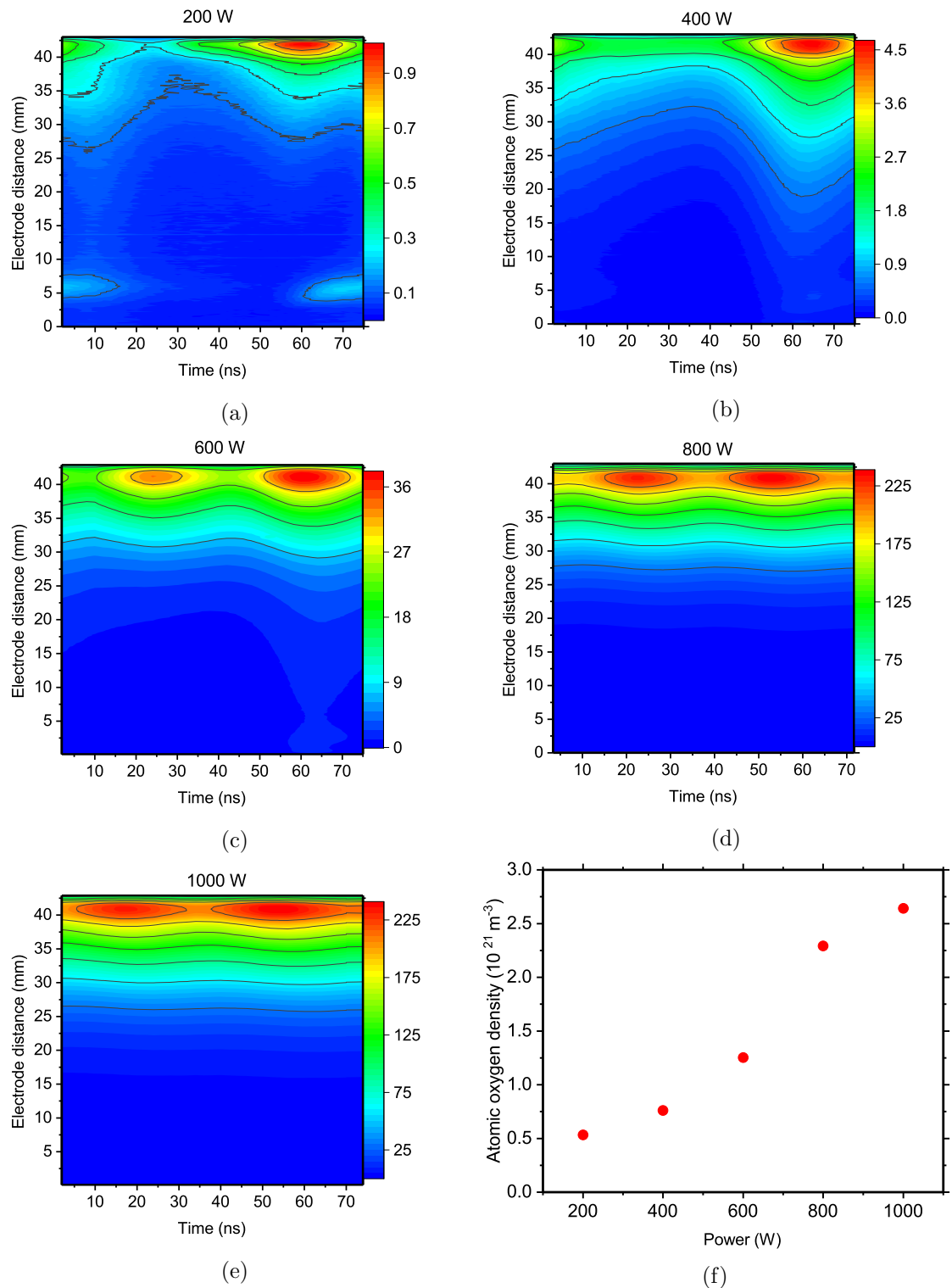


Figure 6.4: PROES images and plots indicating an E-H mode transition in an oxygen plasma with small argon admixture. The mode transition can be observed in both the PROES images and clearly in the plot of atomic oxygen densities. It is marked by the addition of a second sheath structure (plot (c)) and the jump in oxygen density as shown in the final plot (f). The plasma pressure is 150 Pa and incremental plasma power measurements of 200 - 1000 W. Gas mixture is O_2/Ar (98%/2%).

simulations performed by Corr et al, these were taken on a GEC reference cell at 6.66 Pa in an oxygen plasma and produced atomic oxygen densities of 10^{19}m^{-3} to 10^{20}m^{-3} , where the E-H mode is observed between 27 and 220 W [27].

Figure 6.5a shows the O atom density as a function of power from 200 - 1000 W, increasing in 200 W increments as shown in figure 6.2a. The figure includes a 20 and 250 Pa set of measurements. The 20 Pa results show an increase in O density from 200 - 400 W before dropping off and slowly increasing again between 600 - 1000 W, the slow drop off could be due to thermal effects which would initially impact the recombination rate, a jump in gas temperature is observed in figure 6.7a where a higher gas temperature could increase the O atom recombination and therefore a drop in O atom density. In the 250 Pa power variation, a mode transition occurs between 800 and 1000 W, with the O atom density increasing by more than a factor of two in this range.

For the 200 and 1000 W O density measurements in 6.5b. The approximately linear upward trend of the O atom density with pressure is observed. This is largely determined by the increase in total gas density as the pressure increases. Overall, the observed trends are caused by a number of factors, such as mode transitions between E- and H-mode, which cause sharp changes in densities as well as the impact of surface loss processes at different pressures and powers. The error included here is the quantum efficiency of the system as well the two photon excitation cross section ratio totalling 20 %, not to be confused with the 20 % for the gas temperature measurements that which was due to the quenching coefficients for both O and O₂.

6.1.2 Gas temperature

Figure 6.2b is the TALIF effective lifetime as a function of power and pressure. At powers of 800 and 1000 W in a 20 Pa system the results illustrate a region where the neutral gas density was low enough for the effective lifetime to be approximately equal to the natural lifetime, as indicated by the hatched region in figure 6.2b The effective lifetime decreases with increasing pressure as the background gas density also increases, this leads to an increase in the collisional quenching rate. The effective lifetime increases with increasing power as the gas temperature increases, leading to a decrease in the background gas density at a constant pressure, resulting in a decrease to the collisional quenching rate

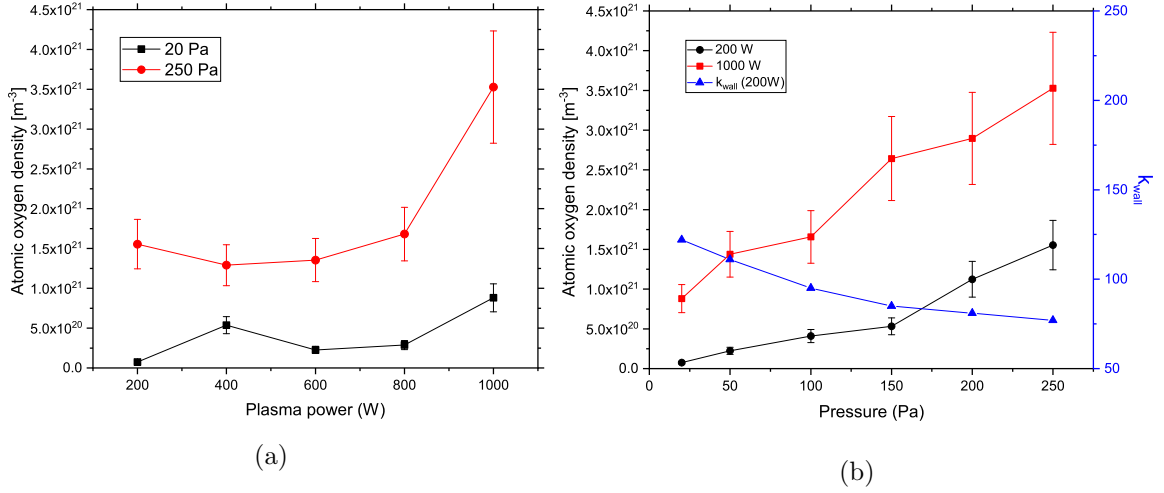


Figure 6.5: TALIF measurements of absolute O density as a function of plasma power (a) and pressure variation (b) are plotted, laser energy was $800\mu\text{J}$ as previously calibrated. Trends vary significantly depending on pressure and power with possible thermal effects which would impact recombination rate, the consideration of surface loss processes at different conditions is also a factor. Gas mixture is O_2/Ar (98%/2%).

which increases the lifetime.

These results include a transition from E-H mode for each power, where the E-mode is characterised by a higher electron temperatures which switches as it transitions into an H-mode. A lower electron temperature but higher electron density is observed in a fully transitioned H mode [22,26]. The gas temperature is also of interest as it directly impacts the ion energies close to the plasma-surface interface, the plasma density and electron temperature significantly influence the charged particle collision processes [139].

The gas temperatures in this work are calculated using the ideal gas law and radiative lifetime results from the PROES measurements. The quenching coefficient of excited O atoms interacting with ground state O atoms (k_{q_0}) were taken from the work of Dilecce et al [140] and the coefficient for excited O atoms interacting with O_2 molecules ($k_{q_{\text{O}_2}}$) from Niemi et al [2]. Niemi et al included an associated error of 20 % with the quenching coefficient $k_{q_{\text{O}_2}}$, whereas the coefficient from Dilecce et al k_{q_0} is considered an upper limit and an inefficient quencher therefore a total 20 % error will be estimated for both values. Equation 6.4 is the rearranged form of the equation for the lifetime of excited atomic oxygen. Since all the other terms are known from the TALIF measurements, n_{O_2} can be calculated. When combined with the ideal gas law, the gas temperature, T_{gas} , can be

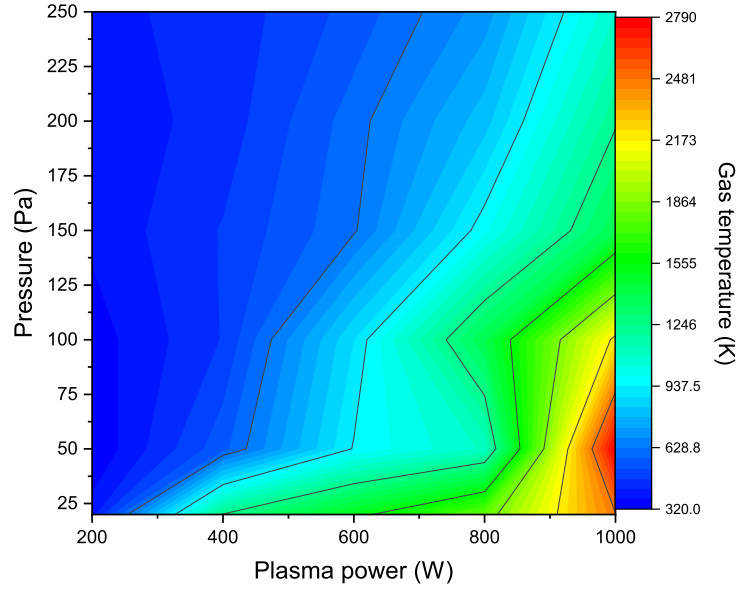


Figure 6.6: Gas temperature contour plot for a power (200 - 1000 W) and pressure (20 - 250 Pa) variation. Gas temperature peaks at an increased plasma power while higher system pressures suppress the temperature due to an overall lower average gain per molecule. Gas mixture is O₂/Ar (98%/2%).

deduced.

$$n_{O_2} = \frac{1}{\tau k q_{O_2}} - \frac{A_{23}}{k q_{O_2}} - \frac{n_O k q_O}{k q_{O_2}} \quad (6.4)$$

$$T_{gas} = \frac{p}{kB (n_{O_2} + n_O)} \quad (6.5)$$

Figure 6.6 illustrates the gas temperature scaling with an increasing RF power, however it is suppressed by the higher gas pressure which is illustrated in the contour plot. Figure 6.7a illustrates the calculated gas temperature increase for the individual pressures over the power range 200 — 1000 W. The gas temperature increases with power, as more power is available to heat the gas. In O₂ plasmas at low pressures one of the main gas heating mechanisms is via the Frank-Condon principle, which occurs when an O₂ molecule is dissociated [70]. This scales with the electron density and therefore with power.

The gas temperature tends to decrease with increasing pressure at constant power as the same amount of gas heating is dissipated in a larger number of background gas molecules and therefore the average energy gain per molecule is lower. High gas temperatures were measured in a low pressure ICP (1 - 10 Pa) by Foucher et al, where vibrationally

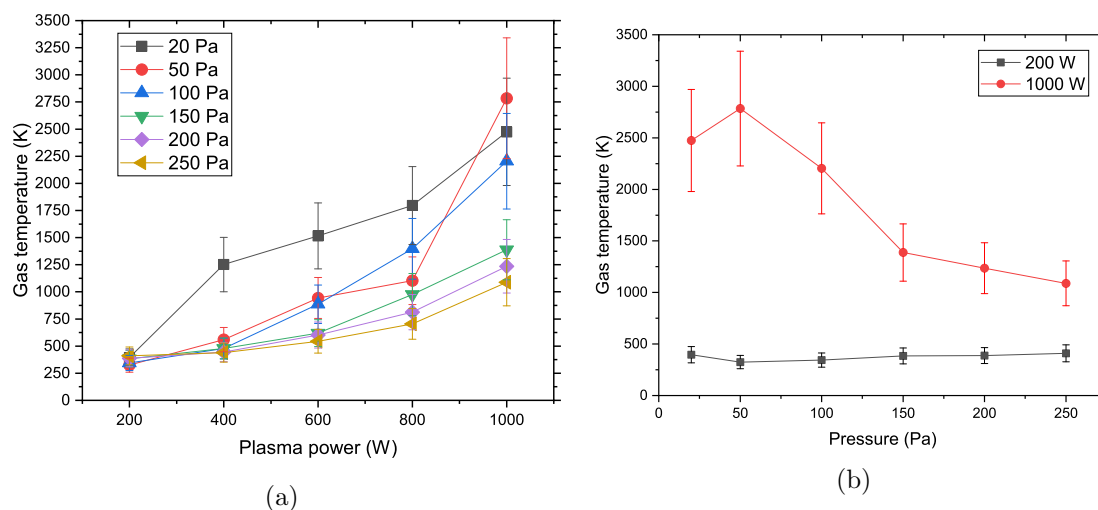


Figure 6.7: Line plot of pressure (20 - 250 Pa) (a) as a function of plasma power and gas temperature, and plot (b) showing the highest (1000 W) and lowest (200 W) plasma power measurements as a function of gas pressure and temperature. Gas mixture is O_2/Ar (98%/2%).

excited O_2 molecules were measured and analysed to obtain the rotational O_2 temperature, this showed a temperature increase with both pressure and power up to 900 ± 20 K in an O_2 gas chemistry at a plasma power of 500 W and a system pressure of 10 Pa. In comparison, temperatures measured in the GEC system at 20 Pa were 1380 ± 270 K, which show similar trends with an increase in gas temperature due to plasma power and pressure.

Figure 6.7b illustrates the gas temperature variation of the 200 and 1000 W measurements, the 200 W set for 20 - 250 Pa are similar with temperatures ranging between 300 - 400 K, while the 1000 W measurement has a much larger variation of 2800 K to 1100 K. These results highlight a significant gas temperature variation with increasing plasma power and pressure. The calculated gas temperatures are indicative of a system temperature trend which increases with less of a focus on the final numbers. Additional calculations which account for the temperature variations across the reactor would provide a more accurate result, with special focus on the plasma-surface interface to monitor the change in radical densities.

The work of Gibson et al, highlights the dependence of the plasma bulk properties and fluxes on the plasma-surface interface, these impact the atomic oxygen surface recombination coefficient and thermal energy coefficient in a low pressure ICP. The thermal

recombination coefficient plays a key role in determining the neutral gas temperature and therefore the neutral gas density. By varying both of the coefficients it was found that plasma properties were most sensitive to small values of each coefficient as they caused losses of atomic oxygen and thermal energy to be surface interaction limited [70].

6.2 Modelling atomic oxygen density and gas temperature

The experimental measurements have been simulated using a two-dimensional, modular, fluid-kinetic simulation code. The geometry as shown in figure 4.2 models a planar inductively coupled plasma which has been configured to match the exact dimensions of the GEC reference cell. The full list of oxygen and argon reactions are given in table 4.1. The reaction set from Gibson et al [70] has been configured to include all key reactions important at these pressures.

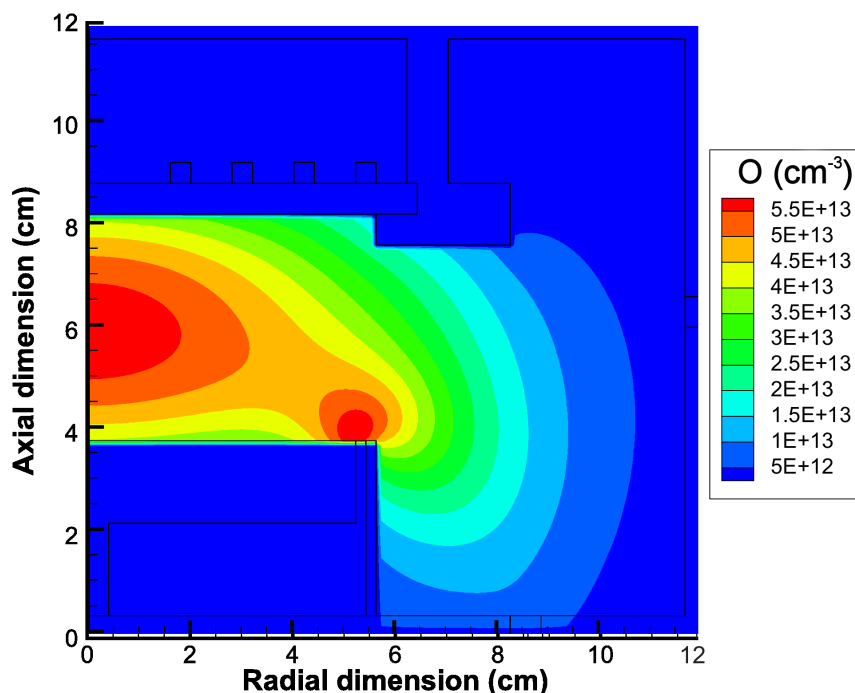


Figure 6.8: Atomic oxygen density simulation using the oxygen/argon chemistry set in chapter 4, modelled in a 200 W plasma with a pressure of 150 Pa, the high atomic density value at the electrode is a consequence of the edge effects between the electrode edge and ground ring and is only observed in the capacitive mode due to the strong electric fields generated in that axis. Gas mixture is O₂/Ar (98%/2%).

Figure 6.8 illustrates the O atom density for a 150 Pa and 200 W plasma. It is contoured to highlight the areas of highest O atom density which are in the centre of the plasma and also at the electrode-guard ring interface, this agrees with the dissociation degree measurements in figure 6.13. The atomic oxygen density peak at the edge of the electrode and guard ring is a consequence of edge effects, which have previously been modelled and observed experimentally in the GEC reference cell [38, 141]. Strong electric fields are generated in the capacitive mode as a result of these edge effects, which occur between the edge of the lower electrode and guard ring and produce higher electron temperatures which in turn generate more O atom density ($5.8 \times 10^{19} \text{m}^{-3}$). This is not observed once the plasma is in a full inductive mode.

In order to observe the E-H mode transition, the electron density for a specific plasma power (200 - 1000 W) is taken from an averaged section over the same spatial region above the lower electrode ~ 1 mm as the TALIF measurements, this is done for all the different powers at 150 Pa. The electron density illustrates a sharp increase between 400 and 600 W, corresponding to the E-H mode transition. The mode transition obtained from the experimental data shows a second structure at 600 W (figure 6.4) which implies the plasma is in a hybrid or mixed mode, however the emission intensity confirms it is close to the start of the mode transition.

The simulated atomic oxygen density is plotted as a function of power (200 - 1000 W) and pressure (150 Pa) with the TALIF densities in figure 6.10. A step like increase in the O atom density is observed over the 400 - 600 W region as modelled in the electron density plot in figure 6.9. The main production of atomic oxygen is through the transfer of electron energy into gas heating via the dissociation process as mentioned previously, this also generates thermal energy. Due to the low pressure of the system, mean free path between the gas phase collision is long, therefore the diffusion of O atoms to the GEC reactor walls happens quickly and results in wall losses being the dominant destruction pathway of the O atoms. Figure 6.11 compares the simulated gas temperature as a function of pressure at 150 Pa and an increasing plasma power. As the plasma power increases, the gas temperature initially remains constant for the 200 - 400 W simulations, whereas the TALIF measurements increase immediately with higher plasma power which is mirrored in the higher atomic oxygen density as plotted in figure 6.10. This could account for

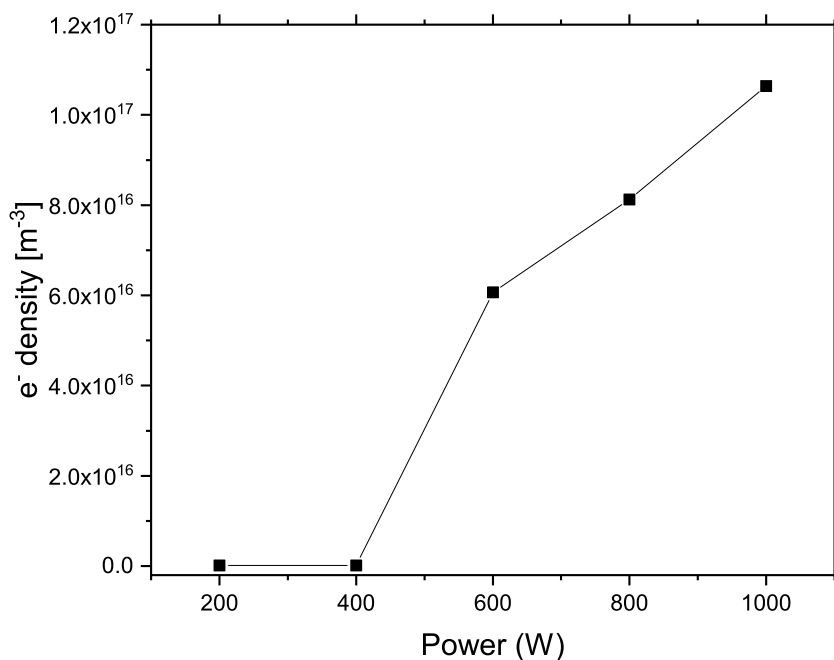


Figure 6.9: HPEM simulation of electron density as a function of pressure (150 Pa) and plasma power (200 - 1000 W) highlighting the step like increase in electron density due to increased plasma power and mode transition from capacitive to inductive plasma. Gas mixture is O₂/Ar (98%/2%).

additional heating processes that haven't been modelled in the HPEM simulations as all but one data point have lower gas temperatures. The electron density as measured ~ 4 mm above the lower electrode in the simulated environment confirms the 200 and 400 W simulations are in a capacitive coupling mode where the atomic oxygen density peaks at the centre of the plasma. The plasma begins to transition between operating modes > 400 W the gas temperature in both cases increases allowing electrons to gain enough energy to dissociate more O₂.

In general the simulations have fairly good agreement with the TALIF measurements, however the E-H mode transition occurs slightly before the GEC measured case, where the simulated gas temperature rises quicker between 400 — 600 W but then drops below the 800 W TALIF measurement.

6.3 PiOES-ERA + TALIF comparison

In this section, the focus is on using PiOES in combination with ERA to derive values for the dissociation degree/atomic oxygen density and the mean electron energy. These values

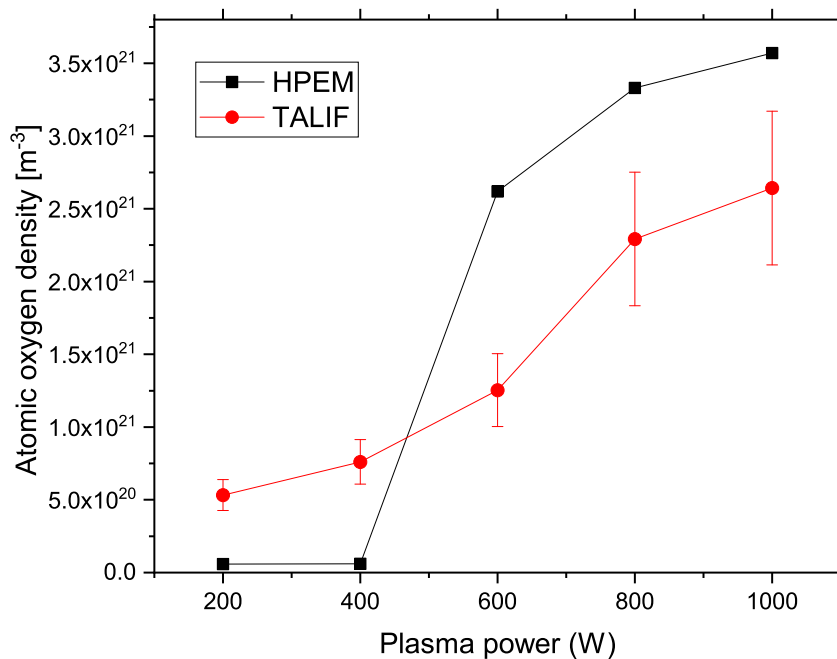


Figure 6.10: HPEM simulation and TALIF measurements compared over the same operational conditions of 150 Pa, with a plasma power variation from 200 - 1000 W. Both methods show similar trends in the E-H transition region with the HPEM model predicting a slightly earlier transition start period. Gas mixture is O_2/Ar (98%/2%).

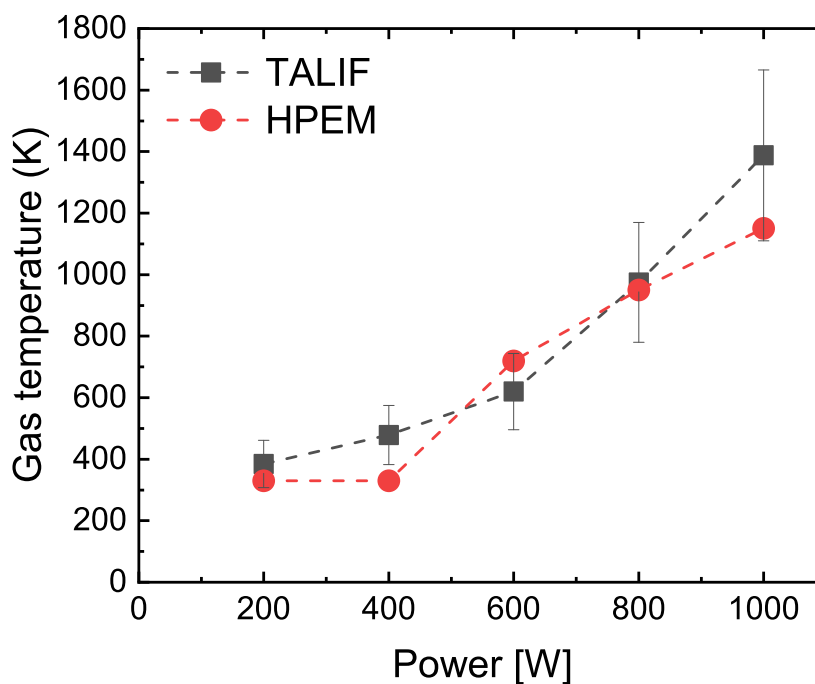


Figure 6.11: Comparison of the TALIF calculated gas temperatures and HPEM simulated results, as a function of plasma power (200 - 1000 W) and constant pressure (150 Pa). Gas mixture is O_2/Ar (98%/2%). These results have fairly good agreement with similar trends.

are obtained by comparing excitation ratios of oxygen and argon emission lines measured experimentally using PiOES with calculated values, as described in section 3.2.7. The atomic oxygen density is calculated from the dissociation degree derived from ERA using the ideal gas law. These atomic oxygen densities are then compared with those obtained in the previous sections using TALIF in order to validate the PiOES-ERA technique.

The plasma and pulse conditions have remained consistent throughout this section with only the plasma power, i.e. the power delivered to the inductive coil, and system pressure varying. The pulse has a negative polarity and consists of eight harmonics, measurements in chapter 5 showed less influence on the ion properties with an intermediate pulse frequency, the repetition rate is fixed at 226 kHz. The plasma is operated at 13.56 MHz with an 98%/2% oxygen/argon gas mixture, the applied pulse voltages were varied between 100 - 350 V_{PP} , this was to accommodate the reduced pulse emission measured in an H mode plasma. For the plasma conditions operating in E-mode the pulse voltages were $300 \pm 20 V_{PP}$ across the pressure range, while in H mode an input voltage of 350 V_{PP} only measured 100 V_{PP} at the electrode due to an increased background plasma voltage. Results from chapter 5 confirmed a 100 V_{PP} would be adequate, so the decision to carry the same tailored pulse design and voltage to the lower plasma powers was made with the caveat that slightly more disruption would occur in the plasma however the signal-to-noise ratio would make the ERA analysis more effective.

6.3.1 Pulse induced optical emission spectroscopy

PiOES data for the O(3p 5P) state over two RF cycles with the pulse applied to the lower electrode, as shown in figure 6.12 for two different pressures. At these relatively high pressures the emission from the plasma without the pulse applied is confined close to the inductive coil. This means that using ERA can only be effective when measuring the dissociation degree or mean electron energy in this region. This has been studied previously by Tsutsumi et al [38] for a capacitively coupled plasma. However, by applying a negative pulse and using PiOES the pulse-induced emission can cause emission close to the bottom electrode and in some cases across the whole electrode gap. At the 50 Pa pressure the influence of the pulse can be seen to extend from bottom to top electrode, which allows for the axial profile of the discharge region to be analysed using ERA and the dissociation

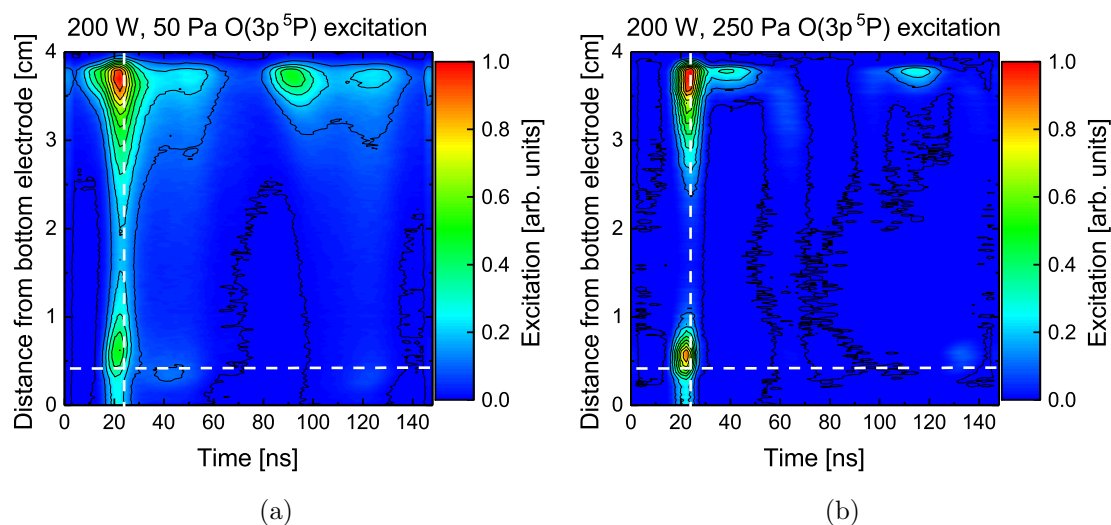


Figure 6.12: Comparison of PiOES images at 50 Pa (a) and 250 Pa (b). The dashed white lines mark the regions where ERA results have been extracted. The opposing pressures highlight the PiOES impact across the spatial region of the image with the higher pressure confining the stimulated emission to the lower electrode and the plasma clearly in a capacitive mode (plot (b)). Gas mixture is O_2/Ar (98%/2%) and the plasma is operated at 200 W.

degree and mean electron energy to be obtained across the entire axial dimension. This is significant as such measurements cannot easily be made using OES without the use of the pulse because of the low emission across most of the plasma. Such measurements are also difficult using TALIF as the laser must be scanned axially. In the higher pressure (250 Pa) case, shown in figure 6.12b, electron collisions in the bulk plasma mean that the influence of the pulse does not extend across the whole plasma, and so full profiles cannot be extracted. In such cases, PiOES-ERA is limited to smaller regions of time and space, but can still be used to extract the dissociation degree close to the bottom electrode. A consideration when applying the pulse is to factor the influence it may have on the sheath at the top of the electrode, both cases in figure 6.12 additional excitation features are visible as a result of the pulse at the top electrode. These could be minimised further by using a lower pulse peak-to-peak voltage, however, strong pulse-induced emission was favoured for these measurements in order to generate a good signal-to-noise ratio for the ERA measurements.

6.3.2 Axial profiles of dissociation degree and mean electron energy

The dissociation degree is defined as the density of an atomic species divided by the total gas density, and is directly inferred from the ERA measurements as described in section 3.2.7. For the results presented in this section a gas temperature of 400 K has been used to calculate the quenching rates in the excitation calculations. This is approximately consistent with the gas temperature calculated from the TALIF atomic oxygen lifetimes in the previous section for plasma powers of 200 W.

ERA has the capacity to measure dissociation degrees in any area that exhibits sufficient plasma emission. At all pressures studied, the pulse induced emission close to the electrode has sufficiently large emission to allow ERA to be used close to the electrode. However, at 50 and 100 Pa the pulse induced emission is large enough across the whole axial distance for ERA to extract the dissociation degree and mean electron energy across the whole gap. The dissociation degree for these pressures is shown in figure 6.13. For both cases the dissociation degree has a dome structure, peaking close to the centre of the gap. These results are consistent with the axial atomic oxygen density measurements of Gomez et al using TALIF in the same reactor [4].

The profiles look as expected; with the dissociation degree peaking at the centre and then decaying towards the surfaces as this is where the dominant loss of atomic oxygen happens through surface recombination. As the pressure is increased from 50 to 100 Pa the axial profile becomes slightly flatter, as a result of the decrease in surface losses the diffusion coefficient of O and the surface recombination coefficient decreases. This is also consistent with the measurements of Gomez et al [4]. An error estimation of 30 % has been applied, this corresponds to the systematic error introduced by the electron impact cross sections.

The mean electron energies derived from the ERA analysis across the electrode gap are shown in figure 6.14. As described in section 3.2.7, these are calculated assuming a Maxwellian EEDF. Assuming different EEDF shapes changes the value of the mean electron energy, but does not affect the observed trends. The mean electron energies for both pressures are highest in the sheath regions as these are the regions where electrons are being heated most efficiently by the movement of the plasma sheath. As the pressure

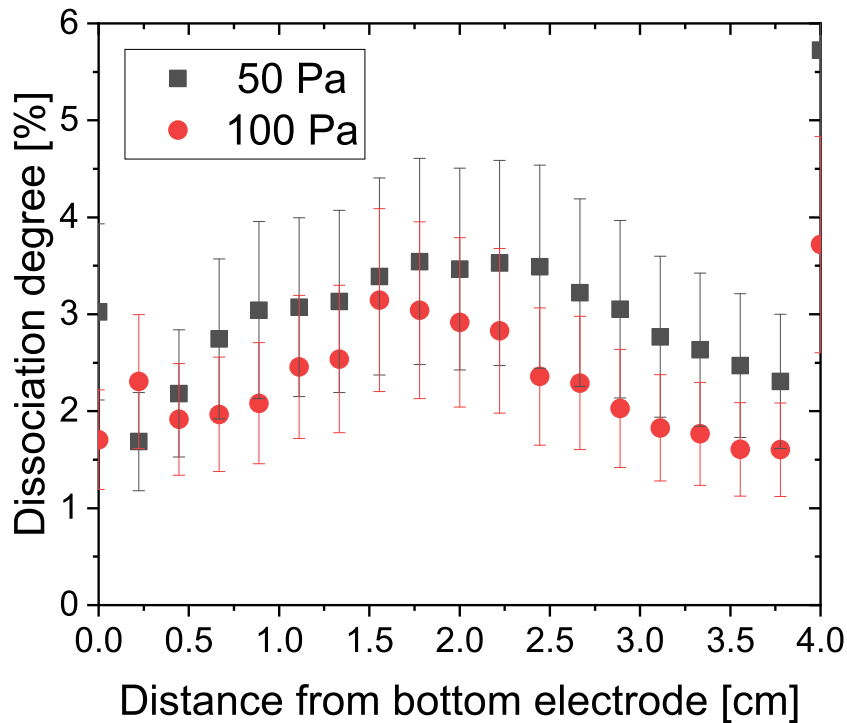


Figure 6.13: Dissociation degree profile for 50 and 100 Pa measurements within the region between the two electrodes. The highest dissociation degree occurs at the centre of the plasma where losses through surface recombination are lowest. Gas mixture is O₂/Ar (98%/2%) and the plasma is operated at 200 W.

is increased from 50 to 100 Pa the mean electron energy decreases as a result of higher electron collision frequencies with the background gas, resulting in a loss in energy. These trends are consistent with the previous experimental work of Tsutsumi et al [38], Kechkar et al [142], Stapelmann et al [143] and the Particle in Cell simulation results of Gudmundsson and Ventejou [144]. Where Gudmundsson's results of a 1D PIC simulation operated in an oxygen chemistry and CCP configuration illustrate a decrease in mean electron energy as the system pressure is increased between 1 and 66 Pa and a plasma voltage of 222 V.

As discussed, the edges of figure 6.14 correspond to the floating (0 cm) and powered electrode (4.2 cm) surfaces. The mean electron energy calculations in the low pressure (50 Pa) results exhibit larger errors with a number of points that do not follow the overall trend. These discrepancies in the 50 Pa case could be due to cascade processes which are currently not accounted for, or as previously mentioned, the EEDFs change as a function of pressure which the current ERA analysis technique also doesn't account for. However, the observed trends provide a representation of the system behaviour, in which a level of

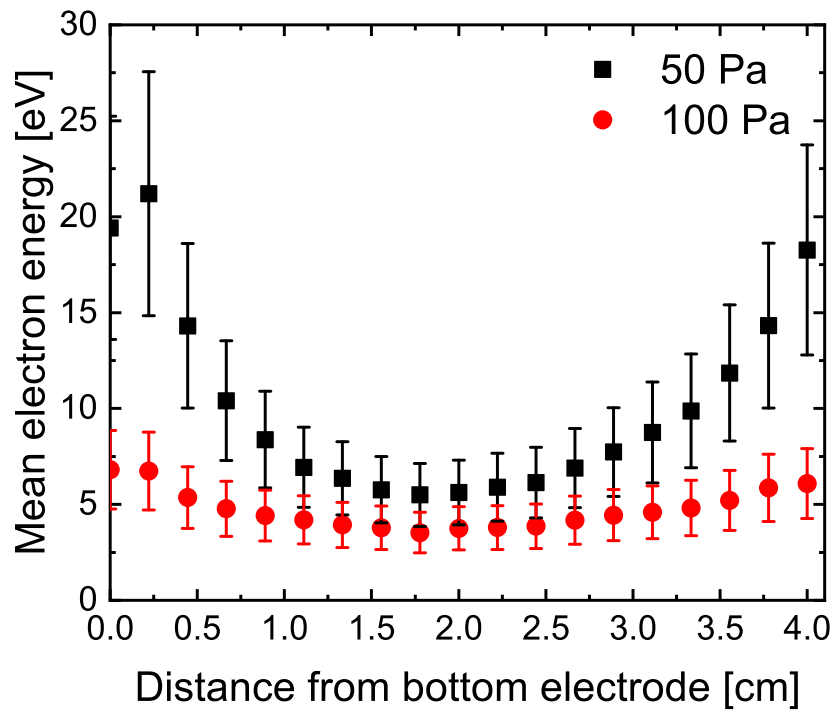


Figure 6.14: Mean electron energy plot of the inter-electrode gap for 50 and 100 Pa pressure plasmas, calculated assuming a Maxwellian EEDF. The highest electron energies are present in the sheath region due to heating from the plasma sheath and TVW. Gas mixture is O_2/Ar (98%/2%) and the plasma is operated at 200 W.

uncertainty in the absolute values is assumed.

6.4 Comparison of PiOES and TALIF

Figure 6.15 illustrates the ERA and TALIF comparative measurements at system pressures of 20 - 250 Pa and 200 W plasma power with a 350 V peak-to-peak amplitude pulse. For these measurements the ERA analysis has been carried out at a specific time and axial location, indicated by the crossing points of the dashed white lines on the PROES images shown in figure 6.12. The dissociation degree inferred from ERA is converted into a density of atomic oxygen using the ideal gas law at a temperature of 400 K, which is approximately consistent with the gas temperatures inferred from the TALIF measurements discussed earlier. This illustrates the effectiveness of the PiOES-ERA technique when directly compared with TALIF. Both measurements show increasing trends which deviate as the pressure increases starting around the 150 Pa mark.

In general, the agreement between the absolute densities and the trends of the two

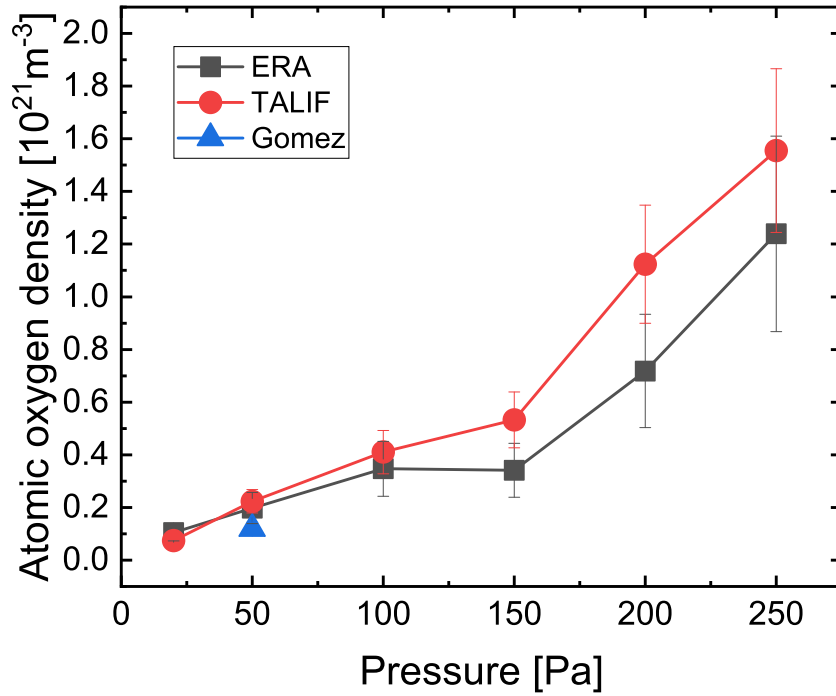


Figure 6.15: Comparison of atomic oxygen densities calculated using ERA and measured with TALIF in a 200 W O₂/Ar plasma (98%/2%) plasma, with an additional literature measurement (blue triangle) by Gomez et al at 50 Pa and 250 W in a GEC operating in an oxygen chemistry [4], showing good agreement in the capacitive plasma regime.

techniques is very good, particularly at the lower pressures. When compared with a measurement from the work of Gomez et al, an atomic density measured at 50 Pa and 250 W in a GEC reactor at the same distance from lower electrode, the atomic oxygen density ($\sim 1.1 \times 10^{20} \text{ m}^{-3}$) has very good agreement with the ERA and TALIF measurements.

Figure 6.16 shows the mean electron energies inferred from ERA for the same space and time point as the atomic oxygen densities shown in figure 6.15. Here, a clear decrease in mean electron energy with increasing pressure is observed, again consistent with the work of Tsutsumi et al [38] and Gudmundsson and Ventejou [144]. The drop in mean electron energy between 50 and 100 Pa may indicate the EEDF in the experiment is very different from the Maxwellian EEDF assumed in the simulation. The work of Gudmundsson et al discusses the evolution of the electron energy probability function (EEDF). At low pressures the population of low energy electrons is relatively small, however as the pressure is increased as per figure 6.14 the number of low energy electrons increases. The collisional heating of low energy electrons in an oxygen capacitive discharge is poor, despite the collision cross section of momentum transfer collisions being larger. As the pressure is

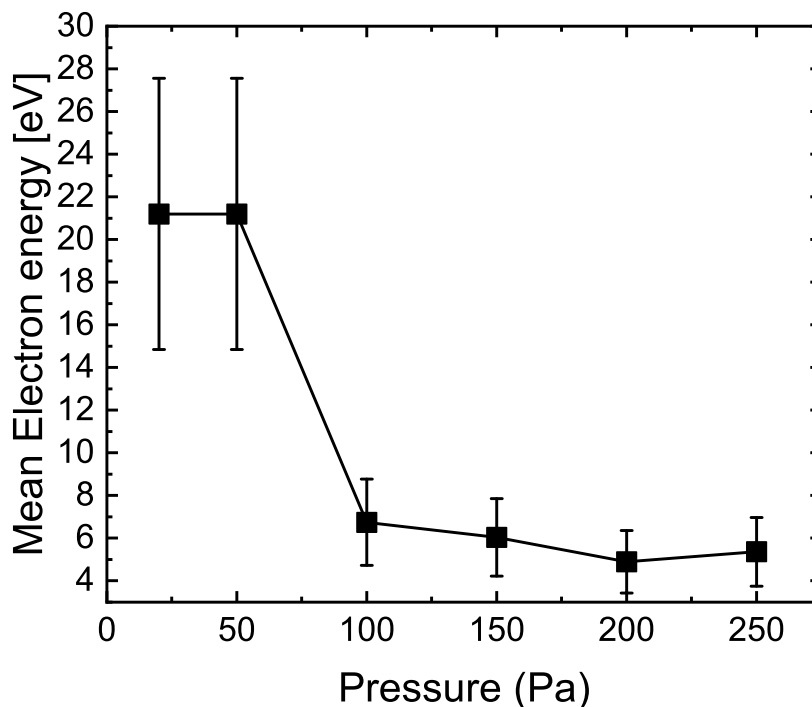


Figure 6.16: Mean electron energies calculated using ERA as a function of pressure, a decreasing trend in mean electron energy is observed over the pressure increase with possible discrepancies in the EEDF used to calculate the 20 and 50 Pa results. Gas mixture is O₂/Ar (98%/2%) and the plasma is operated at 200 W.

increased the shape of the EEDF changes and various sources demonstrate the EEPF becoming more bi-Maxwellian due to the pressure increase [144] or Kechkar et al who experimentally demonstrated the power evolution of an EEPF in pure O₂ from 30 - 600 W, in which it appears Druyvesteyn between 30 - 60 W and but develops into a bi-Maxwellian distribution. These transitions in dominant electron heating mechanisms are observed for the pressure increase in the mean electron energy but will also impact the electron density and effective lifetime [142,145]. This could also have implications for the ERA analysis at lower pressures as cascade effects from higher energy levels are not yet considered in this analysis.

6.4.1 ERA in H-mode analysis

For all the conditions included in figure 6.15 and 6.16 the plasma was operated in E-mode. When the ERA analysis was applied to plasmas operating in H-mode the experimentally measured excitation ratios could not be matched to the calculated excitation ratios. As a result, dissociation degrees and mean electron energies could not be measured in H-mode

plasmas. The fact that no match could be found between the calculated and measured ratios indicates that one or more excitation or de-excitation processes occur in H-mode that are not included in the ERA model, which accounts for only direct and dissociative electron impact excitation, radiative emission and collisional quenching. Understanding which processes are important in H-mode, but not included in the ERA model, this is an area for future work.

6.5 Effectiveness of PiOES-ERA in Oxygen

The presented PiOES-ERA technique has been used to measure oxygen dissociation degree and mean electron energy at the plasma-surface interface in a technologically relevant oxygen CCP/ICP plasma. These measurements have resulted in the calculation of atomic oxygen density and gas temperature in a region of the plasma that isn't easily assessable or permitting of external probes. The technique allows for the sensitive measurement of the dissociation degree and mean electron energy with high resolution 0 - 4 mm above the lower electrode, where measuring both quantities simultaneously in this location tracks the fundamental processes that change in an oxygen plasma due to pressure and power variations. The measured dissociation degree in figure 6.13 illustrates a dome shaped profile between the two electrodes, with a peak at both 50 and 100 Pa at the centre point (~ 2.0 cm) between the electrodes, whereas the local mean electron energy peaks at both electrodes, with a reduction in the electron energy due to a pressure increase and lower electron mobility as a result of collisions. The largest mean electron energy is observed at the lower electrode in the 50 Pa case, which could be a result of the edge effects known to occur in the GEC cell design and outlined in the HPEM model in figure 6.8. This work confirms the importance of surface recombination probabilities due to pressure and power control variations, especially with regard to the dissociation fraction at the electrode surface, with an important next step in roadmap of this technique is the automation of the in situ measurements to allow real-time measurement of the complex spatial profiles of electron heating and reactive species densities in larger scale industrial plasma reactors.

This includes developing the ERA analysis to include pure inductive mode plasmas which requires further analysis of the excitation and de-excitation schemes. The author

acknowledges that this is a major factor to ERA/actinometry being an effective analysis technique across all operating modes of the plasma. The motivation for industrial partners using the PiOES-ERA diagnostic is the benefit to developing and understanding the process control for plasma enhanced ALE and ALD processes.

In conclusion, this chapter has investigated the effectiveness of the PiOES-ERA technique in measuring the dissociation degree and mean electron energy in an oxygen plasma over a wide pressure and plasma power range. It has compared the PiOES-ERA technique with HPEM simulations and experimental TALIF measurements to verify the calculated atomic oxygen density at a region of the plasma with classically low emission. By applying a tailored voltage waveform and stimulating emission it is possible to collect enough plasma emission to calculate key atomic species densities in a novel non-invasive manner.

Results from the oxygen dissociation degree and mean electron energy measured at the plasma-surface interface in a 50 Pa oxygen plasma operated at 200 W have been measured and analysed, atomic oxygen densities of $1.97 \times 10^{20} \text{ m}^{-3}$ were calculated using the PiOES-ERA technique, TALIF under the same system and operating conditions measured a density of $2.23 \times 10^{20} \text{ m}^{-3}$ and work by Gomez et al on a similar GEC reference cell measured $1.20 \times 10^{20} \text{ m}^{-3}$. These values show good agreement with scope to extend the diagnostic further and into different systems.

The results presented in this chapter show good agreement for low power or capacitive plasmas but at high power the experimentally measured excitation ratios could not be matched to the calculated values, resulting in no H-mode dissociation degree or mean electron energy. The lack of matching values indicates that there are additional excitation or de-excitation processes that are not considered in this iteration of the ERA model.

Chapter 7

Scaling of H density with pressure and power

Applications of low pressure, high density hydrogen plasmas are widely used in materials processing, this includes plasma etching, deposition and passivation applications. More specifically; ion implantation and hydrogenation of polysilicon thin-film transistors to increase the transistor performance. The dissociation energy of molecular hydrogen is 4.52 eV and hydrogen atoms are generated via electron impact dissociation [146]. The use of high density hydrogen plasma discharges have been developed for specific passivation processes where the processing time has been reduced from hours to minutes [147].

Alternative areas of research are investigating the possibility of replacing existing wet etching of copper (Cu) that currently uses nitric acid, sulphuric acid or hydrogen peroxide. These wet etching technologies are typically used for the fabrication of printed circuit boards (PCB) with an etching rate on the order of tens of micrometers per minute. Current dry etching processes use chlorine gases as they achieve highly anisotropic etch patterns, However Wu et al has investigated the use of low temperature hydrogen plasmas to mitigate the use of hazardous gases and wet etching products with Cu [148]. Etching rates of 500 nm/min were achieved which isn't on the same scale as wet etching however for small batch or high aspect ratio structures it could add value. After discussion with industry partners, investigations on the GEC reference cell were undertaken in a range of low pressure and high power scenarios to understand the etching products left behind on a carbon wafer

post treatment. These products would be detrimental to the cleaning life cycle of the reactor. It was found that over shorter, high power (1 kW) measurements no change or deposits were observed to the quartz microscope slide placed next to the carbon wafer.

This chapter uses TALIF to look at the density of atomic hydrogen over the same power and pressure range as investigated in chapter 6 for oxygen plasmas, covering the plasma operation in both E and H mode and providing data for future development of H PiOES and model verification. The author acknowledges the preliminary nature of this chapter however feels it is relevant to the developing the roadmap of the PiOES-ERA technique. The TALIF data is an excellent benchmark for future studies.

7.1 Hydrogen atom TALIF

The laser was operated at 700 μJ due to the saturation threshold measured at 780 μJ and a laser wavelength of $\lambda = 203.53$ nm. The plasma was operated at the same parametric values as the oxygen TALIF, Pressure range from 20 to 250 Pa and power from 200 — 1000 W. The system gas mixture is set to a hydrogen/helium mix of 98%/2% with flow rates of 24.5 and 0.5 sccm.

Figure 7.1a shows the H atom density as a function of pressure and power. The excited H atom lifetime for identical system conditions is shown in figure 7.1b. The H atom density follows a similar trend to that of the atomic oxygen density, discussed in chapter 6, showing an increase with both power and pressure. The increase in H atom density is once again caused by increasing electron densities, leading to more electron impact dissociation. The increase with pressure results from having greater numbers of H_2 molecules to dissociate.

The general trends for the H atom lifetime are also similar to those for O atoms. The lifetime tends to increase with increasing power, which is likely a result of higher gas temperatures and lower gas densities, and decreases with pressure as a result of higher gas densities and increased quenching.

In the case of H atom TALIF the same method of calculating the gas temperature was attempted as in the O atom TALIF case. These calculations produced gas temperatures of lower than 300 K in many cases, and are not shown here. This issue may be caused by weaknesses in the quenching coefficient data for excited H atoms, or from state mixing

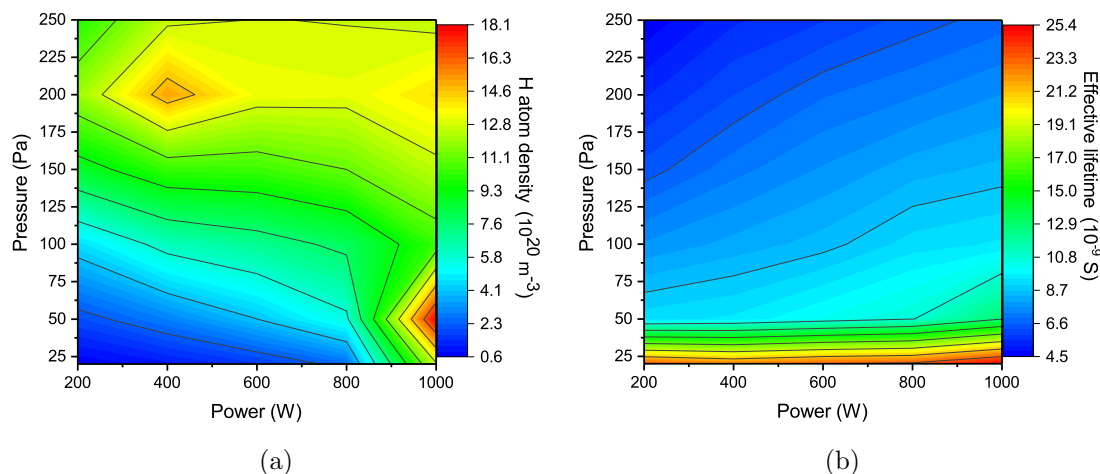


Figure 7.1: Hydrogen density plot as a function of plasma power and pressure (a) and effective lifetime (b) illustrating similar trends to the oxygen experimentation. Increasing H atom density with pressure and power as a result of increased electron impact dissociation. Effective lifetime is also increasing with power due to the higher gas temperatures and lower gas densities.

between excited H atoms. Improvement of these calculations is a topic for future work.

As the gas temperature was not calculated in this work, this could not be used to calculate the dissociation degree. To estimate the dissociation degree a gas temperature of 400 K was assumed over the entire pressure and power range, the results are shown in figure 7.2. In general, the dissociation degree increases with power, and decreases with pressure, but does not vary as much as the dissociation degree shown for atomic oxygen, except for at 20 and 50 Pa between 800 and 1000 W. These points appear to show the plasma transition between E and H mode. Compared to oxygen plasmas, the E-H transition appears to occur at higher powers in hydrogen plasmas for any given pressure.

The H density for power variation at 20 Pa in figure 7.3a the mode transition between E and H mode can be seen as a large increase in the H density between 800 and 1000 W, with a gradual density increase between 200 and 800 W. For the constant 200 W power measurement in figure 7.3b no transition is observed, an increase in the gas pressure and therefore an increase in the H density.

A number of studies examining the plasma-surface interface in low pressure hydrogen plasmas include; deposition processing of hydrogenated silicon thin films, diamond-like hydrocarbon and self-assembled carbon nanostructures [149–151]. These studies generally implement reduced pressure of power ranges due to limitations in the associated hardware

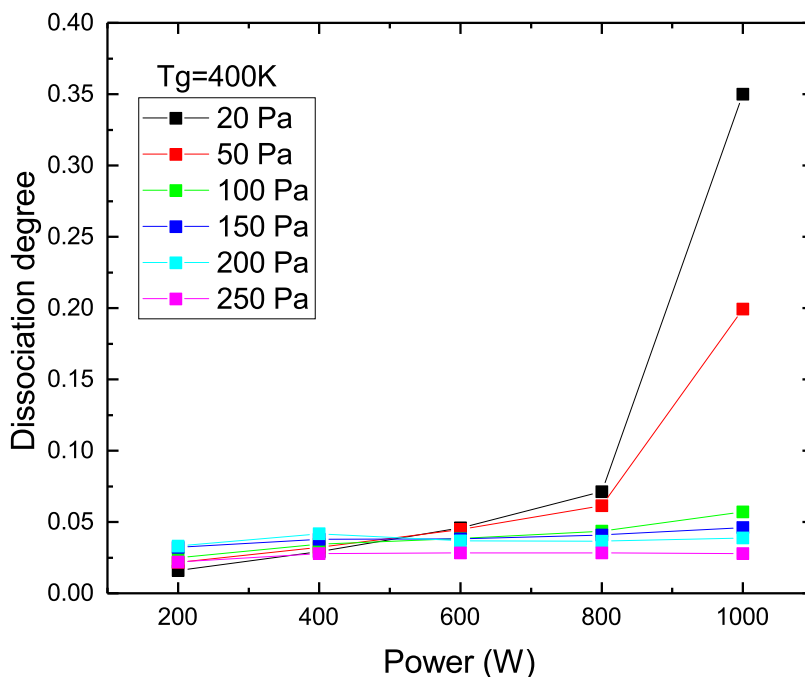


Figure 7.2: Dissociation degree at a T_{gas} value of 400 K as a function of plasma power and pressure. The higher pressure (100 - 250 Pa) results stay fairly linear while 20 and 50 Pa demonstrate much larger dissociation degree increases.

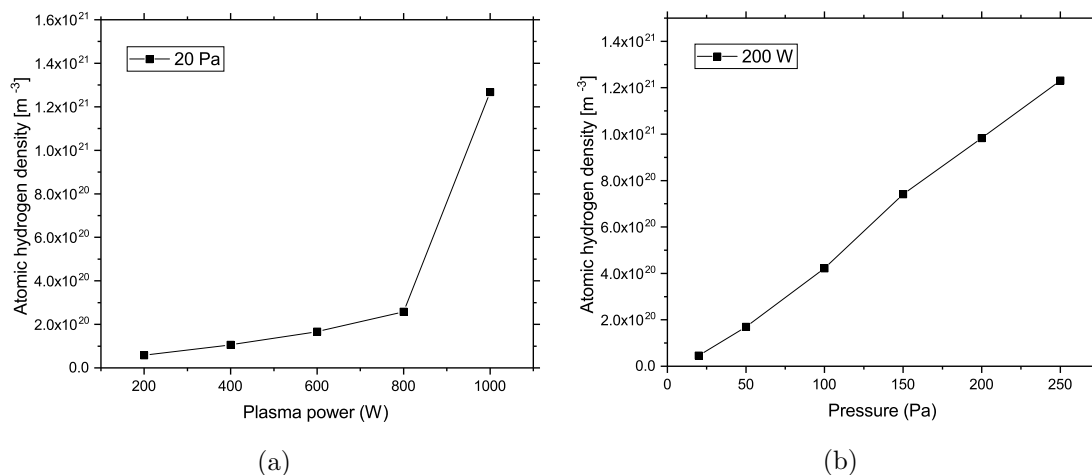


Figure 7.3: Atomic hydrogen density plots of pressure (20 Pa) plot (a) and plasma power (200 W) plot (b) highlighting a much later E-H mode transition between 800 - 1000 W at low pressures. While the constant power case only increases gradually with no steps or jumps.

or specific plasma surface interaction conditions, with typical plasma powers between 0 - 500 W and pressures up to 100 Pa [152]. This chapter is intended to provide results for a significant power and pressure range study in order to meet different plasma conditions for current and future applications using low pressure hydrogen plasmas.

In conclusion, an increasing trend of atomic hydrogen density is seen in both pressure and power measurements, these can be tailored to etching or deposition processes depending on the flux or energy of the radical produced. Different H atom density values are observed for the E-H mode transitions, these can only be seen in the lower pressure cases i.e. 20 and 50 Pa. This warrants further investigation to assess where the transition modes occur and how this impacts the plasma density. These results provide a baseline for future HPEM simulations and further material testing to produce a non-invasive technique for monitoring hydrogen containing low pressure plasmas. It also highlights the need for further work in measuring hydrogen quenching coefficients, in order to obtain accurate gas temperature measurements and calculate dissociation degrees. By utilising a platform such as the GEC reference cell it is possible to continue this work under the same operational conditions at any location using the TALIF data as a benchmark.

Chapter 8

Conclusion

In conclusion, the work presented in this research validates a new method for producing and analysing plasma emission by tailoring a voltage waveform and creating sufficient optical emission spectroscopy to extract dissociation degrees and mean electron energies. The focus being to generate enough emission in a region of the ICP plasma doesn't ordinarily benefit from high levels of emission. In order to achieve this, both the experimental method and analytical technique required additional tailoring.

Chapters 1 - 4 introduces theory, computational and experimental techniques as well as expanding on the actinometry theory, it outlines the TALIF and HPEM configuration used in the results chapters. The focus of this research is using an advanced actinometry technique as the analysis platform and generating plasma emission in a region of interest inside the GEC reference cell, therefore allowing atomic species densities to be calculated in an otherwise unachievable region of the plasma, this required a tailored approach to creating a non-invasive voltage waveform to induce sufficient plasma emission.

Chapter 5 introduces the initial and developed methods for producing and tailoring a voltage waveform at the lower electrode and in a region of interest for a number of manufacturing processes, this is due to high radical densities, high selectivity and anisotropic etch profiles at low temperatures and mild voltages. Understanding this interface helps to prevent unwanted degradation of materials due to factors surrounding heat and lattice damage from ion bombardment. By designing and tailoring the voltage waveform around the implementation of harmonics, it has been possible to reduce the rise time and full

width half maximum of the pulse to a degree where its impact on the electron and ion plasma properties is minimal. The initial tailored voltage waveform was generated using a 40 MHz TTI arbitrary waveform generator where the shortest FWHM value of 50 ns was achieved, this was deemed unacceptable due to its highly variable impact on ion energies 20 - 32 eV and lack of resolution when configuring the phase over a single RF cycle (74 ns). The developed voltage was generated using a 120 MHz Keysight 33622A waveform generator capable of ≥ 3 ns pulse rise times and pulse widths of ≥ 8 ns, here the ion energies varied less than 5 eV per measurement block, in comparison to 12 eV previously. Between the initial and developed TVW design, the ion energy variation is reduced from 0 - 12 eV (initial TVW design) across a single RF phase measurement down to 0 - 5 eV for the developed tailored waveform. The variation in phase and polarity was reduced for the developed TVW design with only minor ion energy changes 17 (± 3) eV between the phases and polarity which suggests the modified design is less impactful on the ion energies and therefore more applicable to plasma assisted ALD processes, none of the ion energy measurements using the modified approach exceeded 35 eV. Where plasma assisted ALDs that have upper and lower ion energy limits e.g (19 - 27 eV), the developed design will conform to much tighter ion energy constraints.

Furthermore, measurements in chapter 5 looking at the ion energy distribution function at the plasma-surface interface, highlighted the impact of varying the TVW's voltage, polarity and repetition, by reducing the pulse width it reduced the impact on the ion properties due to the fast change in applied voltage. The negative polarity pulse was found to accelerate the electrons away from the lower electrode and influenced the sheath expansion during operation, this is beneficial and a novel approach to achieving emission across the axial region of the plasma, while a positive pulse attracted electrons to the electrode surface and focussed the analysis at the electrode surface.

Chapter 6 implemented the negative polarity TVW design in an oxygen plasma, the PiOES-ERA experimentation and analysis procedure was formalised and compared with HPEM simulations and TALIF measurements under the same plasma conditions. The PiOES measurements at 50 and 100 Pa allow sufficient pulse emission to span the whole axial distance of the discharge region. Allowing ERA to extract the dissociation degree and mean electron energy. The profiles exhibit higher dissociation degrees at the centre which

decay towards the surfaces, this is due to the dominant loss mechanisms of atomic oxygen occurring due to surface recombination. Whereas, the mean electron energies are highest at the sheath regions due to heating of the electrons from the movement of the plasma sheath. An increase in gas pressure also increases the collision frequency with the background gas resulting in lower mean electron energies. Surface losses under these conditions play an important role in the density of atomic O, at higher gas temperatures the diffusion of O to the surface is faster, leading to increased surface losses. Gas temperature measurements in chapter 6 spanned 300 - 2800K, with upward trends that followed increased pressure and power input, these showed good agreement with the work of Foucher at low system pressures. The PiOES-ERA technique has been used to measure oxygen dissociation degree and mean electron energy at the plasma surface interface in a 50 Pa oxygen plasma operated at 200 W, this has resulted in atomic oxygen densities of $1.97 \times 10^{20} \text{m}^{-3}$ from the PiOES-ERA technique, TALIF in the same system with identical operating conditions at $2.23 \times 10^{20} \text{m}^{-3}$ and work by Gomez et al on a similar GEC reference cell of $1.20 \times 10^{20} \text{m}^{-3}$. These values show good agreement with scope to extend the diagnostic further and into different systems. For the H-mode measurements the experimentally measured excitation ratios could not be matched to the calculated values, resulting in no H-mode dissociation degree or mean electron energy. The lack of matching values indicates that there are additional excitation or de-excitation processes that are not considered in the ERA model. By further analysing extreme cases in the H-mode it may be possible to quantify the impact of cascade and metastable processes contributing to the direct and dissociative electron impact processes.

A positive polarity pulse accelerates the electrons towards the surface of the electrode, creating a more defined emission structure at the substrate. This could overcome one of the limitations of plasma assisted ALD which affects the conformity or step coverage achieved in non-planar substrates. To overcome this and achieve conformal deposition, plasma conditions need to be surface recombination limited, so by taking PiOES data and examining the local mean electron energy and dissociation degree from the plasma bulk to the wafer surface it would be possible to find a regime where the plasma assisted ALD either reduces its power or increases the pressure to find the optimal species density and flux range.

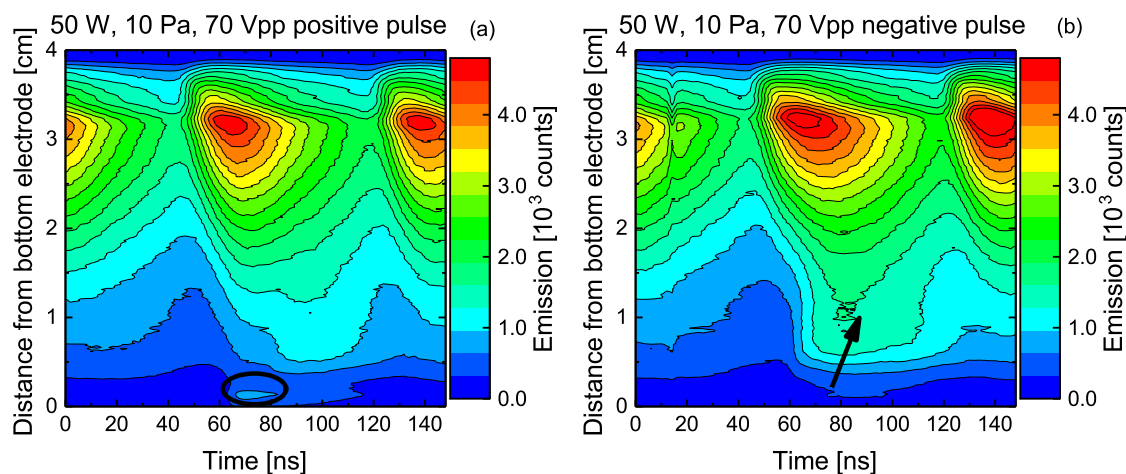


Figure 8.1: Plot (a) TVW design that focuses excitation and emission at the plasma-surface interface, while (b) tailors a waveform that allows axial measurements between the electrodes.

In chapter 7 general the hydrogen atom density and lifetime are similar to those for O atoms in chapter 6. For the H atom density an increase in power causes an increase in electron density which leads to more electron impact dissociation. The lifetime also increases with higher plasma power, which is a result of higher gas temperatures and lower gas densities as previously observed for the O effective lifetime. This chapter is the start of the roadmap into evaluation of other gases and systems using the PiOES-ERA technique. These results highlight the need for further work in measuring hydrogen quenching coefficients in order to obtain accurate gas temperature measurements and calculate dissociation degrees.

The next phase of testing for future applications would include attaching the PiOES-ERA technique to a larger scale processing plasma, to confirm the process resolution and integration into a manufacturing life-cycle. This would require a TVW calibration phase, however the process for testing voltage, phase and polarity are set out in this document.

Appendices

Appendix A

List of publications and conference attendances

Publications directly related to this work;

- **M. P. Blake**, A. R. Gibson, A. Greb, K. Niemi, J. Ellis, D. O’Connell, T. Gans
”*Pulse induced optical emission spectroscopy: a novel diagnostic technique for the plasma surface interaction region in low temperature plasmas*” in preparation
- **M. P. Blake**, A. R. Gibson, J. Bredin, K. Niemi, D. O’Connell, T. Gans ”*Atomic oxygen density and gas temperature scaling with power and pressure in a low pressure capacitive/inductive plasma*” in preparation
- **M. P. Blake**, A. R. Gibson, J. Bredin, S. Schroeter, K. Niemi, D. O’Connell, T. Gans ”*Atomic hydrogen density scaling with power and pressure in a low pressure capacitive/inductive plasma*” in preparation

Conference presentations;

- *Neutral and ion dynamics in inductively coupled plasmas*
69th Annual Gaseous Electronics Conference (GEC)
Bochum, Germany, Oct. 2016

- *Plasma Dynamics at the Surface Interface in Low Pressure Capacitively and Inductively Coupled Plasmas*

63rd AVS International Symposium and Exhibition

Nashville, Tennessee, Nov. 2016

Appendix B

Industrial relevance

The plasma processing industry takes advantage of the unique properties of high density plasmas for etching and deposition applications within integrated circuit (IC) fabrication. By utilising the charged particles to a high precision the industry aims to scale down these dimensions, however an important condition for wafer to wafer repeatability is an understanding of any changes to the wall conditions [153]. This has been identified as a large and uncontrolled cause of process drift, and can influence the etching rates and sensitively greatly [154]. Changes in the reactor wall conditions often occur after multiple etch cycles, and consist of any etch product generated during production. As the inner reactor surface is modified this changes the surface loss or production probability of species in the plasma.

This chapter investigates the processed carbon products that leave a wafer surface during treatment and end up on the quartz glass cylinder. By applying SEM and EDX techniques to better understand how these products behave and react with the plasma.

B.1 Experimental setup

The ICP plasma discharge chamber was modified slightly by incorporating a glass cylinder to enclose the main plasma producing region and reduce the accumulation of carbon products on the outer reactor walls. A microscope glass slide was attached to the inner side of the glass cylinder with Kapton tape to analyse any debris left behind by the sample during treatment.

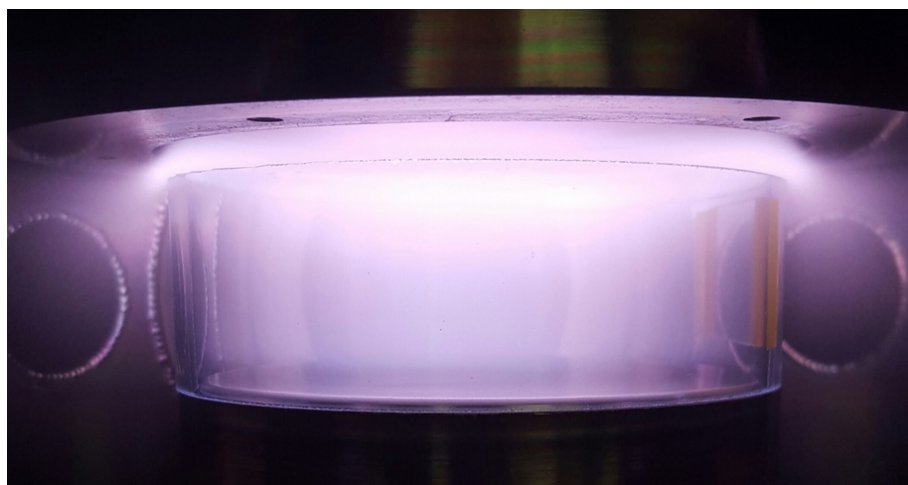


Figure B.1: Plasma discharge region with quartz glass cylinder placed on the lower electrode, operated at 1000 W and 250 Pa

The plasma configuration was identical to previous measurements, except the introduction of the carbon wafer and quartz glass cylinder. The GEC was operated in a helium/hydrogen gas mixture at 6/1 ratio. An issue with high gas heating at 1000 W and 250 Pa resulted in the Kapton tape drying out and no longer holding the glass slide in place. Small carbon wafers (25×25 mm) were placed on the lower electrode and positioned next to the microscope slides so that the etching product from the carbon wafer would settle on it.

The carbon wafer was plasma treated 6 times, each treatment lasted 180 seconds, the system was allowed to cool for a further 180 seconds between each of the runs.

B.2 PiOES analysis

For the measurement and treatment of the carbon, PROES images of the system were taken at the H_α (3-2) transition which has a fluorescence wavelength of 656 nm. The aim was to monitor and observe any potential changes to the plasma during the process, while also understanding how PiOES can be used under industrially relevant conditions, where the lower electrode is covered by a wafer.

Figure B.2 focuses in the PROES across the whole plasma (a), and just above the electrode (b). The scale is saturated in part (a) due to the strong emission from the H-mode plasma close to the coil. Despite the strong emission from the plasma, pulse

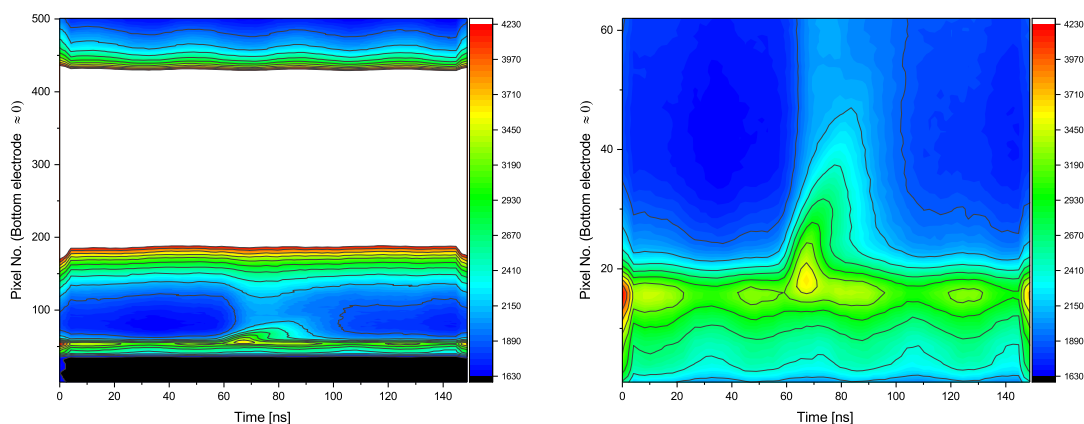


Figure B.2: 1000 W 6/1 He/H₂ plasma at 250 Pa with 400 V_{pp}, negative polarity pulse applied.

induced emission is visible at around 70 ns at the bottom electrode. In this case, the pulse used is a negative polarity pulse with 400 V_{pp}. Part (b) shows the pulse induced emission more clearly. This preliminary result follows on from those obtained in an E-mode oxygen plasma in chapter 5, to show that PiOES may be applicable in high power hydrogen plasmas as well. However, this will require more development to fully assess the compatibility of PiOES under these conditions.

B.3 Surface analysis

To better understand the carbon wafer and glass microscope slide composition before and after treatment with a helium/hydrogen/argon plasma. The samples will be placed in a Scanning Electron Microscope (SEM) and Energy Dispersive X-ray spectroscopy (EDX) both techniques provide information on the samples morphology and surface composition.

B.3.1 SEM

The Scanning Electron Microscope (SEM) is used as a diagnostic technique in which to study the topology and composition of a sample by focussing a beam of electrons on to it and monitoring the back scattered and secondary electrons produced via the surface interaction. The SEM device (JEOL JSM7800F) uses a series of lenses and an electron source to control a path of electrons. As the incident electron beam enters the sample, it typically produces either secondary electron emission from the valence electrons of the

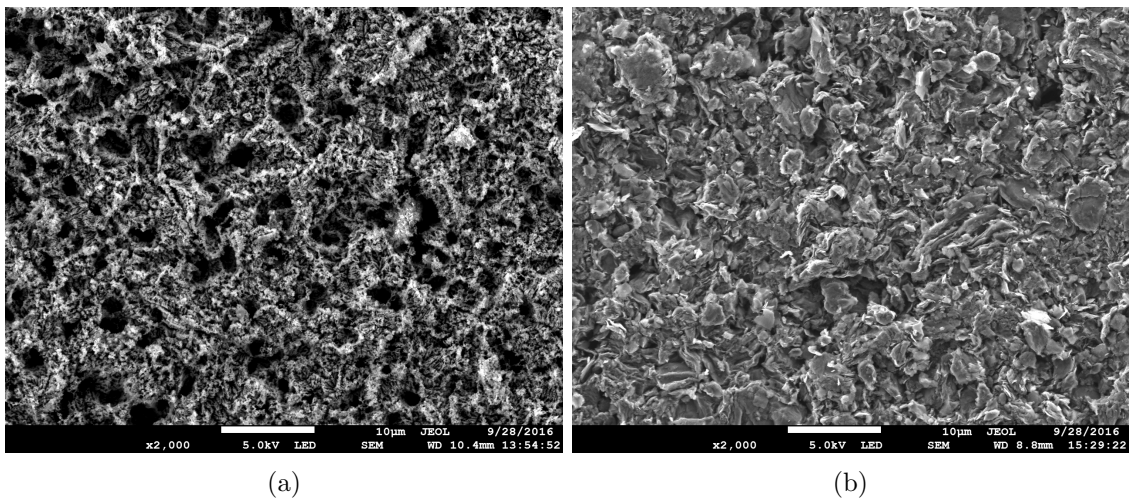


Figure B.3: far field amplification figure (a) is a 1 kw 250 Pa ICP plasma treated carbon sample, whereas (b) is an untreated sample

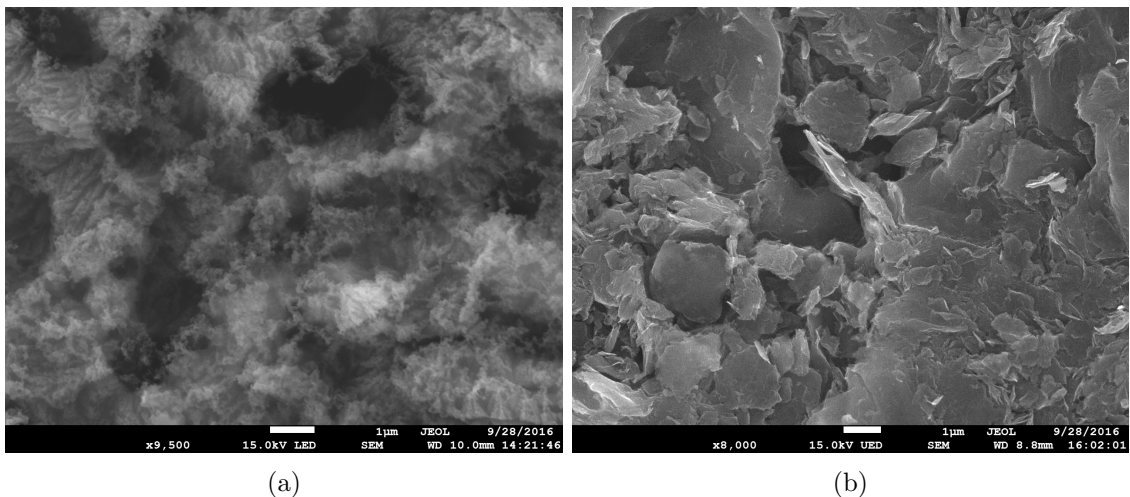


Figure B.4: Mid range magnification figure (a) is a 1 kw 250 Pa ICP plasma treated carbon sample, whereas (b) is an untreated sample.

atoms in the specimen. These are limited to 50 eV while and accounts for a large proportion of the detected signal. Or backscattered electrons which range in energy from the upper limit of secondary electron emission to the incident electron energy. These are sensitive to the composition of the sample, while secondary electrons provide information of the topology of the sample.

Figure B.3 is the carbon wafer post (a) and pre (b) treatment. The sample was treated for a total of 1080 seconds, what can be observed is that the surface has been significantly altered, producing a less uniform and more pitted appearance. A combination of heat from the plasma and reactive chemistry has fundamentally changed its appearance.

With a higher magnification the SEM images in figure B.4 show a clearer image of the surface modification and apparent etching, as it has changed in appearance and structure. The glass samples could not be analysed using SEM due to their lack of conductivity and subsequent surface charging, which meant very little secondary electron emission was detected. However the energy dispersive x-ray spectroscopy was able to resolve the samples and produce elemental surface composition.

B.3.2 EDX

Energy Dispersive X-ray spectroscopy is a technique that sits alongside the SEM configuration but uses increased electron beam energy (5-15 kV) to penetrate further into the sample, where the x-ray fluorescence is resolved in photon energy. Creating unique elemental peaks on the electromagnetic emission spectrum. This allows you to identify the contributing elements through their characteristic radiation.

These results represent a short treatment time of 1080 s in a 250 Pa helium/hydrogen plasma, with one set of measurements also including argon. The main carrier gas is Helium, but to consider using argon as an actinometer gas for ERA there needs to be confirmation it isn't affecting the plasma chemistry and potential etch rate.

Table B.1 is the EDX structure ratio of an untreated quartz microscope slide. The main elemental peaks observed in this analysis were O, Si and C.

	Untreated Quartz	
	Percentage (%)	Error (%)
O	68.0	3.5
Si	22.9	1.5
C	8.0	0.5

Table B.1: Untreated quartz surface composition

Table B.2 is a comparison of plasma with and without argon admixture, the error was calculated on the mean of three measurements taken in a similar area of the quartz microscope slide. This data represents a small variation between a plasma with argon at 0.5 sccm or a ratio of 6/1/0.167 He/H₂/Ar and one without.

The post treatment analysis shows a surface which is closer to SiO₂ as there is a factor of two more O than Si, which suggests a normal composition of quartz. One conclusion is that

	Helium/Hydrogen		Helium/Hydrogen/Argon	
	Percentage (%)	Error (%)	Percentage (%)	Error (%)
O	62.7	2.5	62.8	3.9
Si	30.7	0.6	29.5	0.9
C	5.2	0.1	7.1	0.2

Table B.2: Quartz surface composition, post plasma treatment with either an He/H₂ or He/H₂/Ar plasma

the oxygen plasma has cleaned a previously dirty quartz microscope slide. Further analysis of table B.2 shows a reduction in the amount of C on the surface when compared with the untreated data in table B.1. For these treatment time scales and plasma conditions no additional carbon from the wafer is deposited on the microscope slide. Which was one of the initial tasks for these plasma conditions and revised internal GEC cell configuration.

List of References

- [1] N. Sadeghi, D. W. Setser, A. Francis, U. Czarnetzki, and H. F. Döbele. Quenching rate constants for reactions of Ar($4p'[1/2]_0, 4p[1/2]_0, 4p[3/2]_2$, and $4p[5/2]_2$) atoms with 22 reagent gases. *The Journal of Chemical Physics*, 115(7):3144, 2001.
- [2] K. Niemi, V. S. von der Gathen, and H. F. Döbele. Absolute atomic oxygen density measurements by two-photon absorption laser-induced fluorescence spectroscopy in an rf-excited atmospheric pressure plasma jet. *Plasma Sources Science and Technology*, 14(2):375, 2005.
- [3] P. J. Dagdigian, B. E. Forch, and A. W. Miziolek. Collisional transfer between and quenching of the $3p\ 3p$ and $5p$ states of the oxygen atom. *Chemical Physics Letters*, 148(4):299, 1988.
- [4] S. Gomez, P. G. Steen, and W. G. Graham. Atomic oxygen surface loss coefficient measurements in a capacitive/inductive radio-frequency plasma. *Applied Physics Letters*, 81(1):19, 2002.
- [5] I. Adamovich, et al. The 2017 plasma roadmap: Low temperature plasma science and technology. *Journal of Physics D: Applied Physics*, 50(32):323001, 2017.
- [6] S. A. Lynn, N. MacGearailt, and J. V. Ringwood. Real-time virtual metrology and control for plasma etch. *Journal of Process Control*, 22(4):666, 2012.
- [7] G. G. Gifford. Applications of optical emission spectroscopy in plasma in manufacturing systems. *Advanced Techniques for integrated Circuit Processing*, 1392, 1990.
- [8] Intel. Private discussion, 2014.
- [9] H. E. Litvak. End point control via optical emission spectroscopy. *Journal of Vacuum Science & Technology B: Microelectronics and Nanometer Structures Processing, Measurement, and Phenomena*, 14(1):516, 1996.
- [10] B. Keville, C. Gaman, Y. Zhang, A. M. Holohan, M. M. Turner, and S. Daniels. Attenuation of wall disturbances in an electron cyclotron resonance oxygen argon plasma using real time control. *Journal of Vacuum Science & Technology A*, 32(4):041301, 2014.
- [11] R. Yang and R. Chen. Real-time plasma process condition sensing and abnormal process detection. *Sensors*, 10(6):5703, 2010.
- [12] V. M. Donnelly and A. Kornblit. Plasma etching: Yesterday, today, and tomorrow. *Journal of Vacuum Science & Technology A: Vacuum, Surfaces, and Films*, 31(5):050825, 2013.

- [13] G. S. Oehrlein, D. Metzler, and C. Li. Atomic layer etching at the tipping point: An overview. *ECS Journal of Solid State Science and Technology*, 4(6):N5041, 2015.
- [14] A. J. L. Michael A. Lieberman. *Principles of Plasma Discharges and Materials Processing, 2nd Edition*. Wiley, 2nd edition, 2005.
- [15] E. A. Douglas, J. Stevens, K. Fishgrab, C. Ford, R. J. Shul, and S. J. Pearton. Low-pressure inductively coupled plasma etching of benzocyclobutene with sf6/o2 plasma chemistry. *Journal of Vacuum Science & Technology B, Nanotechnology and Microelectronics: Materials, Processing, Measurement, and Phenomena*, 30(6):06FF06, 2012.
- [16] K. H. Lee, H. W. Jang, K.-B. Kim, Y.-H. Tak, and J.-L. Lee. Mechanism for the increase of indium-tin-oxide work function by o2 inductively coupled plasma treatment. *Journal of Applied Physics*, 95(2):586, 2004.
- [17] F. F. Chen. *Introduction to Plasma Physics and Controlled Fusion*. Springer International Publishing, 3rd edition, 2016.
- [18] J. Hopwood. Review of inductively coupled plasmas for plasma processing. *Plasma Sources Science and Technology*, 1(2):109, 1992.
- [19] V. A. Godyak, R. B. Piejak, and B. M. Alexandrovich. Electron energy distribution function measurements and plasma parameters in inductively coupled argon plasma. *Plasma Sources Science and Technology*, 11(4):525, 2002.
- [20] P. J. Hargis, et al. The gaseous electronics conference radio-frequency reference cell: A defined parallel-plate radio-frequency system for experimental and theoretical studies of plasma-processing discharges. *Review of Scientific Instruments*, 65(1):140, 1994.
- [21] J. W. Denneman. Determination of electromagnetic properties of low-pressure electrodeless inductive discharges. *Journal of Physics D: Applied Physics*, 23(3):293, 1990.
- [22] T. Wegner, C. Küllig, and J. Meichsner. On the e-h transition in inductively coupled radio frequency oxygen plasmas: I. density and temperature of electrons, ground state and singlet metastable molecular oxygen. *Plasma Sources Science and Technology*, 26(2):025006, 2017.
- [23] V. A. Godyak, R. B. Piejak, B. M. Alexandrovich, and V. I. Kolobov. Experimental evidence of collisionless power absorption in inductively coupled plasmas. *Phys. Rev. Lett.*, 80:3264, 1998.
- [24] J. Schulze, E. Schangel, Z. Donka, D. Luggenhalscher, and U. Czarnetzki. Phase resolved optical emission spectroscopy: a non-intrusive diagnostic to study electron dynamics in capacitive radio frequency discharges. *Journal of Physics D: Applied Physics*, 43(12):124016, 2010.
- [25] K. Dittmann, K. Matyash, S. Nemschokmichal, J. Meichsner, and R. Schneider. Excitation mechanisms and sheath dynamics in capacitively coupled radio-frequency oxygen plasmas. *Contributions to Plasma Physics*, 50(10):942, 2010.

- [26] T. Wegner, C. Küllig, and J. Meichsner. Electron heating during e-h transition in inductively coupled rf plasmas. *Plasma Sources Science and Technology*, 24(4):044001, 2015.
- [27] C. S. Corr, S. Gomez, and W. G. Graham. Discharge kinetics of inductively coupled oxygen plasmas: experiment and model. *Plasma Sources Science and Technology*, 21(5):055024, 2012.
- [28] K. U. Riemann. The bohm criterion and sheath formation. *Journal of Physics D: Applied Physics*, 24(4):493, 1991.
- [29] A. Agarwal and M. J. Kushner. Seasoning of plasma etching reactors: Ion energy distributions to walls and real-time and run-to-run control strategies. *Journal of Vacuum Science & Technology A: Vacuum, Surfaces, and Films*, 26(3):498, 2008.
- [30] J. R. Woodworth, I. C. Abraham, M. E. Riley, P. A. Miller, T. W. Hamilton, B. P. Aragon, R. J. Shul, and C. G. Willison. Ion energy distributions at rf-biased wafer surfaces. *Journal of Vacuum Science & Technology A: Vacuum, Surfaces, and Films*, 20(3):873, 2002.
- [31] S. Rauf. Effect of bias voltage waveform on ion energy distribution. *Journal of Applied Physics*, 87(11):7647, 2000.
- [32] T. Mussenbrock. Modeling and simulation of ion energy distribution functions in technological plasmas. *Contributions to Plasma Physics*, 52(7):571, 2012.
- [33] T. E. Sheridan and J. Goree. Collisional plasma sheath model. *Physics of Fluids B: Plasma Physics*, 3(10):2796, 1991.
- [34] D.-Q. Wen, Y.-R. Zhang, M. A. Lieberman, and Y.-N. Wang. Ion energy and angular distribution in biased inductively coupled ar/o2 discharges by using a hybrid model. *Plasma Processes and Polymers*, 14(4-5):1600100, 2017.
- [35] M. D. Logue, H. Shin, W. Zhu, L. Xu, V. M. Donnelly, D. J. Economou, and M. J. Kushner. Ion energy distributions in inductively coupled plasmas having a biased boundary electrode. *Plasma Sources Science and Technology*, 21(6):065009, 2012.
- [36] P. A. Miller, G. A. Gerardo, K. E. Greenberg, P. D. Pochan, and B. P. Aragon. An inductively coupled plasma source for the gaseous electronics conference rf reference cell. *J. Res. Natl. Inst. Stand. Technol.*, 100(427), (1995).
- [37] J. Olthoff and K. Greenberg. The gaseous electronics conference rf reference cell - an introduction. *National Institute of Standards and Technology*, 100(327), 1995.
- [38] T. Tsutsumi, A. Greb, A. R. Gibson, M. Hori, D. O'Connell, and T. Gans. Investigation of the radially resolved oxygen dissociation degree and local mean electron energy in oxygen plasmas in contact with different surface materials. *Journal of Applied Physics*, 121(14):143301, 2017.
- [39] M. Tadokoro, A. Itoh, N. Nakano, Z. L. Petrovic, and T. Makabe. Diagnostics of an inductively coupled plasma in oxygen. *IEEE Transactions on Plasma Science*, 26(6):1724, 1998.

- [40] G. Hebner, P. Miller, and J. Woodworth. *Overview of Plasma Diagnostic Techniques*. Springer, Berlin, Heidelberg, handbook of advanced plasma processing techniques edition, 2000.
- [41] I. H. Hutchinson. *Principles of Plasma Diagnostics*. Cambridge University Press, 2nd edition, 2002.
- [42] S. Siepa, S. Danko, T. V. Tsankov, T. Mussenbrock, and U. Czarnetzki. On the oes line-ratio technique in argon and argon-containing plasmas. *Journal of Physics D: Applied Physics*, 47(44):445201, 2014.
- [43] T. Gans, V. Schulz-von der Gathen, and H. F. Döbele. Prospects of phase resolved optical emission spectroscopy as a powerful diagnostic tool for rf-discharges. *Contributions to Plasma Physics*, 44(5-6):523, 2004.
- [44] T. Gans, D. O'Connell, V. S. von der Gathen, and J. Waskoenig. The challenge of revealing and tailoring the dynamics of radio-frequency plasmas. *Plasma Sources Science and Technology*, 19(3):034010, 2010.
- [45] A. Hibbert, E. Biemont, M. Godefroid, and N. Vaeck. E1 transitions of astrophysical interest in neutral oxygen. *Journal of Physics B: Atomic, Molecular and Optical Physics*, 24(18):3943, 1991.
- [46] J. W. Coburn and M. Chen. Optical emission spectroscopy of reactive plasmas: A method for correlating emission intensities to reactive particle density. *Journal of Applied Physics*, 51(6):3134, 1980.
- [47] J. Conway, S. Kechkar, N. O. Connor, C. Gaman, M. M. Turner, and S. Daniels. Use of particle in cell simulations to improve the actinometry technique for determination of absolute atomic oxygen density. *Plasma Sources Science and Technology*, 22(4):045004, 2013.
- [48] M. B. Schulman, F. A. Sharpton, S. Chung, C. C. Lin, and L. W. Anderson. Emission from oxygen atoms produced by electron-impact dissociative excitation of oxygen molecules. *Phys. Rev. A*, 32:2100, 1985.
- [49] M. Abdel-Rahman, V. S. von der Gathen, T. Gans, K. Niemi, and H. F. Döbele. Determination of the degree of dissociation in an inductively coupled hydrogen plasma using optical emission spectroscopy and laser diagnostics. *Plasma Sources Science and Technology*, 15(4):620, 2006.
- [50] A. Greb, K. Niemi, D. O'Connell, and T. Gans. Energy resolved actinometry for simultaneous measurement of atomic oxygen densities and local mean electron energies in radio-frequency driven plasmas. *Applied Physics Letters*, 105(23):234105, 2014.
- [51] J. E. Chilton, J. B. Boffard, R. S. Schappe, and C. C. Lin. Measurement of electron-impact excitation into the $3p^54p$ levels of argon using fourier-transform spectroscopy. *Phys. Rev. A*, 57:267, 1998.
- [52] R. R. Laher and F. R. Gilmore. Updated excitation and ionization cross sections for electron impact on atomic oxygen. *Journal of Physical and Chemical Reference Data*, 19(1):277, 1990.

- [53] W. K. Bischel, B. E. Perry, and D. R. Crosley. Two-photon laser-induced fluorescence in oxygen and nitrogen atoms. *Chemical Physics Letters*, 82(1):85, 1981.
- [54] J.-P. Booth, D. Marinov, M. Foucher, O. Guaitella, D. Bresteau, L. Cabaret, and C. Drag. Gas temperature measurements in oxygen plasmas by high-resolution two-photon absorption laser-induced fluorescence. *Journal of Instrumentation*, 10(11):C11003, 2015.
- [55] A. F. H. van Gessel, S. C. van Grootel, and P. J. Bruggeman. Atomic oxygen talif measurements in an atmospheric-pressure microwave plasma jet with in situ xenon calibration. *Plasma Sources Science and Technology*, 22(5):055010, 2013.
- [56] N. Knake, K. Niemi, S. Reuter, V. Schulz-von der Gathen, and J. Winter. Absolute atomic oxygen density profiles in the discharge core of a microscale atmospheric pressure plasma jet. *Applied Physics Letters*, 93(13):131503, 2008.
- [57] S. Reuter, J. Winter, A. Schmidt-Bleker, D. Schroeder, H. Lange, N. Knake, V. S. von der Gathen, and K.-D. Weltmann. Atomic oxygen in a cold argon plasma jet: Talif spectroscopy in ambient air with modelling and measurements of ambient species diffusion. *Plasma Sources Science and Technology*, 21(2):024005, 2012.
- [58] A. Goehlich, T. Kawetzki, and H. F. Döbele. On absolute calibration with xenon of laser diagnostic methods based on two-photon absorption. *The Journal of Chemical Physics*, 108(22):9362, 1998.
- [59] N. Knake, S. Reuter, K. Niemi, V. S. von der Gathen, and J. Winter. Absolute atomic oxygen density distributions in the effluent of a microscale atmospheric pressure plasma jet. *Journal of Physics D: Applied Physics*, 41(19):194006, 2008.
- [60] K. Niemi, V. S. von der Gathen, and H. F. Döbele. Absolute calibration of atomic density measurements by laser-induced fluorescence spectroscopy with two-photon excitation. *Journal of Physics D: Applied Physics*, 34(15):2330, 2001.
- [61] R. Loudon. *The quantum theory of light*. Oxford university press, 3rd edition, 2000.
- [62] M. Payne, C. Chen, G. Hurst, and G. Foltz. Applications of resonance ionization spectroscopy in atomic and molecular physics. *Advances in atomic and molecular physics*, 17:229, 1981.
- [63] K. Tonokura, N. Shafer, Y. Matsumi, and M. Kawasaki. Photodissociation of oxygen molecules at 226 nm in the herzberg i system. *The Journal of Chemical Physics*, 95(5):3394, 1991.
- [64] V. Hasson and R. W. Nicholls. Absolute spectral absorption measurements on molecular oxygen from 2640-1920 aa. ii. continuum measurements 2430-1920 aa. *Journal of Physics B: Atomic and Molecular Physics*, 4(12):1789, 1971.
- [65] S. N. Dixit, D. A. Levin, and B. V. McKoy. Resonant enhanced multiphoton ionization studies in atomic oxygen. *Phys. Rev. A*, 37:4220, 1988.
- [66] H. F. Döbele, T. Mosbach, K. Niemi, and V. S. von der Gathen. Laser-induced fluorescence measurements of absolute atomic densities: concepts and limitations. *Plasma Sources Science and Technology*, 14(2):S31, 2005.

- [67] D. W. Setser. *Reactive intermediates in the gas phase: Generation and monitoring*. New York: Academic Press., 1979.
- [68] D. B. Graves and M. J. Kushner. Influence of modeling and simulation on the maturation of plasma technology: Feature evolution and reactor design. *Journal of Vacuum Science & Technology A: Vacuum, Surfaces, and Films*, 21(5):S152, 2003.
- [69] M. J. Kushner. Hybrid modelling of low temperature plasmas for fundamental investigations and equipment design. *Journal of Physics D: Applied Physics*, 42(19):194013, 2009.
- [70] A. Gibson, M. Foucher, D. Marinov, P. Chabert, T. Gans, M. Kushner, and J.-P. Booth. The role of thermal energy accommodation and atomic recombination probabilities in low pressure oxygen plasmas. *Plasma Physics and Controlled Fusion*, 59(2), 2017. 2017, IOP Publishing Ltd.
- [71] S.-H. Song, Y. Yang, P. Chabert, and M. J. Kushner. Electron energy distributions in a magnetized inductively coupled plasma. *Physics of Plasmas*, 21(9):093512, 2014.
- [72] P. L. G. Ventzek, R. J. Hoekstra, and M. J. Kushner. Two dimensional modeling of high plasma density inductively coupled sources for materials processing. *Journal of Vacuum Science & Technology B: Microelectronics and Nanometer Structures Processing, Measurement, and Phenomena*, 12(1):461, 1994.
- [73] P. L. G. Ventzek, T. J. Sommerer, R. J. Hoekstra, and M. J. Kushner. Two dimensional hybrid model of inductively coupled plasma sources for etching. *Applied Physics Letters*, 63(5):605, 1993.
- [74] D. L. Scharfetter and H. K. Gummel. Large-signal analysis of a silicon read diode oscillator. *IEEE Transactions on Electron Devices*, 16(1):64, 1969.
- [75] V. A. Godyak and R. B. Piejak. Abnormally low electron energy and heating-mode transition in a low-pressure argon rf discharge at 13.56 mhz. *Phys. Rev. Lett.*, 65:996, 1990.
- [76] S.-H. Song and M. J. Kushner. Control of electron energy distributions and plasma characteristics of dual frequency, pulsed capacitively coupled plasmas sustained in Ar and Ar/CF₄/O₂. *Plasma Sources Science and Technology*, 21(5):055028, 2012.
- [77] S. Rauf and M. Kushner. Argon metastable densities in radio frequency Ar, Ar/O₂ and Ar/CF₄ electrical discharges. *Journal of Applied Physics*, 82(6):2805, 1997.
- [78] K. Tachibana. Excitation of the $1s_5, 1s_4, 1s_3$, and $1s_2$ levels of argon by low-energy electrons. *Phys. Rev. A*, 34:1007, 1986.
- [79] D. Rapp and P. Englander-Golden. Total cross sections for ionization and attachment in gases by electron impact. i. positive ionization. *The Journal of Chemical Physics*, 43(5):1464, 1965.
- [80] R. H. McFarland and J. D. Kinney. Absolute cross sections of lithium and other alkali metal atoms for ionization by electrons. *Phys. Rev.*, 137:A1058, 1965.
- [81] P. K. Lechner and R. J. Ericson. Time dependence of the vacuum-ultraviolet emissions in krypton excited by 250-keV electrons. *Phys. Rev. A*, 9:251, 1974.

- [82] L. G. Piper, J. E. Velazco, and D. W. Setser. Quenching cross sections for electronic energy transfer reactions between metastable argon atoms and noble gases and small molecules. *The Journal of Chemical Physics*, 59(6):3323, 1973.
- [83] D. L. King, L. G. Piper, and D. W. Setser. Electronic energy transfer from metastable argon $4(s^3P_{2,0})$ to xenon, oxygen and chlorine atoms. *J. Chem. Soc., Faraday Trans. 2*, 73:177, 1977.
- [84] D. C. Parent, R. Derai, G. Mauclaire, M. Heninger, R. Marx, M. E. Rincon, A. O'Keefe, and M. T. Bowers. Comparison of energy partitioning in Ar^+ and N_2^+ charge-transfer reactions. *Chemical Physics Letters*, 117(2):127, 1985.
- [85] P. Gaucherel and B. Rowe. Measurement of rates of charge exchange and dissociative recombination reactions in Ar-N₂, Ar-H₂ and Ar-O₂ mixtures. *International Journal of Mass Spectrometry and Ion Physics*, 25(2):211, 1977.
- [86] S. A. Lawton and A. V. Phelps. Excitation of the $b^1\sigma_g^-$ state of o₂ by low energy electrons. *The Journal of Chemical Physics*, 69(3):1055, 1978.
- [87] M. Tashiro, K. Morokuma, and J. Tennyson. R-matrix calculation of electron collisions with electronically excited o₂ molecules. *Phys. Rev. A*, 73:052707, 2006.
- [88] Y. Itikawa and A. Ichimura. Cross sections for collisions of electrons and photons with atomic oxygen. *Journal of Physical and Chemical Reference Data*, 19(3):637, 1990.
- [89] R. I. Hall and S. Trajmar. Scattering of 4.5 ev electrons by ground (x^3/σ_g^-) state and metastable ($a^1\delta g$) oxygen molecules. *Journal of Physics B: Atomic and Molecular Physics*, 8(12):L293, 1975.
- [90] P. D. Burrow. Dissociative attachment from the O₂($a^1\delta g$) state. *The Journal of Chemical Physics*, 59(9):4922, 1973.
- [91] H. Deutsch, P. Scheier, K. Becker, and T. Märk. Calculated cross-sections for the electron-impact detachment from negative ions using the deutsch- märk (dm) formalism. *Chemical Physics Letters*, 382(1):26, 2003.
- [92] A. Florescu-Mitchell and J. Mitchell. Dissociative recombination. *Physics Reports*, 430(5):277, 2006.
- [93] R. Peverall, et al. Dissociative recombination and excitation of o₂⁺: Cross sections, product yields and implications for studies of ionospheric airglows. *The Journal of Chemical Physics*, 114(15):6679, 2001.
- [94] J. T. Gudmundsson. A critical review of the reaction set for a low pressure oxygen processing discharge. *Technical report*, 2004.
- [95] S. G. Ard, J. J. Melko, B. Jiang, Y. Li, N. S. Shuman, H. Guo, and A. A. Viggiano. Temperature dependences for the reactions of o₂⁻ and o⁻ with n and o atoms in a selected-ion flow tube instrument. *The Journal of Chemical Physics*, 139(14):144302, 2013.

- [96] A. Midey, I. Dotan, S. Lee, W. T. Rawlins, M. A. Johnson, and A. A. Viggiano. Kinetics for the reactions of O^- and O_2^- with O_2 ($a^1\Delta_g$) measured in a selected ion flow tube at 300 k. *The Journal of Physical Chemistry A*, 111(24):5218, 2007. PMID: 17523608.
- [97] N. L. Aleksandrov. *Soviet physics Technical physics*, 23:806, 1978.
- [98] M. Ziólkowski, G. C. Schatz, A. A. Viggiano, A. Midey, and I. Dotan. O_2 ($X^3\Sigma_g^-$) and O_2 ($a^1\Delta_g$) charge exchange with simple ions. *The Journal of Chemical Physics*, 140(21):214307, 2014.
- [99] I. Dotan. Rate constants and branching ratios for the reactions of $^{18}O^+$ and ^{18}O $^{18}O^+$ ions with ^{16}O ^{16}O measured at relative kinetic energies 0.04-2 eV. *Chemical Physics Letters*, 75(3):509, 1980.
- [100] V. Abreu, J. Yee, S. Solomon, and A. Dalgarno. The quenching rate of $O(^1D)$ by $O(^3P)$. *Planetary and Space Science*, 34(11):1143, 1986.
- [101] R. Atkinson, D. L. Baulch, R. A. Cox, J. N. Crowley, R. F. Hampson, R. G. Hynes, M. E. Jenkin, M. J. Rossi, and J. Troe. Evaluated kinetic and photochemical data for atmospheric chemistry: Volume i - gas phase reactions of O_x , HO_x , NO_x and SO_x species. *Atmospheric Chemistry and Physics*, 4(6):1461, 2004.
- [102] G. E. Streit, C. J. Howard, A. L. Schmeltekopf, J. A. Davidson, and H. I. Schiff. Temperature dependence of $O(^1D)$ rate constants for reactions with O_2 , N_2 , CO_2 , O_3 , and H_2O . *The Journal of Chemical Physics*, 65(11):4761, 1976.
- [103] L. C. Lee and T. G. Slanger. Observations on $O(^1D \rightarrow ^3P)$ and $O_2(b^1\Sigma_g^+ \rightarrow X^3\Sigma_g^-)$ following O_2 photodissociation. *The Journal of Chemical Physics*, 69(9):4053, 1978.
- [104] I. Clark and R. Wayne. The reaction of $O_2(^1\Delta_g)$ with atomic nitrogen and with atomic oxygen. *Chemical Physics Letters*, 3(6):405, 1969.
- [105] J. B. Burkholder, S. P. Sander, J. P. D. Abbatt, J. R. Barker, R. E. Huie, C. E. Kolb, M. J. Kurylo, V. L. Orkin, D. M. Wilmouth, and P. H. Wine. Chemical kinetics and photochemical data for use in atmospheric studies. *Evaluation Number 18, JPL Publication 15-10*, 2015.
- [106] R. F. H. III, C. E. Gardner, T. M. E. Sayed, G. I. Segal, and J. V. V. Kasper. Temperature dependence of $O_2(^1\Delta) + O_2(^1\Delta)$ and $I(^2P_{1/2}) + O_2(^1\Delta)$ energy pooling. *The Journal of Chemical Physics*, 74(10):5618, 1981.
- [107] T. Laffleur. Tailored-waveform excitation of capacitively coupled plasmas and the electrical asymmetry effect. *Plasma Sources Science and Technology*, 25(1):013001, 2016.
- [108] E. Schüngel, I. Korolov, B. Bruneau, A. Derzsi, E. Johnson, D. O'Connell, T. Gans, J.-P. Booth, Z. Donkó, and J. Schulze. Tailored voltage waveform capacitively coupled plasmas in electronegative gases: frequency dependence of asymmetry effects. *Journal of Physics D: Applied Physics*, 49(26):265203, 2016.
- [109] P. Diomede, B. Bruneau, S. Longo, E. Johnson, and J.-P. Booth. Capacitively coupled hydrogen plasmas sustained by tailored voltage waveforms: vibrational kinetics and negative ions control. *Plasma Sources Science and Technology*, 26(7):075007, 2017.

- [110] A. Derzsi, B. Bruneau, A. R. Gibson, E. Johnson, D. O'Connell, T. Gans, J.-P. Booth, and Z. Donkó. Power coupling mode transitions induced by tailored voltage waveforms in capacitive oxygen discharges. *Plasma Sources Science and Technology*, 26(3):034002, 2017.
- [111] B. Bruneau, T. Gans, D. O'Connell, A. Greb, E. V. Johnson, and J.-P. Booth. Strong ionization asymmetry in a geometrically symmetric radio frequency capacitively coupled plasma induced by sawtooth voltage waveforms. *Phys. Rev. Lett.*, 114:125002, 2015.
- [112] B. Bruneau, T. Novikova, T. Laffleur, J. P. Booth, and E. V. Johnson. Ion flux asymmetry in radiofrequency capacitively-coupled plasmas excited by sawtooth-like waveforms. *Plasma Sources Science and Technology*, 23(6):065010, 2014.
- [113] T. Takagi. Ion surface interactions during thin film deposition. *Journal of Vacuum Science & Technology A*, 2(2):382, 1984.
- [114] H. B. Profijt, S. E. Potts, M. C. M. van de Sanden, and W. M. M. Kessels. Plasma-assisted atomic layer deposition: Basics, opportunities, and challenges. *Journal of Vacuum Science & Technology A*, 29(5):050801, 2011.
- [115] H. B. Profijt, P. Kudlacek, M. C. M. van de Sanden, and W. M. M. Kessels. Ion and photon surface interaction during remote plasma etch of metal oxides. *Journal of The Electrochemical Society*, 158(4):G88, 2011.
- [116] T. Faraz, K. Arts, S. Karwal, H. C. M. Knoops, and W. M. M. Kessels. Energetic ions during plasma-enhanced atomic layer deposition and their role in tailoring material properties. *Plasma Sources Science and Technology*, 28(2):024002, 2019.
- [117] B. Bruneau. *Control of radio frequency capacitively coupled plasma asymmetries using Tailored Voltage Waveforms*. Theses, Ecole Polytechnique, 2015.
- [118] Y. Wang and J. K. Olthoff. Ion energy distributions in inductively coupled radio-frequency discharges in argon, nitrogen, oxygen, chlorine, and their mixtures. *Journal of Applied Physics*, 85:6358, 1999.
- [119] J. T. Gudmundsson. The ion energy distribution in a planar inductive oxygen discharge. *Journal of Physics D: Applied Physics*, 32(7):798, 1999.
- [120] H. Seo, S. B. Kim, J. Song, Y. Kim, H. Soh, Y. C. Kim, and H. Jeon. Low temperature remote plasma cleaning of the fluorocarbon and polymerized residues formed during contact hole dry etching. *Journal of Vacuum Science & Technology B: Microelectronics and Nanometer Structures Processing, Measurement, and Phenomena*, 20(4):1548, 2002.
- [121] C.-Y. Sin, B.-H. Chen, W. L. Loh, J. Yu, P. Yelehanka, A. See, and L. Chan. Resist trimming in high-density cf₄/o₂ plasmas for sub-0.1 μm device fabrication. *Journal of Vacuum Science & Technology B: Microelectronics and Nanometer Structures Processing, Measurement, and Phenomena*, 20(5):1974, 2002.
- [122] S. Rauf. Model for photoresist trim etch in inductively coupled cf₄/o₂ plasma. *Journal of Vacuum Science & Technology B: Microelectronics and Nanometer Structures Processing, Measurement, and Phenomena*, 22(1):202, 2004.

- [123] F. Greer, L. Van, D. Fraser, J. W. Coburn, and D. B. Graves. Argon and oxygen ion chemistry effects in photoresist etching. *Journal of Vacuum Science & Technology B: Microelectronics and Nanometer Structures Processing, Measurement, and Phenomena*, 20(5):1901, 2002.
- [124] A. Sankaran and M. J. Kushner. Integrated feature scale modeling of plasma processing of porous and solid sio. ii. residual fluorocarbon polymer stripping and barrier layer deposition. *Journal of Vacuum Science & Technology A Vacuum Surfaces and Films*, 22, 2004.
- [125] O. Joubert, J. Pelletier, and Y. Arnal. The etching of polymers in oxygen based plasmas: A parametric study. *Journal of Applied Physics*, 65(12):5096, 1989.
- [126] D. L. Flamm and V. M. Donnelly. The design of plasma etchants. *Plasma Chemistry and Plasma Processing*, 1(4):317, 1981.
- [127] Q. Zeng, H. Jin, S. Meng, W. Liang, and H. Shu. Spatially resolved ground state atomic oxygen density during the mode transition of inductively coupled oxygen plasmas. *Vacuum*, 164:98, 2019.
- [128] S. Tinck and A. Bogaerts. Computer simulations of an oxygen inductively coupled plasma used for plasma-assisted atomic layer deposition. *Plasma Sources Science and Technology*, 20(1):015008, 2011.
- [129] P. J. Bruggeman, N. Sadeghi, D. C. Schram, and V. Linss. Gas temperature determination from rotational lines in non-equilibrium plasmas: a review. *Plasma Sources Science and Technology*, 23(2):023001, 2014.
- [130] P. C. Cosby. Electron impact dissociation of oxygen. *The Journal of Chemical Physics*, 98(12):9560, 1993.
- [131] J. T. Gudmundsson and M. A. Lieberman. Model and measurements for a planar inductive oxygen discharge. *Plasma Sources Science and Technology*, 7(1):1, 1998.
- [132] N. C. M. Fuller, M. V. Malyshev, V. M. Donnelly, and I. P. Herman. Characterization of transformer coupled oxygen plasmas by trace rare gases-optical emission spectroscopy and langmuir probe analysis. *Plasma Sources Science and Technology*, 9(2):116, 2000.
- [133] J. Guha, R. Khare, L. Stafford, V. M. Donnelly, S. Sirard, and E. A. Hudson. Effect of cu contamination on recombination of o atoms on a plasma-oxidized silicon surface. *Journal of Applied Physics*, 105(11):113309, 2009.
- [134] J. P. Booth and N. Sadeghi. Oxygen and fluorine atom kinetics in electron cyclotron resonance plasmas by time resolved actinometry. *Journal of Applied Physics*, 70(2):611, 1991.
- [135] P. J. Chantry. A simple formula for diffusion calculations involving wall reflection and low density. *Journal of Applied Physics*, 62(4):1141, 1987.
- [136] S. Chapman and T. G. Cowling. *The Mathematical Theory of Non-uniform Gases*. Cambridge University Press, 3rd edition, 1970.

- [137] M. Z. ul Islam, K. Niemi, T. Gans, and D. O'Connell. Energetic electron avalanches and mode transitions in planar inductively coupled radio-frequency driven plasmas operated in oxygen. *Applied Physics Letters*, 99(4):041501, 2011.
- [138] R. Zaplotnik, A. Vesel, and M. Mozetic. Transition from e to h mode in inductively coupled oxygen plasma Hysteresis and the behaviour of oxygen atom density. *EPL (Europhysics Letters)*, 95(5):55001, 2011.
- [139] H.-C. Lee and C.-W. Chung. Control of electron energy distribution by adding a pulse inductive field in capacitive discharge. *Plasma Sources Science and Technology*, 23(6):062002, 2014.
- [140] G. Dilecce, M. Vigliotti, and S. D. Benedictis. A talif calibration method for quantitative oxygen atom density measurement in plasma jets. *Journal of Physics D: Applied Physics*, 33(6):53, 2000.
- [141] U. Czarnetzki, D. Luggenhölscher, and H. F. Döbele. Space and time resolved electric field measurements in helium and hydrogen RF-discharges. *Plasma Sources Science and Technology*, 8(2):230, 1999.
- [142] S. Kechkar, P. Swift, S. Kelly, S. Kumar, S. Daniels, and M. Turner. Investigation of the electron kinetics in O₂ capacitively coupled plasma with the use of a langmuir probe. *Plasma Sources Science and Technology*, 26(6):065009, 2017.
- [143] K. Stapelmann, M. Fiebrandt, T. Styrnoll, S. Baldus, N. Bibinov, and P. Awakowicz. Implications of electron heating and non-uniformities in a vhf-ccp for sterilization of medical instruments. *Plasma Sources Science and Technology*, 24(3):034014, 2015.
- [144] J. T. Gudmundsson and B. Ventéjou. The pressure dependence of the discharge properties in a capacitively coupled oxygen discharge. *Journal of Applied Physics*, 118(15):153302, 2015.
- [145] M.-H. Lee, H.-C. Lee, and C.-W. Chung. Comparison of pressure dependence of electron energy distributions in oxygen capacitively and inductively coupled plasmas. *Phys. Rev. E*, 81:046402, 2010.
- [146] J. D. Bernstein, S. Qin, C. Chan, and Tsu-Jae King. High dose-rate hydrogen passivation of polycrystalline silicon cmos tfts by plasma ion implantation. *IEEE Transactions on Electron Devices*, 43(11):1876, 1996.
- [147] G. Liu and S. J. Fonash. Polycrystalline silicon thin film transistors on corning 7059 glass substrates using short time, low temperature processing. *Applied Physics Letters*, 62(20):2554, 1993.
- [148] F. Wu, G. Levitin, and D. W. Hess. Low-temperature etching of cu by hydrogen-based plasmas. *ACS Applied Materials & Interfaces*, 2(8):2175, 2010.
- [149] B. N. Ganguly and P. Bletzinger. Effect of plasma?surface interactions on the radial variation of h atom density in a hydrogen radio frequency discharge. *Journal of Applied Physics*, 76(3):1476, 1994.
- [150] H. M and H. M. *Carbon Nanowalls: Synthesis and Emerging Applications*. New York: Springer, 2010.

- [151] I. Vlassiouk, M. Regmi, P. Fulvio, S. Dai, P. Datskos, G. Eres, and S. Smirnov. Role of hydrogen in chemical vapor deposition growth of large single-crystal graphene. *ACS Nano*, 5(7):6069, 2011. PMID: 21707037.
- [152] M. Hori, H. Kondo, and M. Hiramatsu. Radical-controlled plasma processing for nanofabrication. *Journal of Physics D: Applied Physics*, 44(17):174027, 2011.
- [153] G. Cunge, B. Pelissier, O. Joubert, R. Ramos, and C. Maurice. New chamber walls conditioning and cleaning strategies to improve the stability of plasma processes. *Plasma Sources Science and Technology*, 14(3):599, 2005.
- [154] O. Joubert, G. Cunge, B. Pelissier, L. Vallier, M. Kogelschatz, and E. Pargon. Monitoring chamber walls coating deposited during plasma processes: Application to silicon gate etch processes. *Journal of Vacuum Science & Technology A: Vacuum, Surfaces, and Films*, 22(3):553, 2004.